Auguste Renoir, *Landscape between Storm*, 1874

PSA or TSA for Drying Green Hydrogen

by

Kausthubh Khodke

To obtain the degree of Master of Science
at Delft University of Technology
to be defended publicly on Wednesday September 30th, 2026 at 10:00 AM

Student number: 5842379
Thesis committee: Dr. ir. Mahinder Ramdin, TU Delft, supervisor
Dr. Huseyin Bural Eral, TU Delft

TU Delft

Abstract

Green hydrogen produced by alkaline water electrolysis may contain residual water vapour and other impurities that must be removed before use in fuel-cell applications. This study investigated adsorption-based hydrogen drying using Pressure Swing Adsorption (PSA) and Temperature Swing Adsorption (TSA), with particular attention to process modelling in Aspen Adsorption.

Zeolite 4A was selected because of its strong affinity for water at low partial pressures. Water adsorption equilibrium was represented using a Dual-Site Langmuir 2 model, while mass transfer was described using the Linear Driving Force model. A non-isothermal packed-bed model was developed for a hydrogen feed containing $872\ \mathrm{ppmv}$ water at $25\ \mathrm{bar}$, $298.15\ \mathrm{K}$, and a flow rate of $0.0223\ \mathrm{kmol\,s^{-1}}$.

Several PSA configurations were tested, including conventional pressure regeneration, vacuum regeneration, and temperature-assisted vacuum regeneration. Conventional regeneration at $1\ \mathrm{bar}$ produced only limited reduction in solid water loading, while deep-vacuum simulations showed numerical convergence problems during multi-cycle operation. Therefore, the detailed cyclic and economic assessment was continued using TSA.

For the TSA process, the simulated breakthrough time was approximately $19\,250\ \mathrm{s}$, and an adsorption time of $14\,000\ \mathrm{s}$ was selected to provide a safety margin before water breakthrough. Regeneration with heated dry hydrogen up to $175\,^{\circ}\mathrm{C}$ reduced the water loading from approximately 0.0138 to $0.0018\ \mathrm{kmol\,kg^{-1}}$. The process reached cyclic steady state after 23 cycles and maintained the outlet water concentration below the selected limit of $5\ \mathrm{ppmv}$. The calculated hydrogen recovery was 94.32%.

A staggered three-bed arrangement was proposed for continuous operation, giving an estimated net hydrogen-production rate of $151.3\ \mathrm{kg\,h^{-1}}$. The screening-level OpenPyTEA analysis resulted in a fixed capital investment of approximately $5.303\ \mathrm{million\ EUR}$ and a total annual operating expenditure of approximately $0.656\ \mathrm{million\ EUR\,year^{-1}}$. The deterministic levelized cost of hydrogen drying was $1.179\ \mathrm{EUR\,kg_{H_2}^{-1}}$. A combined techno-economic Monte Carlo analysis gave a mean levelized cost of $1.232\ \mathrm{EUR\,kg_{H_2}^{-1}}$, with a central 95% uncertainty interval of 0.852 to $1.723\ \mathrm{EUR\,kg_{H_2}^{-1}}$.

The results demonstrate the technical potential of Zeolite 4A TSA for deep hydrogen drying. However, experimental validation is required, particularly for adsorption kinetics, heat transfer parameters, and the low temperatures predicted during blowdown.

Acknowledgement

I would like to express my sincere gratitude to my supervisor, Prof. Mahinder Ramdin, for his continuous support, guidance and constructive feedback throughout this thesis project. His supervision helped me approach complex problems step by step, understand the underlying principles and make steady progress. I am especially grateful for the way he encouraged me to think critically, ask the right questions and understand the reasoning behind each decision.

I would also like to thank my academic counsellor, Evert Vixseboxse, for his support during a difficult period. His guidance helped me cope with the challenges I faced and find a way forward during my time at TU Delft. I deeply appreciate his patience, understanding and encouragement.

I am also grateful to Prof. Tony Kiss for his valuable guidance, technical insights and constructive suggestions during this project.

Furthermore, I would like to thank all instructors and staff members of the Energy, Flow and Process Technology section at Delft University of Technology for providing the necessary resources and for creating a supportive and stimulating academic environment.

The use of generative AI language models for clarification of technical concepts, language improvement is also acknowledged.

Finally, I would like to thank my family and friends for their constant support, patience and encouragement. Their presence made this phase of my life more manageable, and completing this thesis would have been much more difficult without them.

Contents

List of Figures

List of Tables

1

Green Hydrogen and Purity

Found in abundance in nature, hydrogen has long been identified as a potential energy carrier for transitioning away from fossil fuels. Green hydrogen is produced through the electrolysis of water using renewable electricity sources such as solar or wind. Unlike grey hydrogen which is produced from fossil fuels or blue hydrogen which employs carbon capture and storage (CCS), green hydrogen produced via electrolysis using renewable energy sources such as solar and wind power is inherently carbon free and is considered an environmentally sustainable energy carrier. It plays a pivotal role in decarbonizing hard to electrify sectors like heavy industry, aviation, and long-haul transport. Additionally, it enhances energy security and supports international climate goals such as net zero emissions [1].

Hydrogen Production Technologies: Steam Methane Reforming (SMR) is the most common method for hydrogen production but emits significant amounts of carbon dioxide. It involves reacting methane with steam over a catalyst to produce H_2 and CO_2. Electrolysis on the other hand, is a cleaner alternative with no carbondioxide contaminants.

- Alkaline Water Electrolysis (AWE) uses a liquid alkaline electrolyte, KOH or NaOH. It is cost-effective, and scalable.
- Proton Exchange Membrane (PEM) Electrolysis uses a solid polymer electrolyte and offers high efficiency and fast dynamic response but is costlier due to the use of precious metal catalysts, making it more suitable for small-scale operations
- Solid Oxide Electrolysis (SOEC) is a high-temperature electrolysis technology with typical operating temperatures ranging from 700°C to 1000°C. It offers high electrical efficiency; however, the high operating temperatures require complex thermal management and may lead to material degradation.

Hydrogen is primarily used in oil refining and ammonia synthesis, with global production around 70 million metric tons annually. With fuel cell vehicle deployment projected to reach 2.5 million by 2030 [1], demand for green hydrogen is increasing. Electrolytic hydrogen may contain contaminants such as carbon monoxide, which is harmful to fuel cells and expensive to remove [2, 3]. ISO 14687:2019 outlines stringent purity requirements for hydrogen, specifying allowable levels for 13 gaseous contaminants, of which only nitrogen, oxygen, and water are commonly found in electrolytic hydrogen [4, 5].

The table 1.1 shows the origin of these three contaminant gases along with their ISO standards.

Nitrogen: Often introduced during purging or maintenance. High concentrations can cause fuel cell power loss. Generally, no post treatment is needed as initial venting of the system removes nitrogen. For a continuous process nitrogen is mainly found dissolved in the feed water for electrolysers. To avoid this contamination a pre treatment involving degassing of the feed water can be done [1].

Oxygen: Oxygen contamination is mostly due to production at anode as gas and tends to mix with produced hydrogen gas at cathode because of direct diffusion through separator/membrane commanly refered to as gas cross over. Oxygen contamination can be hazardous and can be explosive with

Table 1.1: Origin of most probable hydrogen contaminants in alkaline electrolysis [1]

Contaminants	ISO 14687:2019 threshold	Typical content without treatment	Origin	Removal Technique
Nitrogen	300 ppm	<100ppm after initial purge	Purge and inertization	Venting of initial production
Oxygen	5 ppm	2000-6000 ppm	Feed-in water gas solubility	Catalytic recombination
Water	5 ppm	>2000 ppm, saturated at ambient temperature	Cross over process	Gas cooling, PSA or TSA systems

explosive limit as low as 4%. Oxygen is typically removed using a catalytic recombination after which oxygen is converted to water vapour which is safer and easier to remove after further processing [1].

Water: Water may remain in vapor phase under certain pressure temperature combinations, but if the gas is cooled below its dew point, condensation or freezing can occur. Therefore, drying systems must avoid conditions that lead to ice formation, which can block flow paths or damage components. Water vapour may even carry traces of dissolved potassium or sodium ions, which may corrode components but can be removed via scrubber [1].

The process of drying hydrogen by removing the above-mentioned impurities is a key area of focus of this study. Several technologies, such as membrane separation, glycol absorption, and cryogenic drying, can be used for hydrogen drying [6]. However, adsorption based technologies remain among the most widely applied methods for achieving very low moisture contents required for high purity hydrogen applications. Specifically, this study focuses on two important technologies that have been developed over the years and have demonstrated very good performance, Pressure Swing Adsorption (PSA) and Temperature Swing Adsorption (TSA). These technologies use an adsorbent material to selectively capture impurities, water vapour in this case, resulting in purified hydrogen for use in fuel cells.

Even though extensive literature exists on PSA and TSA systems, most published studies investigate these technologies independently rather than providing a direct comparison under similar operating conditions [7, 8]. A large portion of the available research focuses primarily on laboratory scale experiments, while limited work has been conducted on detailed process modeling and the related modeling challenges for industrial hydrogen drying systems. Limited literature on H_2 –H_2O vapour liquid equilibrium (VLE), water adsorption behaviour on adsorbents, and Aspen Adsorption modeling for hydrogen drying further complicates the development of reliable simulation models. Several studies reporting experimental adsorption data do not clearly describe how these data are translated into adsorption isotherm models and simulation parameters for process modelling software. Therefore, this study aims to investigate the drying of hydrogen using PSA and TSA technologies through Aspen Adsorption simulations. Water adsorption data for selected adsorbents will be used to fit appropriate adsorption isotherms and obtain the required isotherm parameters for simulation. In addition, H_2 –H_2 O VLE/dew point relationships will be used to determine the feed moisture composition of the binary H_2 –H_2 O mixture. The performance of PSA and TSA systems will be evaluated in terms of water removal efficiency, hydrogen purity, hydrogen recovery and operational considerations.

1.1. Research Objective

The main objective of this thesis is to investigate adsorption based drying of hydrogen produced by alkaline water electrolysis, with emphasis on the regeneration of the adsorbent using pressure swing and temperature swing strategies. Dynamic simulations in Aspen Adsorption are used to evaluate the adsorption and regeneration behaviour of the system and to develop a cyclic drying process capable of reducing the water content of hydrogen to the required ISO 14687:2019 specification.

1.1.1. Research Questions

The main research question addressed in this thesis is:

> *How can adsorption based pressure and temperature swing regeneration be applied to the deep drying of hydrogen produced by alkaline water electrolysis?*

To address this main question, the following sub research questions are considered:

1. **Adsorbent and equilibrium behaviour:**

   Which adsorbent is most suitable for deep water removal from hydrogen and how can its adsorption equilibrium be represented for dynamic process simulation?

2. **Regeneration strategy:**

   To what extent can pressure reduction and temperature increase regenerate the selected adsorbent after hydrogen drying?

3. **Cyclic TSA performance:**

   Can a temperature swing adsorption cycle be developed that achieves sufficient adsorbent regeneration and maintains the required hydrogen product quality over repeated cycles?

4. **Process-level feasibility:**

   What are the hydrogen recovery, productivity, energy requirements, equipment requirements, and preliminary economic implications of the developed TSA process when extended to continuous operation?

1.1.2. Scope of the Study

This study focuses specifically on the removal of residual water from hydrogen produced by alkaline water electrolysis. It is assumed that upstream treatment has already removed electrolyte droplets, residual oxygen, and bulk liquid water. The feed to the adsorption system is therefore represented as a binary $\mathrm{H_2}$–$\mathrm{H_2O}$ mixture.

Adsorbent selection is based on literature data, after which Zeolite 4A is investigated in detail. The adsorption equilibrium of water on Zeolite 4A is represented using a Dual-Site Langmuir2 model, while dynamic adsorption and regeneration are simulated in Aspen Adsorption.

Both pressure-driven and temperature-driven regeneration strategies are investigated. Pressure swing regeneration is evaluated to determine the extent of desorption achievable through depressurisation and deep vacuum. Because stable multi-cycle PSA/VPSA operation could not be obtained under the investigated conditions, detailed cyclic steady-state analysis, continuous process configuration, equipment sizing, and techno-economic assessment are performed for the developed TSA process.

The techno-economic analysis is intended as a preliminary, screening level assessment rather than a detailed plant design or investment estimate. Its purpose is to identify the principal equipment, energy requirements, and cost contributions associated with the proposed TSA hydrogen-drying system.

1.2. Progression of the Study

The study was conducted in a series of stages. First, potential adsorbents for hydrogen drying were evaluated based on literature data, with particular attention to water adsorption at low partial pressures. Zeolite 4A was subsequently selected for detailed investigation.

Experimental water adsorption data for Zeolite 4A at different temperatures were then fitted using a temperature-dependent adsorption isotherm model. The resulting equilibrium model, together with the selected mass-transfer, momentum, and energy-balance formulations, was implemented in Aspen Adsorption to construct a dynamic packed bed model.

The adsorption behaviour of the bed was first investigated through breakthrough simulations. Regeneration was subsequently studied using pressure reduction, including deep vacuum conditions, to assess the feasibility of PSA/VPSA operation. Although deeper vacuum improved desorption, numerical instability prevented the development of a stable full cyclic PSA process under the investigated conditions.

The study therefore proceeded with the development of a temperature swing adsorption cycle. The effects of heating, purge flow, cooling, and repressurisation were investigated, after which repeated cycles were simulated to evaluate the approach towards cyclic steady state. The resulting TSA process was assessed in terms of breakthrough behaviour, regeneration, product water concentration, hydrogen recovery, and adsorbent productivity.

Finally, the single bed cycle was extended conceptually to a three bed configuration for continuous hydrogen production. The principal process equipment was sized and the associated energy requirements were estimated. These results were then used to perform a preliminary techno-economic assessment of the proposed TSA hydrogen drying process.

2

Adsorption

According to the *Compendium of Chemical Terminology*, adsorption is defined as an increase in the concentration of a substance at the interface between a condensed phase and a fluid phase due to the action of surface forces [9]. Adsorption is widely applied in gas purification and separation processes because of its operational simplicity and the possibility of regenerating and reusing the adsorbent [10].

In the present study, adsorption is considered for the selective removal of water vapour from hydrogen. Water acts as the adsorbate, while the porous solid material acts as the adsorbent. The suitability of an adsorbent for hydrogen drying depends not only on its total water adsorption capacity, but also on its affinity for water at the low partial pressures relevant to deep drying, its adsorption and desorption kinetics, and its ability to be regenerated over repeated cycles. The following sections therefore discuss water adsorption equilibrium, adsorption-based regeneration techniques, adsorbent materials and their water sorption behaviour, and the principal criteria governing adsorbent selection for hydrogen drying.

2.1. Water Adsorption Isotherm

To evaluate the amount of adsorbate that can be captured by an adsorbent, it is essential to understand adsorption equilibrium. An adsorption isotherm describes this equilibrium at constant temperature and relates the equilibrium adsorbed amount to the concentration or partial pressure of the adsorbate in the fluid phase. The equilibrium behaviour is influenced by several parameters, including the nature of the adsorbent and adsorbate, temperature, ionic strength, and solution chemistry [11]. Adsorption isotherms can be established experimentally or using appropriate simulation and modelling approaches, provided sufficient time is allowed for the system to reach equilibrium. Such models are widely applied in separation processes, including carbon dioxide capture and chemical purification [12, 13]. Numerous mathematical isotherm models have been developed to describe adsorption equilibrium for different adsorbate–adsorbent systems.

For water adsorption, the isotherm provides considerably more information than simply indicating whether an adsorbent is hydrophilic or hydrophobic. The shape and position of the isotherm influence the equilibrium adsorption capacity, working capacity, regeneration requirements, and suitable operating conditions of adsorption-based drying systems. For hydrogen drying applications, water is present at very low partial pressures. Therefore, adsorption behaviour in the low pressure region is particularly important.

Adsorbents exhibiting Type I behaviour, such as many zeolitic materials, show substantial water uptake even at low relative pressures. This makes them attractive for deep drying applications in which very low residual moisture concentrations are required. In contrast, materials exhibiting Type III or Type V behaviour generally adsorb relatively little water at very low partial pressures and may therefore be less suitable for ultra dry hydrogen production.

The location of the transition or inflection region of the adsorption isotherm also has direct implications for adsorbent selection. An inflection occurring at a low relative pressure indicates a comparatively

strong affinity between water molecules and the adsorbent surface. Strong adsorption is favourable during the drying step because it enables water to be removed even when its gas phase concentration is very low. However, strong adsorbate–adsorbent interactions can also make regeneration more difficult and may increase the energy required for desorption, particularly in Temperature Swing Adsorption (TSA) processes.

Adsorbent selection therefore involves a trade off between achieving sufficiently strong water adsorption during the drying step and maintaining adequate regenerability during cyclic operation. For this reason, adsorption isotherms are important not only for material characterisation, but also as fundamental inputs for the modelling and design of PSA and TSA systems.

Water is a polar molecule and has a strong ability to form hydrogen bonds. Consequently, its interaction with an adsorbent surface depends on several material properties, including hydrophilicity, structural and chemical stability, pore size and geometry, surface chemistry, and adsorption thermodynamics. Depending on these characteristics, different types of water adsorption isotherms can be observed.

IUPAC classifies water adsorption isotherms into seven characteristic types that can be used to interpret the hydrophilic or hydrophobic behaviour of porous materials [14]. Type I isotherms show substantial water uptake at very low pressures and are associated with strongly hydrophilic adsorbents. Type II and Type IV isotherms exhibit lower initial slopes and therefore weaker water affinity in the low pressure region compared with Type I behaviour. Type III isotherms exhibit low water uptake at low relative pressure, indicating comparatively weak adsorbate surface interactions and hydrophobic behaviour. Type V isotherms also show limited uptake at low pressure but exhibit an S-shaped adsorption profile. Type VI isotherms are characterised by stepwise adsorption behaviour and may occur when several sequential adsorption interactions take place. Type VII behaviour is approximately linear and is associated with strongly hydrophobic adsorbents [15]. Overall, the different isotherm shapes provide an indication of the relative hydrophilicity or hydrophobicity of an adsorbent. This behaviour can also be related to the position of the isotherm inflection point. The inflection point is defined as the position at which approximately half of the maximum adsorption capacity is reached [16]. An inflection point occurring at lower relative pressure generally indicates stronger water affinity.

For hydrogen drying, the low-pressure region of the water adsorption isotherm is therefore of particular importance. The adsorbent must maintain sufficient affinity for water as the gas-phase water concentration approaches the required product specification. At the same time, excessively strong adsorption can increase the severity of the conditions required for regeneration. The water adsorption isotherm consequently provides an important basis for both adsorbent selection and the subsequent evaluation of pressure and temperature driven regeneration strategies.

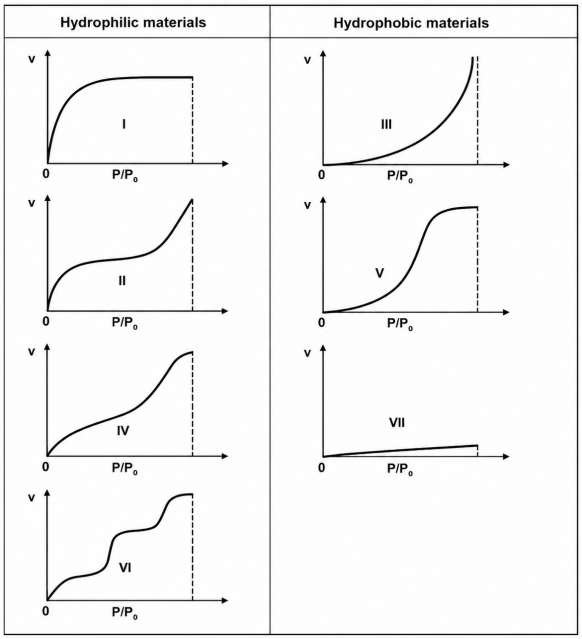

Figure 2.1: IUPAC classification of adsorption isotherms for hydrophilic and hydrophobic materials (adapted from [17]).

2.2. Adsorption Techniques

Several adsorption based process configurations can be used for the separation and purification of gas streams. The appropriate configuration depends on factors such as the adsorbate–adsorbent interaction, feed conditions, required product purity, regeneration requirements, and energy consumption. Among the available cyclic adsorption processes, Pressure Swing Adsorption (PSA) and Temperature Swing Adsorption (TSA) are widely used for gas separation and purification. Variations such as Vacuum Pressure Swing Adsorption (VPSA) and Vacuum Temperature Swing Adsorption (VTSA) can provide an additional driving force for regeneration.

The main distinction between these processes is the variable used to shift the adsorption equilibrium during regeneration. PSA relies primarily on a reduction in pressure, whereas TSA uses an increase in temperature. The effectiveness of either strategy therefore depends strongly on the adsorption equilibrium of the adsorbate–adsorbent system. For hydrogen drying, this is particularly important because water is strongly adsorbed by hydrophilic adsorbents at low partial pressures.

2.2.1. Pressure Swing Adsorption

Pressure Swing Adsorption (PSA) is a cyclic separation process in which differences in adsorption affinity are combined with changes in pressure to separate components from a gas mixture. Consider a binary gas mixture passing through a packed bed containing a selective adsorbent. The component with the stronger affinity for the adsorbent is preferentially retained within the bed, while the weakly adsorbed component passes through the column and is recovered as the product stream [18]. The separation performance therefore depends on the adsorption equilibrium, mass transfer behaviour, and physical properties of the adsorbent, including its pore structure and surface area.

During the adsorption step, the feed gas is introduced into the column at an elevated pressure. For systems in which adsorption is favoured by increasing pressure, the equilibrium loading of the strongly adsorbed component increases with its partial pressure [6]. As the gas passes through the bed, the more strongly adsorbed component is retained and a mass transfer zone (MTZ) develops and propagates through the column. Adsorption cannot continue indefinitely because the adsorbent progressively approaches its equilibrium loading under the adsorption conditions. The bed must therefore be regenerated before the adsorbed component reaches an unacceptable concentration in the product stream.

In PSA, regeneration is achieved primarily by reducing the pressure of the adsorption bed. Depres-

surisation decreases the partial pressure of the adsorbed species and shifts the adsorption equilibrium towards a lower equilibrium loading, thereby promoting desorption. The difference between the equilibrium loading under adsorption and regeneration conditions is commonly referred to as the *working capacity* of the adsorbent. Conceptually, for an approximately isothermal pressure swing, it can be expressed as

$$\Delta q_{\mathrm{PSA}} = q^*(P_{\mathrm{ads}}, T) - q^*(P_{\mathrm{des}}, T), \tag{2.1}$$

where Δq_{PSA} is the equilibrium working capacity, q^* is the equilibrium adsorbed loading, P_{ads} is the adsorption pressure, P_{des} is the regeneration pressure, and T is the bed temperature. In an actual dynamic PSA cycle, the usable working capacity can differ from this equilibrium value because of mass transfer limitations, pressure gradients, temperature changes, and the finite duration of each cycle step.

A typical PSA cycle consists of adsorption, depressurisation or blowdown, regeneration, and repressurisation [19]. A purge step may also be introduced during regeneration, in which a fraction of the purified product gas is passed through the bed to assist in removing the desorbed species [18]. Following regeneration, the column is repressurised using feed gas, purified product gas, or a combination of streams before the next adsorption step begins. The exact sequence and duration of these steps depend on the required product purity, recovery, and characteristics of the adsorbate–adsorbent system.

For hydrogen drying, hydrogen is the weakly adsorbed carrier gas while water is the strongly adsorbed impurity. During adsorption, water is preferentially retained by the adsorbent and dry hydrogen is recovered as the product. During regeneration, reducing the total pressure also reduces the partial pressure of water and therefore lowers its equilibrium loading. The effectiveness of PSA for hydrogen drying consequently depends on whether the achievable pressure reduction produces a sufficiently large decrease in water loading to restore the required working capacity of the adsorbent.

This consideration becomes particularly important for strongly hydrophilic adsorbents. Although strong water affinity is advantageous for achieving very low outlet moisture concentrations, substantial water loading may remain even after conventional depressurisation. In such cases, deeper pressure reduction, vacuum-assisted regeneration, increased temperature, or a combination of these approaches may be required to obtain sufficient desorption.

PSA is an established industrial gas separation technology and can offer advantages such as relatively short cycle times, compact equipment, and the absence of direct thermal regeneration of the adsorbent [20]. However, its overall performance and energy requirement depend on the required pressure ratio, compression or vacuum duty, product gas consumed during purge and repressurisation, and the extent of regeneration achieved during each cycle..

2.2.2. Temperature Swing Adsorption

Temperature Swing Adsorption (TSA) is a cyclic adsorption process in which regeneration is achieved primarily by increasing the temperature of the adsorbent bed. Similar to PSA, the separation is based on the preferential adsorption of one or more components from a gas mixture. The principal difference is the variable used to shift the adsorption equilibrium during regeneration: PSA primarily relies on a reduction in pressure, whereas TSA uses an increase in temperature.

Adsorption is generally favoured at lower temperatures for exothermic adsorption systems. During the adsorption step, the feed gas is passed through the bed at the selected adsorption temperature, where the more strongly adsorbed component is preferentially retained. As the bed approaches its usable adsorption capacity, regeneration is required before the adsorbate reaches an unacceptable concentration in the product stream.

During TSA regeneration, heat is supplied to the adsorption bed. The increase in temperature shifts the adsorption equilibrium towards a lower equilibrium loading, thereby promoting desorption of the retained species. A regeneration or purge gas can subsequently be used to remove the desorbed species from the bed. Conceptually, the equilibrium working capacity associated with a temperature swing can be expressed as

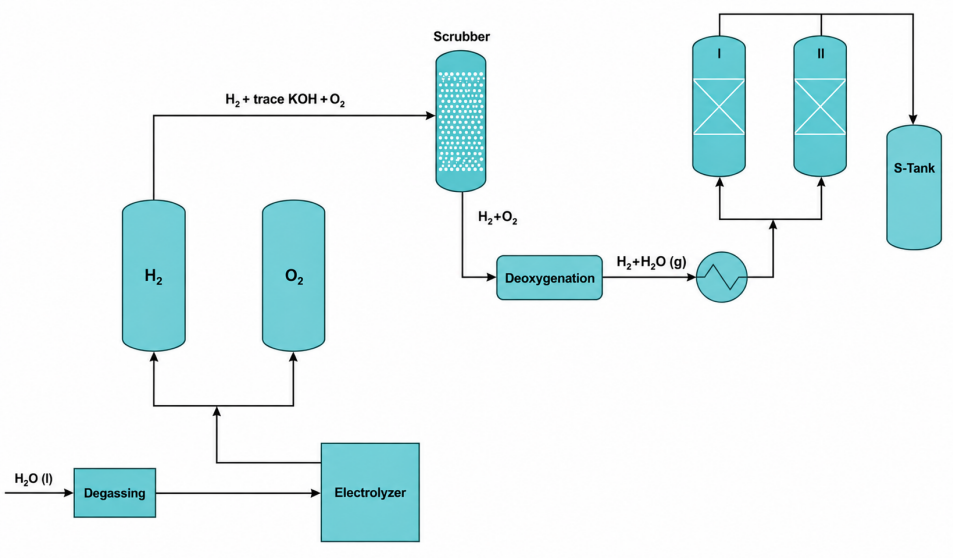

Figure 2.2: Process Flow Diagram of PSA

$$\Delta q_{\mathrm{TSA}} = q^*(P, T_{\mathrm{ads}}) - q^*(P, T_{\mathrm{regen}}), \tag{2.2}$$

where Δq_{TSA} is the equilibrium working capacity, q^* is the equilibrium adsorbed loading, P is the operating pressure, T_{ads} is the adsorption temperature, and T_{regen} is the regeneration temperature. In practice, the usable working capacity also depends on factors such as heat and mass transfer, purge conditions, temperature distribution within the bed, and the duration of the regeneration step.

A typical TSA cycle consists of the following principal steps:

- Pressurisation,
- Adsorption,
- Heating and desorption,
- Cooling.

Depending on the process configuration, additional depressurisation, purging, or repressurisation steps may also be incorporated into the cycle.

Following thermal regeneration, the adsorbent bed must be cooled before the subsequent adsorption step because adsorption capacity generally increases as the temperature is reduced. Consequently, both heating and cooling contribute to the overall TSA cycle duration. The relatively slow thermal response of a packed adsorption bed can result in cycle times of several hours and is one of the principal limitations of TSA compared with pressure driven adsorption processes [8].

The regeneration temperature required in a TSA process depends on the adsorbate–adsorbent interaction and the desired extent of regeneration. Strongly adsorbed species may require substantial temperature increases to achieve sufficient desorption. For example, Kheimi et al. reported regeneration temperatures of approximately $350\,^{\circ}\mathrm{C}$ for the adsorption system investigated in their study [21]. Such temperatures should, however, be regarded as system specific rather than as a general requirement for TSA operation.

The requirement to heat and subsequently cool the adsorbent bed introduces additional energy consumption compared with regeneration based solely on pressure reduction. Repeated temperature cycling can also impose thermal stress on the adsorbent and process equipment, while the longer heating and cooling periods can reduce cycle frequency and consequently influence process productivity. The magnitude of these effects depends strongly on the regeneration temperature, adsorbent properties, bed dimensions, heat transfer characteristics, and process configuration.

For hydrogen drying, however, thermal regeneration can be advantageous when water is strongly retained by a hydrophilic adsorbent. Increasing the temperature can substantially reduce the equilibrium water loading, providing an additional regeneration driving force when pressure reduction alone does not produce sufficient desorption. The suitability of TSA for hydrogen drying therefore depends on the balance between improved adsorbent regeneration and the additional thermal energy, cooling time, and process complexity associated with temperature cycling.

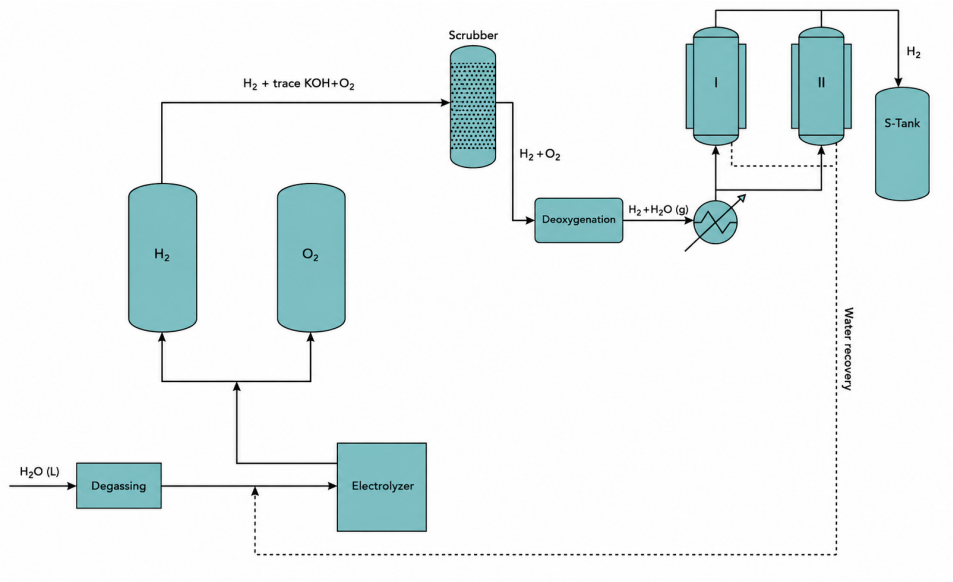

Figure 2.3: Process Flow Diagram of TSA

Table 2.1: Summary of advantages and disadvantages of PSA and TSA for hydrogen drying.

Technology	Advantages	Disadvantages
PSA	Short cycle times, low energy consumption, high productivity, compact system design, and mature industrial implementation.	Potential hydrogen losses during purge and depressurisation, less effective regeneration for strongly adsorbed water, and multiple valves and controll system.
TSA	Effective regeneration of strongly adsorbed water, excellent deep drying capability, and high hydrogen recovery.	High heating and cooling requirements, long cycle times, lower productivity, and larger equipment.

2.2.3. Vacuum Pressure Swing Adsorption

Vacuum Pressure Swing Adsorption (VPSA) is a variation of Pressure Swing Adsorption in which the regeneration pressure is reduced below atmospheric pressure. The fundamental separation mechanism is therefore the same as that of PSA, but the use of vacuum provides a larger pressure swing between the adsorption and regeneration conditions.

During regeneration, reducing the bed pressure below atmospheric pressure decreases the partial pressure of the adsorbed species. This shifts the adsorption equilibrium towards a lower equilibrium loading and can therefore increase the driving force for desorption. Compared with conventional PSA, where regeneration may be limited to pressures close to atmospheric pressure, VPSA can consequently provide more extensive regeneration of the adsorbent.

This behaviour can be particularly relevant for strongly adsorbed species such as water vapour. In hydrogen-drying applications, reducing the water partial pressure through vacuum-assisted regeneration may enable greater desorption than conventional depressurisation and can therefore be useful when very low residual water concentrations are required [1]. However, the extent of the improvement depends on the adsorption equilibrium and on how strongly water remains adsorbed at the selected regeneration pressure.

The additional regeneration driving force provided by VPSA must be balanced against the requirements associated with vacuum generation. Vacuum pumps increase equipment complexity and capital cost and introduce an additional energy requirement. Furthermore, progressively deeper vacuum conditions generally require greater vacuum duty. Consequently, the appropriate regeneration pressure represents a trade-off between improved adsorbent regeneration and the additional energy and equipment required to achieve the vacuum conditions [1].

For deep hydrogen drying, VPSA therefore provides an intermediate regeneration strategy between conventional pressure swing operation and thermal regeneration. Its feasibility depends on whether the reduction in water partial pressure is sufficient to restore the required adsorbent working capacity without requiring impractically deep vacuum conditions.

2.2.4. Vacuum Temperature Swing Adsorption

Vacuum Temperature Swing Adsorption (VTSA) is a hybrid regeneration strategy that combines the temperature variation used in TSA with sub-atmospheric pressure during desorption. The process therefore uses two thermodynamic driving forces for regeneration: an increase in temperature and a reduction in adsorbate partial pressure.

During adsorption, the bed is operated at a relatively low temperature, where adsorption of the target species is favoured. During regeneration, the bed temperature is increased while vacuum is simultaneously applied. The elevated temperature reduces the equilibrium adsorption capacity, while the reduction in pressure lowers the partial pressure of the adsorbed species. The combined effect can therefore promote more extensive desorption than either temperature or pressure variation alone [22].

For strongly adsorbed species such as water vapour, this combined regeneration strategy can be particularly useful because the reduction in equilibrium loading obtained by heating is reinforced by the lower partial pressure created by the vacuum. As a result, VTSA may allow the required degree of regeneration to be achieved at a lower temperature than would otherwise be necessary in a conventional TSA process.

The potential reduction in regeneration temperature can decrease the thermal duty imposed on the adsorbent and may also reduce thermal stress during repeated cycling. However, the use of vacuum introduces additional equipment, capital cost, and electrical energy consumption. Consequently, the total energy requirement of a VTSA process depends on the balance between the reduced thermal regeneration requirement and the additional vacuum duty [21].

VTSA therefore offers a potentially effective regeneration strategy for systems in which the adsorbate is strongly retained by the adsorbent. Its practical suitability depends on the required regeneration temperature, vacuum level, cycle duration, and the associated energy and equipment requirements.

2.3. Adsorbents and Water sorption properties

The suitability of an adsorbent depends on several physical and chemical properties, including specific surface area, pore-size distribution, pore accessibility, and surface chemistry. A high specific surface area generally provides more potential adsorption sites [23], but this does not necessarily lead to higher adsorption if the pores are too small or inaccessible to the adsorbate molecules [24]. Pore structure influences both adsorption capacity and mass-transfer rates. Micropores contribute strongly to adsorption capacity, while mesopores and macropores can facilitate transport of adsorbate molecules through the particle [24]. Surface chemistry also affects selectivity, since polar or functional surface groups can increase the affinity of the adsorbent towards specific molecules.

For water adsorption, these properties act together to determine the hydrophilicity, adsorption capacity, and transport behaviour of the material. Therefore, adsorbent selection should consider the combined effect of pore structure, accessible surface area, and surface chemistry rather than maximising a single property.

A wide range of porous materials has been investigated for water adsorption, with significant differences in their hydrophilicity, adsorption capacity, and low-pressure uptake behaviour. The following sections compare the water adsorption characteristics and representative isotherms of porous carbons, silica gel, zeolites, and metal-organic frameworks (MOFs) in order to assess their suitability for hydrogen drying.

Porous Carbons: Porous carbon materials have been extensively studied for water adsorption both experimentally and theoretically [25]. In general, they exhibit low water uptake at low relative pressures, reflecting their comparatively hydrophobic character. Their water adsorption behaviour is therefore commonly associated with an S-shaped Type V isotherm. Water adsorption on porous carbons typically proceeds progressively, beginning with adsorption at surface or functional-group sites, followed by clustering and pore filling as the relative pressure increases. At sufficiently high relative pressure, the pores approach saturation. Both microporous and mesoporous carbons can exhibit this characteristic S-shaped behaviour, although the total water uptake is influenced by pore size and available pore volume. Mesoporous carbons can accommodate larger quantities of water because of their greater accessible pore volume [26].

The relatively low water uptake of porous carbons at low partial pressures limits their suitability for deep hydrogen drying, where strong water affinity is required even at very low moisture concentrations.

Silica Gel: Silica gel is a widely used inorganic adsorbent for moisture removal because of its strong affinity for water [27]. Its surface contains silanol groups (Si–OH), which are hydrophilic and provide active sites for water adsorption. Depending on its surface chemistry and pore structure, silica gel can exhibit different water adsorption isotherm shapes, including Type I, II, IV, and S-shaped behaviour. Such behaviour has also been reported by Tashiro et al. for silica gel used in desiccant cooling applications [28].

For many commercial silica gels, a substantial increase in water uptake occurs at moderate to high relative pressures. This provides good moisture-removal capacity under relatively humid conditions but can make silica gel less effective for deep drying when the water partial pressure becomes very low. Consequently, silica gel is often more suitable for bulk moisture removal or pre-drying than for achieving extremely low residual water concentrations in hydrogen..

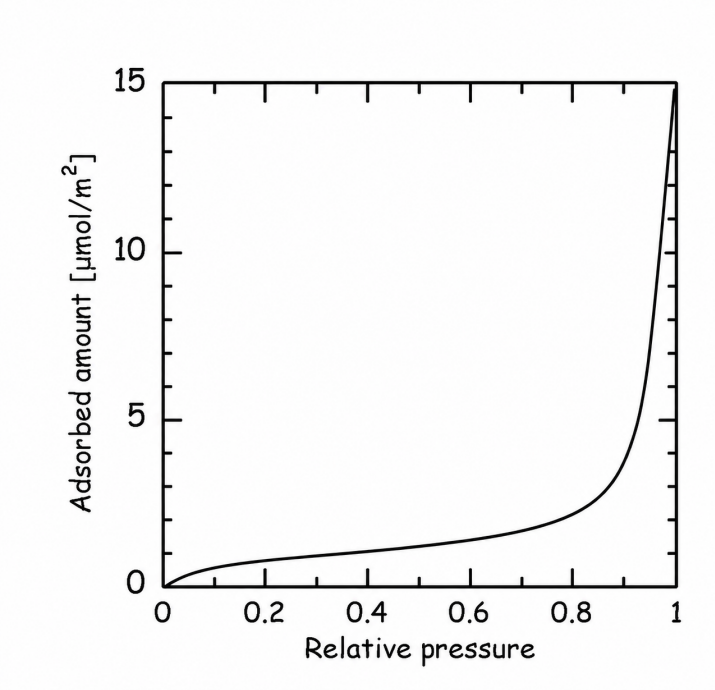

Figure 2.4: Adsorption isotherm of porous carbon adapted from [26]

Zeolites Zeolites are crystalline aluminosilicate materials composed of interconnected SiO_4 and AlO_4 tetrahedra, forming a rigid framework with well-defined micropores. The presence of aluminium in the framework produces a negative structural charge that is balanced by exchangeable cations. These cations create strongly polar adsorption sites and contribute to the high affinity of many zeolites for water. Consequently, zeolites commonly exhibit Type I water adsorption behaviour, characterised by substantial uptake at low relative pressures.

Zeolites 3A, 4A, and 5A are among the most widely studied molecular sieves and have been extensively applied in gas separation and drying processes. Zeolite A is commonly produced in its sodium form and is referred to as zeolite 4A because of its approximate pore opening of 4 Å. Partial ion exchange of Na^+ with Ca^{2+} produces zeolite 5A, with an approximate pore opening of 5 Å, whereas exchange with K^+ produces zeolite 3A, with an approximate pore opening of 3 Å[30]. These materials exhibit molecular-sieving behaviour, whereby molecules smaller than the pore opening can enter the internal pore structure while larger molecules are excluded.

Zeolites X and Y have also been extensively investigated for water adsorption because of their high pore volume and strong hydrophilic behaviour [32, 26]. In addition to zeolite type and pore structure, the preparation method and resulting structural defects can influence water adsorption performance. Defects in the crystalline framework may create additional adsorption sites and free volume, thereby promoting water adsorption, hydrogen bonding, and clustering within the pore structure [33].

Hydrothermal stability is another important consideration, particularly when zeolites are subjected to repeated heating and cooling during regeneration. The stability of the zeolite framework is influenced by its Si/Al ratio. Zeolites with lower Si/Al ratios generally exhibit lower hydrothermal stability because Si–O–Al bonds are more susceptible to hydrolysis and framework degradation than Si–O–Si bonds [34].

The strong water affinity of zeolites at low partial pressures makes them particularly suitable for deep gas-drying applications. However, the same strong adsorbate–adsorbent interactions that favour water removal can also increase the severity of the conditions required for regeneration. Therefore, both adsorption capacity and regenerability must be considered when selecting a zeolite for cyclic hydrogen-drying processes.

Metal Organic Frameworks(MOFs) have emerged as a promising class of porous materials for water

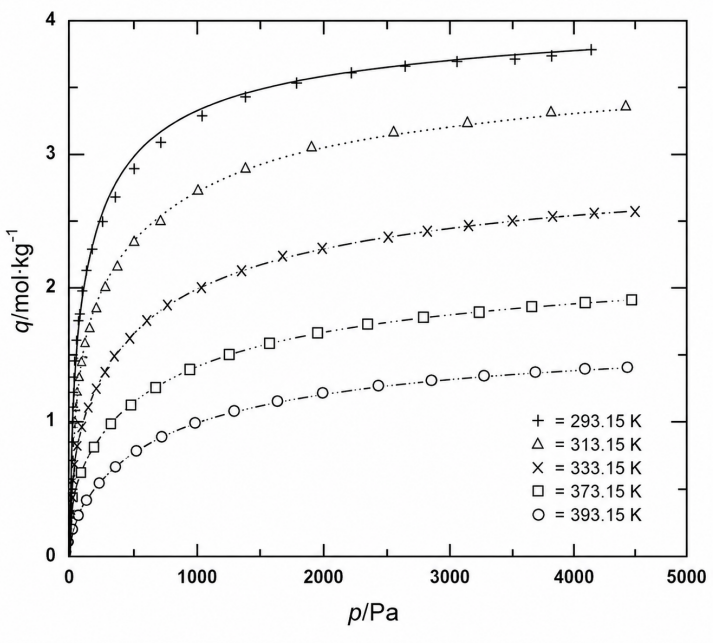

Figure 2.5: Adsorption isotherm on Silica Gel adapted from [29]

vapor adsorption due to their tuneable pore structures, exceptionally high surface areas and can also be fine tuned to obtain isotherm of a particular shape. Structural designability of MOFs are the plus point and hence allow extensive research and development of various chemically stable MOFs. Bottlenecks have been observed with MOFs with their poor water stability. A range of water adsorption isotherm can be observed for MOFs due to their structural design which comes different degree of hydrophobicity and hydrophilicity. These water isotherms related to MOFs vary in shape, water loading capacity, steepness of the curve and hysteresis can give MOFs various advantages in different water-based applications such as water harvesting and humidity control to gas purification and drying. To remove water from other molecules the inflection point should appear at very low relative pressures. Hence design of MOFs requires fine tuning of adsorption sites, their optimal total pore volume for water adsorption. Due to this dual nature of MOFs, they often require careful tuning of adsorption sites, optimization of pore size and volume, and control over the distribution of hydrophilic and hydrophobic regions within the framework. The inflection point (rapid water uptake) occurs mainly when the relative pressure crosses 0.1 or relative humidity of 10% [35].

The adsorption isotherms presented for porous carbons, silica gels, zeolites, and MOFs demonstrate significant differences in water adsorption behaviour, hydrophilicity, adsorption capacity, and adsorption mechanisms. These differences strongly determine the suitability of adsorbents for hydrogen drying applications using PSA or TSA technologies.

The adsorption isotherm for porous carbon materials demonstrates relatively low water uptake at low relative pressures, reflecting weak interaction between water molecules and the carbon surface. This behaviour shows hydrophobic nature of carbon adsorbents resulting in limited affinity toward polar water molecules. The delayed increase in adsorption uptake and the position of the inflection point at high relative pressures further confirm the hydrophobic nature of porous carbon materials. As the pressure approaches unity, a sharp increase in water uptake can be observed which may be due to pore filling on carbon surface rather than strong affinity of carbon towards water molecule. For hydrogen drying applications, this behaviour presents an important limitation since hydrogen streams generally contain water at very low partial pressures. Adsorbents used for hydrogen purification must exhibit strong water uptake in the low-pressure region to achieve ultra-high purity hydrogen specifications such as mentioned in ISO 14687. Although there is weaker interaction of carbon surface with water molecule, this can result in less regeneration energy for the carbon based adsorbents and improve cyclic stability in adsorption-desoprtion operation.

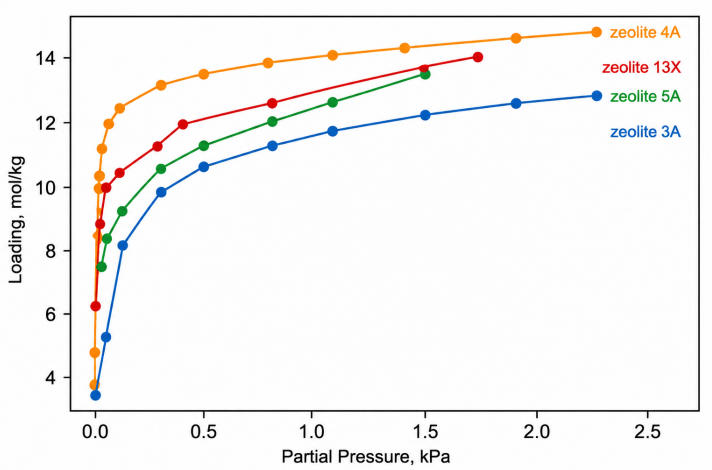

Figure 2.6: Water adsorption isotherms of Zeolite 3A, 4A, 5A, and 13X, adapted from [30, 31].

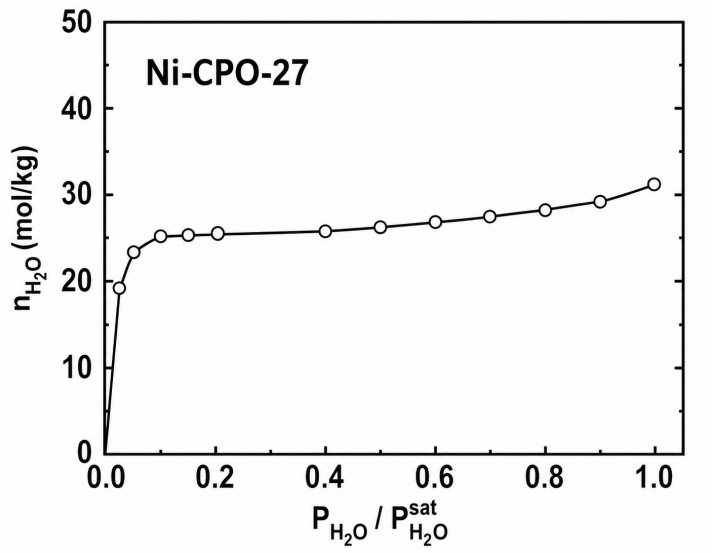

Figure 2.7: Adsorption isotherm of Metal Organic Framwork Ni-CPO-27 adapted from [36]

The adsorption isotherm of silica gel shows relatively high water uptake at low partial pressures, indicating hydrophilic behaviour and strong affinity between water molecules and the silica gel surface. Compared to porous carbons, silica gel shows a much steeper initial uptake region, suggesting stronger adsorbent water interactions and improved adsorption performance.Another important observation from the isotherm is the influence of temperature on adsorption capacity. As temperature increases from 293.15 K to 393.15 K, the adsorption uptake decreases significantly. This behaviour confirms the exothermic nature of water adsorption, where increasing temperature weakens the interaction between water molecules and the adsorbent surface reducing adsorption capacity. Generally, silica gel is widely used for pre-drying applications where it is used to remove a large portion of the moisture initially present in the gas stream before final ultra high purity drying stages. In multi stage drying systems, silica gel is often used as a first drying stage to reduce the water load on more strongly hydrophilic adsorbents which are then used for deep drying to achieve extremely low residual moisture concentrations required for high-purity applications.

The adsorption isotherms for Zeolite show that all zeolite materials exhibit very high water uptake at low partial pressures reflecting strongly hydrophilic behaviour and strong affinity toward water molecules. This behaviour is due to the electrostatic interaction between water molecules and the charged zeolite framework. Among the zeolites shown, zeolite 4A demonstrates the highest water adsorption capacity

followed by zeolite 13X, 5A, and 3A. The steep uptake observed at very low partial pressures suggests that zeolites are highly suitable for deep hydrogen drying applications where very low moisture concentrations must be achieved. However, this strong adsorption behaviour results in higher heats of adsorption which may increase regeneration energy requirements during cyclic operation.

The adsorption isotherm of MOFs shows high water uptake at low relative pressures, indicating moderate to high hydrophilic behaviour and strong affinity between water molecules and the MOF structure. The sharp initial increase in adsorption suggests the presence of highly active adsorption sites and favourable pore structures for water adsorption.

2.4. Recent Advances in Adsorbents

There has been a lot of advances in adsorbent material, a lot of researchers have looked into doping of adsorbent material which will help in more activation sites or more hydrophilic nature of adsorbents.

Covalent organic frameworks(COFs) and porous organic polymer (POPs) are carbon based material that has seen advances in water adsorption due to their stability for water molecules [37]. Doping COFs with hydrophilic groups increases the water uptake capacities. Karak et al. found that COFs acquire higher surface are when they used p-toluenesulfonic acid as a catalyst [38]. These material exhibited type 2, 4 and 5 isotherms. When polar functional groups like N and O are added making the pore structure more hydrophilic, the adsorbent amount was noticed to rise quickly at lower relative pressure giving inflection point at 0.2. in addition to crystalline COFs, POPs have also attracted significant attention in the last decade due to their stability in humid conditions. Like any other cabon based porous material which exhibit type 5 isotherm, POP also show the same result but were found to have higher water uptake capacity due to their mesopore structure such as CPOP-9 [39]. Depending on what type of functional group used to make POPs, both surface area of the pores and polarity of the surface can be fine-tuned leading to different water adsorption isotherms.

SILICA GEL: To enhance water adsorption capacity of silica gel several modifications such as using composite materials like hygroscopic salts (alkali, bromides, sulfates, nitrates) along with silica gel were studied. These resulted in increased water uptake compared to pure silica gel and the study also showed that amount of salt used and present within the pores had direct relation to water adsorption capacity [27]. Mesoporous silica materials are also preferred for their higher water uptake capacity. When different pore size and variable dimensions were tested for silica based materials, they showed positive result as opposed to microporous materials. Effect of Si/Al ratio also had great impact on the adsorption capacity, and it was determined that when Al content is less in mesoporous silica they showed increase in steepness of the slope of isotherm [40].

ALUMINOPHOSPHATES(AlPOs) and SILICA-ALUMINOPHOSPHATES(SAPOs): Potential alternatives of zeolites are AlPOs and SIPOs which have similar crystalline inorganic materials which can be considered for water related applications. SIPOs are more hydrophilic compared to AlPOs. This ability comes from the presence of counter cations in their frameworks and are generally shown to have an S type isotherm [39]. There has been some development and research to enchnace efficiency of adsorbents through varouis techniques. One such technique is known as Molecular Imprinted Polymers also known as MIPs. Imagine making a cast or die of certain molecule, this cast acts as an imprint for when the adsorption process takes place the adsorbate can easily attach itself in the cavity of the adsrobents. MIPs shows high selectivity and control over the selection process making this technique highly tunable [41].

2.5. Parameters for Adsorbent Selection

When selecting an adsorbent for water removal from hydrogen gas, several important parameters must be considered because they strongly affect the performance and efficiency of the adsorption process. One of the most important properties is the polarity of the adsorbent. Water is a highly polar molecule, while hydrogen is non-polar [42]. Therefore, adsorbents with a polar surface such as Zeolite shows a strong attraction toward water molecules and weak interaction with hydrogen. This allows water molecule to be adsorbed while hydrogen passes through the bed. Another important parameter is pore size and molecular size compatibility. The pores of the adsorbent must be large enough for water molecules to enter easily and diffuse through the structure. Uniform pore sizes are especially important

in molecular sieves improving selectivity towards water molecule and adsorption efficiency [43].

Adsorption capacity is also a key factor in adsorbent selection. A high adsorption capacity means that the material can adsorb a larger amount of water before reaching breakthrough conditions. This leads to longer operating cycles, reduced regeneration frequency. The adsorbent should also have high selectivity toward water over hydrogen in order to minimize hydrogen losses during the process. Adsorption and desorption kinetics are also important, especially in Pressure Swing Adsorption systems where cycle times are short. Fast kinetics allow water molecules to be adsorbed and desorbed quickly resulting in improved process efficiency and less cycle duration [44].

Thermal stability is another major requirement especially in Temperature Swing Adsorption systems. During TSA regeneration, the adsorbent is repeatedly heated(regeneration) and cooled(adsorption). Hence, the material must be able to withstand high temperatures and thermal cycling without losing its structure or adsorption performance [21]. Moreover, the adsorbent should have good regenerability so that adsorbed water can be removed efficiently during regeneration and the material can be reused for many cycles without significant loss of performance. Another important property is the heat of adsorption [44]. Water adsorption is an exothermic process, meaning that the heat is released during adsorption. A high heat of adsorption generally indicates strong interaction between water and the adsorbent, which improves water removal performance. However, it can also increase the energy required for regeneration.

Table 2.2: Comparison of major adsorbent classes used in gas drying and separation processes.

Adsorbent Class	**Advantages**	**Disadvantages**
Zeolites	High water adsorption capacity, strong hydrophilicity, excellent thermal stability, well established industrial use, and suitable for deep drying applications.	Strong water adsorption can increase regeneration energy requirements, and adsorption performance may decrease in the presence of competing species.
Silica Gel	Low cost, easy regeneration, high moisture capacity at moderate and high relative humidities, and widespread commercial availability.	Lower affinity for water at very low partial pressures, making it less suitable for ultra-deep drying applications.
Activated Carbon	Large surface area, relatively inexpensive, effective for adsorption of organic compounds.	Generally hydrophobic and therefore exhibits limited water adsorption capacity compared with zeolites and silica gel.
Metal Organic Frameworks (MOFs)	Highly tunable pore structures and surface chemistry, potentially high adsorption capacities, and promising performance for selective separations.	High material cost, limited large-scale industrial deployment, and concerns regarding long-term stability for some MOF structures.
Activated Alumina	Good mechanical strength, moderate water adsorption capacity, and relatively low cost.	Typically exhibits lower adsorption capacity and selectivity compared with zeolites for deep drying applications.

2.6. Challeneges

As mentioned earlier, International Organization for Standardization (ISO) developed the ISO 14687 standard, which specifies hydrogen purity requirements for fuel cell applications and defines the maximum allowable concentration of impurities that may cause degradation of fuel cells. As a result, efficient hydrogen purification and drying technologies are becoming increasingly important for large scale hydrogen deployment. Several studies have investigated purification techniques such as Pressure Swing Adsorption and Temperature Swing Adsorption individually, discussing their operating principles, advantages, and limitations [3, 7, 8] . However, only limited studies provide direct side by side comparison of

PSA and TSA systems under similar operating conditions. Therefore, further comparative studies are required to better understand which purification technique is more suitable for hydrogen drying under specific operating conditions considering their economics as well.

Another important challenge reported in literature is the scale-up of adsorption systems from laboratory to industrial operation. Most experimental studies are performed using small laboratory columns while industrial adsorption systems often involve multiple large columns operating in parallel with complex valve sequencing and cyclic operation [20]. As the size and number of adsorption columns increase, the overall process becomes more complex. Large columns may experience heat and flow maldistribution, resulting in incomplete utilization of the adsorbent bed. Moreover, mass transfer and heat transfer become more significant at industrial scale. Since adsorption is an exothermic process, temperature gradients inside large columns may reduce adsorption capacity and affect breakthrough behavior significantly. Especially in TSA systems regeneration requires significant thermal energy input to heat the adsorbent bed for desorption of impurities. Industrial adsorption systems also require advanced control systems capable of handling valve timing, pressure equalization steps, and synchronization of multiple adsorption beds operating simultaneously.

Growing research on adsorption processes and gas purification techniques has improved the understanding of cyclic adsorption systems. However, only limited studies have investigated green hydrogen purification using detailed simulation platforms such as Aspen Adsorption. Many published studies rely on simplified assumptions or custom models, which may reduce reproducibility between different research groups. In addition operating conditions, adsorbent materials, and model assumptions often vary significantly across studies, making direct comparison [21]. Although Aspen Adsorption includes built-in adsorbent libraries and allows detailed simulation of cyclic multi-bed adsorption systems, published studies involving hydrogen drying from water electrolysis remain limited. Most adsorption simulation studies focus on air separation, carbon capture, or general gas drying applications, while comparatively fewer studies investigate green hydrogen drying systems [45, 46].

Published techno-economic studies on adsorption systems consistently show that energy consumption is one of the dominant cost contributors in adsorption-based processes. Large amounts of electricity and thermal energy are required for compression, vacuum generation, heating, and regeneration of adsorbents [47]. Another major point from literature is that adsorbent properties strongly influence economic performance. High-capacity and highly selective adsorbents reduce bed size, regeneration frequency, and cycle time, leading to reduced capital and operating cost [48]. Some studies also mention improved adsorbent performance lowers energy demand. These findings indicate that realistic adsorbent characterization is essential in techno-economic analysis [49, 50]. There is a clear trade off between product purity, recovery, and process cost as well. Achieving very high purity levels often requires additional regeneration energy, larger adsorption columns, or longer cycle times, which increases overall cost. Bashir et al. reported that increasing hydrogen purity from 98% to 99.3% reduced hydrogen recovery significantly, thereby affecting overall process economics. Finally, published literature also mentions that scale-up substantially increases process complexity [51]. Many laboratory scale studies do not completely account for industrial requirements such as multi-bed operation, valve sequencing, instrumentation, piping networks, and control systems [52] . Overall, literature suggests that although adsorption systems generally benefit from economies of scale, accurate industrial-scale techno-economic analysis must include realistic balance-of-plant and operational considerations.

The modeling of Pressure Swing Adsorption and Temperature Swing Adsorption systems for hydrogen drying involves several important challenges that can affect the accuracy and reliability of the simulation results. One of the major challenges is the limited availability of experimental adsorption equilibrium data for the H_2/H_2O system. Although adsorption data are available for many gas systems, only limited studies provide detailed water uptake data in hydrogen streams, especially at industrial operating conditions. This results in difficulties in accurately describing the adsorption behavior of water on adsorbents such as zeolites. Moreover, very accurate adsorption isotherm parameters are required as input for Aspen Adsorption simulations [53]. However, the lack of experimental uptake data as a function of water partial pressure and temperature makes it difficult to fit adsorption isotherm models such as Langmuir or Toth and obtain reliable isotherm parameters [54, 55]. As a result, many studies rely on assumptions, extrapolated data, or parameters obtained under different operating conditions, which can reduce model accuracy.

Another major challenge is the validation of PSA and TSA models. Experimental breakthrough curves and cyclic adsorption data for green hydrogen drying systems are limited in the literature, while industrial data are often propriatary and hence confidential. Therefore, validating simulation results against real experimental systems becomes difficult. Several studies emphasize the importance of validating adsorption models using experimental isotherms and breakthrough data in order to improve simulation reliability [54, 56]. Furthermore, PSA and TSA processes involve complex multicomponent adsorption behavior where adsorption equilibrium, mass transfer, heat transfer, and pressure variations occur simultaneously inside the adsorption bed. These coupled phenomena make the systems highly dynamic and difficult to model accurately. Water adsorption is also strongly exothermic, causing temperature changes inside the bed which influence adsorption equilibrium and breakthrough behavior. Therefore, non-isothermal modeling is often required for realistic simulation of adsorption systems [57].

Another important issue in PSA and TSA simulations is the difficulty of reaching cyclic steady state (CSS). Since adsorption systems operate cyclically which means to reach stable operating conditions to achieve sensible results, the simulation must often run for many cycles before stable repeating conditions are achieved. This increases computational time and may lead to numerical instability and convergence problems. Previous studies have shown that CSS calculations are computationally intensive and require careful numerical discretization and solver selection [58]. Moreover, commercial simulation tools such as Aspen Adsorption are highly complex and require detailed understanding of equilibrium models, kinetic models, discretization methods, solver settings, and cycle organization. Although Aspen Adsorption is widely used for cyclic adsorption simulations, detailed methodological guidance and application examples for hydrogen drying systems remain limited, creating additional challenges for new users. Finally, another challenge is scaling laboratory-scale models to industrial systems. Laboratory experiments are usually performed under controlled and simplified conditions, while industrial systems may involve larger beds, temperature gradients, pressure drops, and flow maldistribution. Therefore, simulation models developed at lab scale may not always accurately predict industrial-scale performance [56, 57, 54].

The literature shows that adsorption-based processes are suitable for removing water from hydrogen. Zeolites are particularly attractive for deep drying because they have a strong affinity for water at low partial pressures. PSA offers short cycle times and relatively low energy consumption, whereas TSA provides more effective regeneration of strongly adsorbed water but requires heating and cooling.

However, limited information is available on the detailed non-isothermal modelling of water removal from electrolytic hydrogen using Aspen Adsorption. Experimental equilibrium and cyclic data for the $\mathrm{H_2 - H_2O}$ system are also limited. In addition, many published studies do not include realistic multi-bed operation, energy requirements, hydrogen consumption, and techno-economic performance. These limitations create a need for a detailed simulation-based assessment of hydrogen drying using TSA.

3

Methodology

The green hydrogen drying process was modelled in Aspen Adsorption, a dynamic flowsheet simulation package developed by AspenTech for the design and analysis of cyclic adsorption processes [59]. The model consisted of a packed adsorption column containing zeolite 4A, together with feed, product, purge and waste streams. valves were connected to the column boundaries to regulate the gas via constant flow or by specifying linear valve coefficient during adsorption, depressurisation, regeneration, cooling and repressurisation.

3.1. Component and Feed-Gas Definition

Hydrogen and water were selected as the gas phase components in the Aspen Adsorption model. Hydrogen was treated as the carrier gas and as a non adsorbing species, whereas water was treated as the adsorbing component. Adsorption of hydrogen on zeolite 4A was neglected because the objective of the study was the removal of trace quantities of water from a hydrogen rich gas stream. Under the selected operating conditions, the adsorption effect of hydrogen was assumed to be insignificant compared with the strong affinity of zeolite 4A for water.

The simulated feed represented wet hydrogen produced by water electrolysis after preliminary gas-treatment steps. Ligen et al. reported the operation of a $50\,\mathrm{kW}$ McPhy McLyzer 10-10 alkaline electrolyser at a pressure of approximately $10\,\mathrm{bar}$. The associated post-treatment system included the removal of potassium hydroxide droplets using a scrubber, the catalytic recombination of residual oxygen with hydrogen and the further removal of liquid water using a coalescing filter. A hydrogen dew point of approximately $5\,^{\circ}\mathrm{C}$ was reported following these treatment steps [1].

The reported dew point was used to estimate the residual water concentration in the hydrogen stream. At the dew point temperature, the partial pressure of water in the gas is equal to the saturation vapour pressure of water at the same temperature:

$$p_{\mathrm{H_2O}} = p^{\mathrm{sat}}_{\mathrm{H_2O}}\left(T_{\mathrm{dp}}\right) \tag{3.1}$$

where $p_{\mathrm{H_2O}}$ is the partial pressure of water, $p^{\mathrm{sat}}_{\mathrm{H_2O}}$ is the saturation vapour pressure of water, and T_{dp} is the dew-point temperature.

At a dew point of $5\,^{\circ}\mathrm{C}$, the saturation vapour pressure of water is approximately [60]:

$$p^{\mathrm{sat}}_{\mathrm{H_2O}}\left(5\,^{\circ}\mathrm{C}\right) = 8.719 \times 10^{-3}\ \mathrm{bar} \tag{3.2}$$

Using Dalton's law, the mole fraction of water was calculated as:

$$y_{\mathrm{H_2O}} = \frac{p_{\mathrm{H_2O}}}{P_{\mathrm{total}}} \tag{3.3}$$

Substituting the saturation pressure of water and the total gas pressure gives:

$$y_{\mathrm{H_2O}} = \frac{8.719 \times 10^{-3}}{10} = 8.719 \times 10^{-4} \tag{3.4}$$

The water concentration in parts per million by volume was subsequently calculated as:

$$y_{\mathrm{H_2O}} \times 10^{6}, \tag{3.5}$$

which gives:

$$871.9 \text{ ppm} \approx 872 \text{ ppm}. \tag{3.6}$$

Because the feed gas was assumed to contain only hydrogen and water, the hydrogen mole fraction was calculated as:

$$y_{\mathrm{H_2}} = 1 - y_{\mathrm{H_2O}}, \tag{3.7}$$

and therefore:

$$y_{\mathrm{H_2}} = 1 - 8.719 \times 10^{-4} = 0.999128 \tag{3.8}$$

The final feed composition used in the simulations was therefore a hydrogen mole fraction of 0.999128 and a water mole fraction of 8.72×10^{-4}.

Gas flow through a packed adsorption column is accompanied by variations in pressure, gas density, velocity, temperature and composition. These variations are important during dynamic steps such as depressurisation, heating, cooling and repressurisation. An appropriate thermodynamic property model is therefore required to calculate gas density, compressibility, enthalpy and other physical properties over range of operating pressures and temperatures experienced during the temperature swing adsorption cycle.

The ideal gas equation provides the simplest relationship between pressure, temperature and molar volume:

$$PV = nRT, \tag{3.9}$$

where (P) is the gas pressure, (V) is the gas volume, (n) is the number of moles, (R) is the universal gas constant and (T) is the absolute temperature.

Because the simulated gas consists mainly of hydrogen and only a trace amount of water, ideal gas behaviour could be a reasonable approximation. However the adsorption step was conducted at a relatively high pressure of 25 bar, while the column pressure changed during depressurisation and regeneration. Under these conditions, deviations from ideal gas behaviour could potentially affect the calculated gas density, compressibility, enthalpy and temperature of the adsorption column. The Peng–Robinson equation of state was therefore selected as the thermodynamic property method. It is a cubic equation of state that accounts for intermolecular attractive and repulsive forces and is applicable over a broad range of gas pressures and temperatures [61]. The general form of the Peng–Robinson equation is:

$$P = \frac{RT}{V_m - b} - \frac{a\alpha(T)}{V_m\left(V_m + b\right) + b\left(V_m - b\right)} \tag{3.10}$$

where (P) is the absolute gas pressure, (R) is the universal gas constant, (T) is the absolute gas temperature, and (V_m) is the molar volume of the gas, while (a), (b) and α are equation-of-state parameters that account for the attractive and repulsive interactions between molecules.

The component-specific parameters (a) and (b) are calculated from the critical properties of each component:

$$a = 0.45724\frac{R^2T_{\mathrm{c}}^2}{P_{\mathrm{c}}}, \tag{3.11}$$

$$b = 0.07780\frac{RT_{\mathrm{c}}}{P_{\mathrm{c}}}, \tag{3.12}$$

where T_c and P_c are the critical temperature and critical pressure of the component, respectively.

The temperature-dependent correction factor α is given by:

$$\left[1+\kappa\left(1-\sqrt{\frac{T}{T_c}}\right)\right]^2, \tag{3.13}$$

where κ is a function of the acentric factor ω:

$$\kappa = 0.37464 + 1.54226\omega - 0.26992\omega^2. \tag{3.14}$$

The use of the Peng–Robinson equation allowed the compressibility and enthalpy of the gas phase to be calculated more realistically than with the ideal-gas equation. This was particularly relevant for the non-isothermal model, where gas expansion, pressure changes, heat of adsorption and heat transfer together affected the temperatures of the gas and solid phases. The Peng–Robinson property method was therefore used consistently for the calculation of the gas-phase properties throughout the adsorption, depressurisation, regeneration, cooling and repressurisation steps [61]

3.2. Process Flowsheet

The basic process flowsheet consisted of a wet hydrogen feed stream connected to the inlet of the adsorption bed. The opposite end of the bed was connected to the product stream through which dried hydrogen was collected during the adsorption step. A purge stream was connected to the product end of the bed so that purge gas could flow counter current to the direction of the feed during regeneration. The waste stream was connected to the feed end of the bed and was used to discharge gas during depressurisation, blowdown and regeneration.

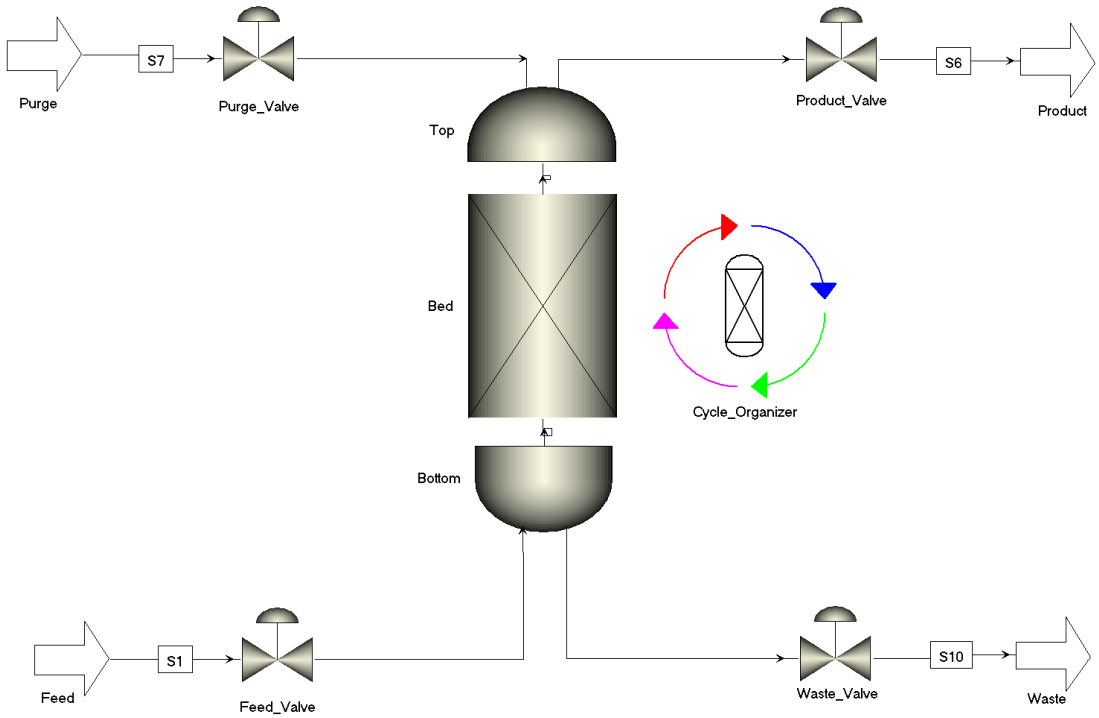

Figure 3.1: Aspen Adsorption flowsheet of the single-bed temperature swing adsorption process.

Valves were connected to the feed, product, purge and waste streams to control the direction and rate of gas flow during the different stages of the TSA cycle. The opening and closing of these valves were specified using the Cycle Organizer in Aspen Adsorption. The Cycle Organizer was used to define the sequence, duration and operating conditions of the adsorption, depressurisation, regeneration, cooling and repressurisation steps.

3.3. Packed-Bed Model Configuration

The adsorption column was represented using the packed bed model available in Aspen Adsorption. The model describes the temporal and spatial variations in gas composition, pressure, temperature and adsorbed loading along the axial direction of the column. The governing equations of the packed bed model consist of partial differential equations that describe mass, momentum and energy transport within the adsorption column. Aspen uses Discretization which is a method by which complex partial differential equations (PDEs) are converted to system of coupled ordinary differential equations (ODEs) [62].

The first order upwind differencing scheme, denoted as UDS1 in Aspen Adsorption, was selected for discretization of the model. UDS1 is the default discretisation scheme available in Aspen Adsorption and is commonly used for dynamic adsorption simulations because of its numerical stability and relatively low computational requirement. The adsorption bed was discretised into 20 axial nodes.

3.3.1. Momentum Balance

As the process gas flows through the packed bed, a pressure drop develops due to the resistance offered by the adsorbent particles. This pressure drop influences the gas velocity, residence time and overall adsorption performance [61]. Aspen Adsorption provides several momentum balance models for calculating the pressure drop across the packed bed.

One of the available models is the Carman–Kozeny equation, which is applicable only to laminar flow conditions. However, adsorption columns frequently operate over a range of flow regimes, particularly during depressurisation and regeneration, where gas velocities change considerably.

For this reason, the Ergun equation was selected to calculate the pressure drop throughout the adsorption cycle. The Ergun equation combines the Carman-Kozeny equation for laminar flow with the Burke-Plummer equation for turbulent flow. It is one of the most widely used pressure-drop correlations in adsorption modelling and is the default momentum balance model implemented in Aspen Adsorption [61].

$$\frac{\partial P}{\partial z} = -\left[\frac{1.5\times10^{-3}(1-\varepsilon_i)^2}{(2r_p\psi)^2\varepsilon_i^3}\mu v_g + 1.75\times10^{-5}M\rho_g\frac{(1-\varepsilon_i)}{2r_p\psi\varepsilon_i^3}v_g^2\right] \tag{3.15}$$

where

- P is the gas pressure,
- z is the axial coordinate along the adsorption bed,
- ε_i is the inter-particle bed void fraction,
- r_p is the adsorbent particle radius,
- ψ is the particle shape factor or particle sphericity,
- μ is the gas viscosity,
- v_g is the superficial gas velocity,
- ρ_g is the gas density, and
- M is the molecular weight of the gas mixture.

3.3.2. Material Balance

The material balance describes the transport of gaseous species through the adsorption column and the transfer of adsorbate from the gas phase to the solid adsorbent. Aspen Adsorption provides several material balance formulations depending on whether axial dispersion is considered.

In this study, the convection only model was selected. This model assumes the gas phase is transported solely by convection in the axial direction, while axial dispersion is neglected. The gas is also assumed to behave as plug flow and concentration changes occur primarily due to convection and mass transfer between the gas phase and the adsorbent particles. Assumption of neglecting axial dispersion is considered appropriate because the adsorption column has a relatively large length to particle diameter ratio, resulting in convective transport dominating over molecular diffusion.

3.3.3. Kinetic Model

The adsorption equilibrium determines the maximum amount of water that can be adsorbed by the adsorbent, whereas the kinetic model determines the rate at which equilibrium is approached. In a packed adsorption column, several mass transfer resistances exist between the bulk gas phase and the adsorption sites within the adsorbent particle. These include the external film resistance surrounding the particle and the internal diffusion resistance associated with the pore structure of the adsorbent.

Aspen Adsorption provides several kinetic models to represent these mass transfer processes. In this study, the lumped-resistance approach was adopted. The lumped resistance model assumes that the overall mass trasnfer resistance can be represented by a single overall mass transfer coefficient, rather than modelling each individual diffusion mechanism separately [63].

Among the available lumped resistance models, the Linear Driving Force (LDF) model was selected. In the LDF model, the adsorption rate is assumed to be directly proportional to the difference between the instantaneous loading and the equilibrium loading.

$$\rho_s \frac{\partial w_i}{\partial t} = MTC_{g_i} \left(c_i - c_i^*\right) \tag{3.16}$$

$$\frac{\partial w_i}{\partial t} = MTC_{s_i} \left(w_i^* - w_i\right) \tag{3.17}$$

where

- w_i is the instantaneous adsorbed loading,
- w_i^* is the equilibrium loading,
- c_i is the gas-phase concentration,
- c_i^* is the gas concentration in equilibrium with the solid phase,
- MTC_{g_i} is the gas-film mass-transfer coefficient,
- MTC_{s_i} is the solid-phase mass-transfer coefficient, and
- ρ_s is the adsorbent density.

The solid film formulation was selected for water adsorption on zeolite 4A

The LDF model requires specification of the solid phase mass transfer coefficient. A simplified relationship proposed by Naidu and Mathews was used to estimate the LDF coefficient from the effective diffusivity and the adsorbent particle diameter [64]:

$$k_{\mathrm{LDF}} = \frac{15 D_{\mathrm{eff}}}{R_p^2} \tag{3.18}$$

or equivalently,

$$k_{\mathrm{LDF}} = \frac{60 D_{\mathrm{eff}}}{d_p^2} \tag{3.19}$$

where D_{eff} is the effective diffusivity of water within the adsorbent particle, R_p is the particle radius and d_p is the particle diameter.

Gorbach et al. investigated water vapour adsorption on zeolite 4A using experimentally measured equilibrium data and fixed bed breakthrough experiments. The breakthrough curves were described using a modified LDF model in which the kinetic coefficient was expressed as a function of water concentration, temperature and pressure. Therefore, the study does not provide a single constant value of the LDF coefficient applicable to all operating conditions [65].

However, Gorbach et al. reported an effective diffusivity of water on zeolite 4A of approximately

$$D_{\text{eff}} = 6.8 \times 10^{-7}\ \text{m}^2/\text{s},$$

which was adopted in the present work.

For a zeolite 4A pellet diameter of

$$d_p = 2\ \text{mm},$$

the particle radius is

$$R_p = 1 \times 10^{-3}\ \text{m}.$$

Substituting the reported effective diffusivity into Equation 3.18 gives

$$k_{\text{LDF}} = \frac{15(6.8 \times 10^{-7})}{(1 \times 10^{-3})^2} = 10.2\ 1/\text{s}. \tag{3.20}$$

The calculated LDF coefficient of $10.2\ \text{s}^{-1}$ was first implemented in the Aspen Adsorption model. This value produced a steep breakthrough curve, with breakthrough occurring at approximately $28{,}500\ \text{s}$. To assess the sensitivity of the predicted breakthrough behaviour to the mass-transfer coefficient, a second simulation was performed using $k_{\text{LDF}} = 20\ \text{s}^{-1}$. The breakthrough profile remained similarly steep, while the breakthrough time decreased to approximately $19{,}250\ \text{s}$. This indicates that, within the investigated range, the LDF coefficient had a stronger influence on the propagation rate of the adsorption front than on the overall shape of the breakthrough curve.

For the subsequent cyclic TSA simulations, a constant value of $20\ \text{s}^{-1}$ was retained as a conservative modelling choice with respect to breakthrough time, since it predicted earlier water breakthrough and therefore a shorter allowable adsorption period. The adsorption step was subsequently selected as $14{,}000\ \text{s}$, which remains below the predicted breakthrough time. The value of $20\ \text{s}^{-1}$ should therefore be regarded as a kinetic sensitivity based modelling assumption rather than an independently experimentally fitted parameter..

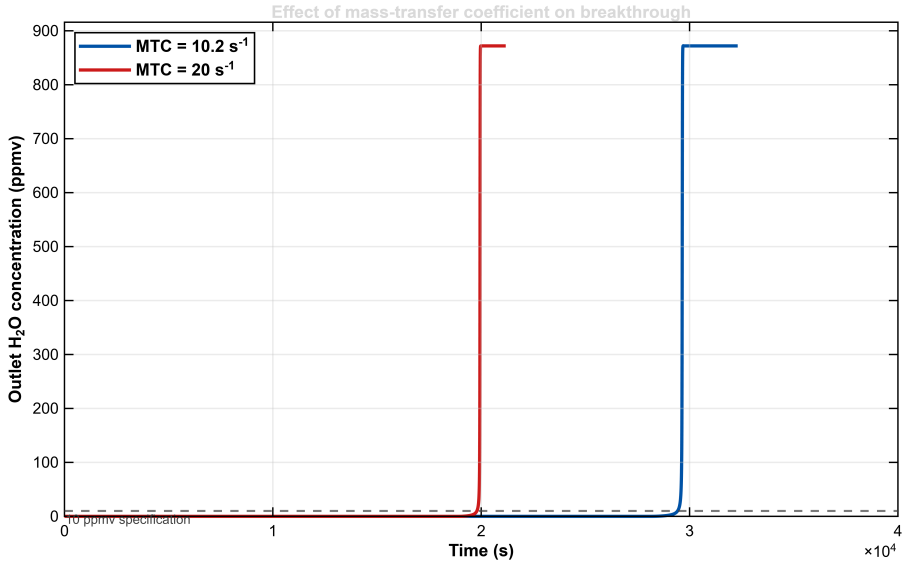

Figure 3.2: Effect of the linear driving force mass-transfer coefficient on the water breakthrough curve. The adsorption bed had an internal diameter of $0.25\ \text{m}$, a packed-bed length of $0.75\ \text{m}$, and a Zeolite 4A pellet diameter of $2\ \text{mm}$. Wet hydrogen containing $872\ \text{ppmv}$ water was supplied at $25\ \text{bar}$, $298.15\ \text{K}$, and $0.0223\ \text{kmol}\,\text{s}^{-1}$. All operating conditions were kept constant while the LDF mass-transfer coefficient was varied between 10.2 and $20\ \text{s}^{-1}$.

3.3.4. Adsorption Isotherm Selection

The adsorption isotherm describes the equilibrium relationship between the water loading on the adsorbent and the water partial pressure in the gas phase at a specified temperature [61, 62]. Selection of an appropriate isotherm model is essential because the predicted equilibrium loading directly affects the calculated adsorption capacity, breakthrough time, regeneration performance and working capacity of the adsorption bed.

An isotherm model can be selected by fitting selected models to experimentally measured adsorption data. In this study, experimental water adsorption data reported by Yu Wang were used for model fitting. The reported data contained equilibrium water loadings for zeolite 4A over a range of water partial pressures and at multiple temperatures [66]

Several studies have represented water adsorption on zeolites using multi site Langmuir model, one of the more recent work of Almas Mardanov reported tripple site langmuir model for water adsorption on zeolite 4A [67, 68]. These models account for the heterogeneous adsorption behaviour of water by assuming that adsorption takes place on more than one type of adsorption site. However, a triple-site Langmuir model was not directly available among the standard isotherm models available in Aspen Adsorption. Therefore, several available models were evaluated using the experimental data.

The candidate isotherm models considered were:

- Toth isotherm;
- Extended Langmuir isotherm;
- Extended Langmuir 2 isotherm;
- Extended Langmuir 3 isotherm;
- Dual-Site Langmuir 1 isotherm;
- Dual-Site Langmuir 2 isotherm.

The parameters of each model were determined by nonlinear regression. The quality of each fit was evaluated using statistical indicators, including the coefficient of determination, root-mean-square error and normalised root-mean-square error. Particular attention was also given to the low-pressure region because hydrogen drying involves the removal of trace quantities of water.

Among the tested models, the Dual-Site Langmuir 2 model provided the best overall representation of the experimental water adsorption data. It reproduced both the pressure dependence and the temperature dependence of the water loading more accurately than the other candidate models. Therefore, the Dual-Site Langmuir 2 model was selected for the Aspen Adsorption simulations.

The Dual-Site Langmuir model assumes that adsorption occurs on two different groups of adsorption sites. The total equilibrium loading is therefore expressed as the sum of the loading on site 1 and site 2:

$$q_i^* = \frac{q_{s,1,i}(T) b_{1,i}(T) p_i}{1 + \sum_k b_{1,k}(T) p_k} + \frac{q_{s,2,i}(T) b_{2,i}(T) p_i}{1 + \sum_k b_{2,k}(T) p_k} \tag{3.21}$$

where q_i^* is the equilibrium loading of component i, p_i is its partial pressure, $q_{s,1,i}$ and $q_{s,2,i}$ are the saturation capacities of the two adsorption sites, and $b_{1,i}$ and $b_{2,i}$ are the corresponding affinity parameters. The summation over k accounts for competition between all adsorbing components.

Since water was the only adsorbing component. Therefore, the summation contained only the contribution of water, while hydrogen adsorption was neglected.

In the Dual-Site Langmuir 2 formulation implemented in Aspen Adsorption, the saturation capacities of the two adsorption sites are expressed as linear functions of temperature:

$$q_{s,1,i}(T) = IP_{1,i} + IP_{2,i} T \tag{3.22}$$

$$q_{s,2,i}(T) = IP_{5,i} + IP_{6,i}T \tag{3.23}$$

The corresponding affinity parameters are expressed as:

$$b_{1,i}(T) = IP_{3,i} \exp\left(\frac{IP_{4,i}}{T}\right) \tag{3.24}$$

$$b_{2,i}(T) = IP_{7,i} \exp\left(\frac{IP_{8,i}}{T}\right) \tag{3.25}$$

where $IP_{1,i}$ to $IP_{8,i}$ are the fitted isotherm parameters for component i, and T is the absolute temperature.

Substitution of the temperature-dependent saturation capacities and affinity parameters into the Dual-Site Langmuir equation gives the Aspen Dual-Site Langmuir 2 formulation:

$$W_i = \frac{(IP_{1,i} + IP_{2,i}T)\, IP_{3,i} \exp\left(\frac{IP_{4,i}}{T}\right) p_i}{1 + \sum_k IP_{3,k} \exp\left(\frac{IP_{4,k}}{T}\right) p_k} + \frac{(IP_{5,i} + IP_{6,i}T)\, IP_{7,i} \exp\left(\frac{IP_{8,i}}{T}\right) p_i}{1 + \sum_k IP_{7,k} \exp\left(\frac{IP_{8,k}}{T}\right) p_k} \tag{3.26}$$

In Equation 3.26, W_i is the equilibrium adsorbed loading of component i, p_i is its partial pressure, and T is the absolute temperature. The first term represents adsorption on the first group of sites, while the second term represents adsorption on the second group of sites.

An important advantage of the Dual-Site Langmuir 2 formulation is that both the saturation capacities and the adsorption affinities can vary with temperature. The experimentally measured water loading on zeolite 4A decreased as the temperature increased. The temperature dependent capacity terms in Equations 3.22 and 3.23 allowed this behaviour to be represented directly, while the exponential affinity terms described the reduction in adsorption strength with changing temperature. The model therefore provided sufficient flexibility to represent the strongly nonlinear and temperature-dependent adsorption of water on zeolite 4A over the investigated range of partial pressures. The fitted Dual-Site Langmuir 2 parameters used in Aspen Adsorption are presented in Table 3.1.

Table 3.1: Fitted Dual-Site Langmuir 2 parameters for water adsorption on zeolite 4A.

Parameter	Fitted value
IP_1	2.1575×10^{-3}
IP_2	-1.1867×10^{-6}
IP_3	2.7393×10^{4}
IP_4	1.05295×10^{3}
IP_5	1.6673×10^{-2}
IP_6	-1.5422×10^{-5}
IP_7	5.1976×10^{-6}
IP_8	6.5895×10^{3}

The parameters were fitted using pressure in bar, temperature in kelvin and adsorbed loading in $\mathrm{kmol\,kg^{-1}}$. The fitted parameters were entered directly into Aspen Adsorption using the same units.

The selected Dual-Site Langmuir 2 model produced a coefficient of determination of $R^2 = 0.9939$ and a root mean square error of $3.84 \times 10^{-4}\ \mathrm{kmol\,kg^{-1}}$. The corresponding normalised root-mean-square error was 0.0276. These results indicated that the model provided a satisfactory representation of the measured equilibrium data over the investigated temperature and pressure range.

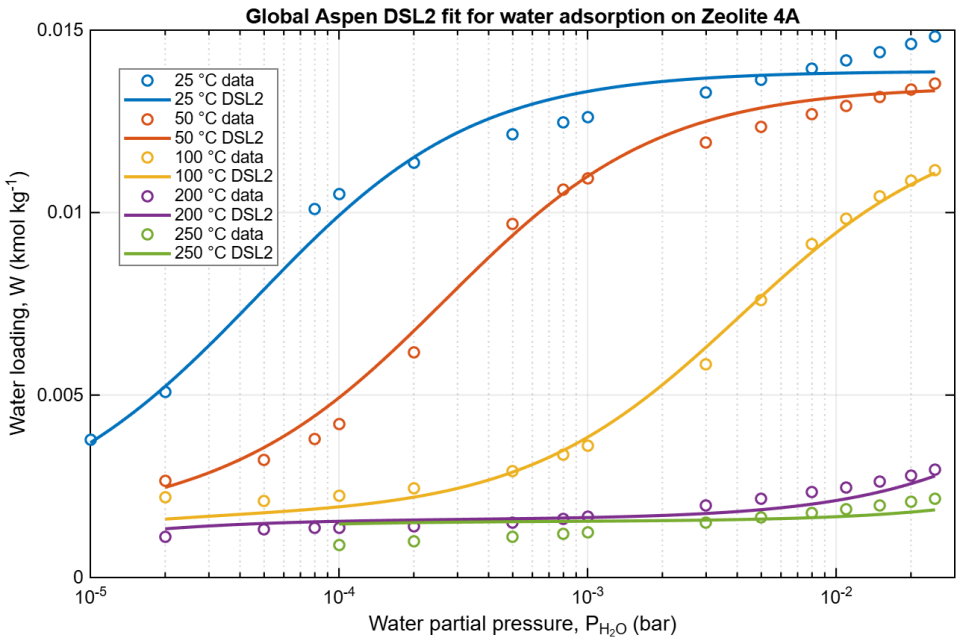

Figure 3.3: Global Dual-Site Langmuir 2 fit for water adsorption on zeolite 4A at different temperatures.

Aspen Adsorption requires adsorption isotherm parameters to be specified for every component included in the simulation. Therefore, isotherm parameters were also assigned to hydrogen. However, hydrogen was treated as a non-adsorbing carrier gas because the adsorption affinity of hydrogen for zeolite 4A is negligible compared with that of water under the operating conditions considered in this study. To represent this behaviour, the adsorption parameters for hydrogen were assigned sufficiently small values so that the predicted equilibrium hydrogen loading was effectively zero over the entire pressure and temperature range investigated.

Table 3.2: Dual-Site Langmuir 2 parameters assigned to hydrogen.

Parameter	Value
IP_1	1.0×10^{-12}
IP_2	0
IP_3	1.0×10^{-12}
IP_4	0
IP_5	1.0×10^{-12}
IP_6	0
IP_7	1.0×10^{-12}
IP_8	0

3.3.5. Energy Balance

The energy balance governs the variation of gas and solid temperatures within the adsorption bed throughout the temperature swing adsorption cycle. Unlike pressure swing adsorption, the regeneration of the adsorbent in a TSA process is achieved by increasing the bed temperature. An accurate prediction of the temperature distribution is essential because temperature directly influences the adsorption equilibrium, adsorption kinetics and working capacity of the adsorbent.

Aspen Adsorption provides several energy balance formulations, including isothermal and non-isothermal models. In this study, the *Non-isothermal with gas and solid conduction* option was selected. The adsorption of water on zeolite 4A is an exothermic process, resulting in the release of heat during adsorption. Conversely, desorption during regeneration requires the supply of thermal energy and is therefore

is an endothermic process. Assuming isothermal operation would neglect these temperature variations and could therefore underpredict the temperature rise during adsorption and the temperature required for regeneration. The predicted adsorption capacity, breakthrough behaviour and working capacity of the adsorbent may also deviate from the actual process behaviour. For these reasons a non-isothermal energy balance was considered more appropriate for this study.

The non-isothermal model required specification of the heat capacities, thermal conductivities, heat-transfer coefficients and heat of adsorption. The values used in the Aspen Adsorption model were either obtained from literature, calculated using established correlations or estimated from the selected operating conditions.

Heat capacity of the solid adsorbent The thermal inertia of the zeolite 4A adsorbent was included in the non-isothermal energy balance through the solid-phase specific heat capacity, $C_{p,s}$. The temperature dependence of the zeolite heat capacity was estimated using the correlation reported in [69],

$$C_{p,s}(T) = 850 + 0.94(T - 273) \qquad \left[\mathrm{J\,kg^{-1}K^{-1}}\right]. \tag{3.27}$$

Since the bed temperature varies during the TSA cycle, a representative temperature of approximately $373\ \mathrm{K}$ was used to obtain a constant heat capacity for the Aspen Adsorption model. This gives

$$C_{p,s}(373) = 850 + 0.94(373 - 273) = 944\ \mathrm{J\,kg^{-1}K^{-1}}. \tag{3.28}$$

Accordingly, a constant value of approximately

$$C_{p,s} \simeq 9.0 \times 10^{-4}\ \mathrm{MJ\,kg^{-1}K^{-1}} \tag{3.29}$$

was specified in Aspen Adsorption. The solid heat capacity therefore accounts for the sensible energy required to heat and cool the zeolite bed during the TSA cycle and was included in the non-isothermal simulations.

Heat capacity of the adsorbed phase Water was the only component assumed to undergo significant adsorption on zeolite 4A. Therefore, the heat capacity of the adsorbed phase was represented using the specific heat capacity of water [69]:

$$C_{p,\mathrm{a,H_2O}} = 4120\ \mathrm{J\,kg^{-1}\,K^{-1}}. \tag{3.30}$$

Hydrogen was treated as a non-adsorbing carrier gas. Hence, its contribution to the heat capacity of the adsorbed phase was set to zero:

$$C_{p,\mathrm{a,H_2}} = 0. \tag{3.31}$$

Heat of adsorption The heat of adsorption of water on zeolite 4A was determined from the temperature-dependent equilibrium adsorption data using the Clausius–Clapeyron relation:

$$\left(\frac{\partial \ln P}{\partial(1/T)}\right)_q = -\frac{\Delta H_{\mathrm{ads}}}{R}, \tag{3.32}$$

where P is the equilibrium water partial pressure at a constant adsorbed loading, T is the absolute temperature, R is the universal gas constant and ΔH_{ads} is the heat of adsorption.

For a selected constant loading, a plot of $\ln P$ against $1/T$ was constructed. The heat of adsorption was calculated from the slope of the resulting line:

$$\Delta H_{\mathrm{ads}} = -R \left[\frac{\partial \ln P}{\partial (1/T)} \right]_q . \tag{3.33}$$

The calculated magnitude of the heat of adsorption was approximately:

$$|\Delta H_{\mathrm{ads}}| = 59 \ \mathrm{MJ\,kmol^{-1}}, \tag{3.34}$$

equivalent to $59 \ \mathrm{kJ\,mol^{-1}}$. A constant heat of adsorption of $59 \ \mathrm{MJ\,kmol^{-1}}$ was therefore used in the Aspen Adsorption model.

Heat transfer coefficient The heat-transfer coefficient between the gas phase and the adsorbent particles was estimated using the Nusselt-number correlation [70]:

$$Nu_p = 2 + 1.1 Re_p^{0.6} Pr^{1/3}, \tag{3.35}$$

where Nu_p is the particle Nusselt number, Re_p is the particle Reynolds number and Pr is the Prandtl number. The Wakao correlation was developed for particle-to-fluid heat transfer in packed beds and was correlated for particle Reynolds numbers of approximately $15 \leq Re_p \leq 8500$ [70]. For the present bed, the adsorption condition gives $Re_p \approx 206$, which lies within this range. During the low-flow regeneration stages, however, the estimated Reynolds number decreases to approximately $Re_p \approx 1.6 - 7$, which is below the published correlation range. The application of the Wakao correlation during these low-flow stages therefore represents an extrapolation and the resulting gas–solid heat transfer coefficient should be regarded as a screening level estimate. Experimental validation or comparison with a correlation applicable to lower Reynolds numbers is recommended for further refinement of the model.

The corresponding gas to particle heat transfer coefficient was calculated as:

$$h_{gs} = \frac{Nu_p k_g}{d_p}, \tag{3.36}$$

where h_{gs} is the gas to solid heat transfer coefficient, k_g is the thermal conductivity of the gas and d_p is the adsorbent-particle diameter.

The particle Reynolds number was calculated using:

$$Re_p = \frac{\rho_g u_g d_p}{\mu_g}, \tag{3.37}$$

and the Prandtl number was calculated from:

$$Pr = \frac{C_{p,g} \mu_g}{k_g}, \tag{3.38}$$

where ρ_g, u_g, μ_g and $C_{p,g}$ are the gas density, superficial gas velocity, dynamic viscosity and gas-phase specific heat capacity, respectively.

The coefficient was evaluated at the heating-stage temperatures of $100\,^{\circ}\mathrm{C}$, $150\,^{\circ}\mathrm{C}$ and $175\,^{\circ}\mathrm{C}$. An average value of:

$$h_{gs} = 540 \ \mathrm{W\,m^{-2}\,K^{-1}} \tag{3.39}$$

was selected and applied as a constant value throughout the TSA simulation.

Gas thermal conductivity The gas phase consisted predominantly of hydrogen, while the water concentration was only $872\ \mathrm{ppmv}$. The contribution of water vapour to the overall gas thermal conductivity was therefore assumed to be negligible. A constant hydrogen thermal conductivity of:

$$k_g = 0.20\ \mathrm{W\,m^{-1}\,K^{-1}} \tag{3.40}$$

was used in the model [71].

Gas-to-wall heat transfer coefficient Heat transfer between the gas phase and the internal surface of the adsorber wall was represented using a constant gas-to-wall heat transfer coefficient. A simplified Nusselt-number relation for fully developed laminar internal flow was used [72]:

$$Nu_D = 3.66. \tag{3.41}$$

The gas-to-wall heat-transfer coefficient was then calculated as:

$$h_{gw} = \frac{Nu_D k_g}{D}, \tag{3.42}$$

where D is the internal diameter of the adsorption vessel.

The coefficient was evaluated at the heating-stage temperatures of $100\,^\circ\mathrm{C}$, $150\,^\circ\mathrm{C}$ and $175\,^\circ\mathrm{C}$. The resulting average value was:

$$h_{gw} = 3.5\ \mathrm{W\,m^{-2}\,K^{-1}}. \tag{3.43}$$

This value was specified as a constant gas-to-wall heat-transfer coefficient in Aspen Adsorption.

Heat transfer to the surroundings Heat transfer from the external vessel wall to the surroundings was represented by natural convection under ambient conditions. Reported convective heat-transfer coefficients under buoyancy driven natural convection conditions are typically in the range of approximately $5-25\ \mathrm{W\,m^{-2}\,K^{-1}}$ [73]. A constant value within this range was therefore adopted for the present model:

$$h_{\mathrm{amb}} = 7\ \mathrm{W\,m^{-2}\,K^{-1}}. \tag{3.44}$$

This value represents weak natural convection from the external vessel surface to the surrounding air. In the unit system used in Aspen Adsorption, this is equivalent to:

$$h_{\mathrm{amb}} = 7 \times 10^{-6}\ \mathrm{MW\,m^{-2}\,K^{-1}}. \tag{3.45}$$

Adsorber-wall properties The adsorption vessel was assumed to be manufactured from stainless steel. The wall specific heat capacity was specified as [74]:

$$C_{p,w} = 500\ \mathrm{J\,kg^{-1}\,K^{-1}}, \tag{3.46}$$

while the wall thermal conductivity was specified as [74]:

$$k_w = 16\ \mathrm{W\,m^{-1}\,K^{-1}}. \tag{3.47}$$

In the Aspen unit system, the wall thermal conductivity was entered as:

$$k_w = 1.6 \times 10^{-5}\ \mathrm{MW\,m^{-1}\,K^{-1}}. \tag{3.48}$$

The energy-balance options implemented in Aspen Adsorption are summarised in Table 3.3.

Table 3.3: Energy-balance assumptions used in Aspen Adsorption.

Parameter	Selected option
Energy balance formulation	Non-isothermal with gas and solid conduction
Heat capacity of adsorbed phase	Constant
Heat of adsorption	Constant
Heat-transfer coefficient	Constant
Gas thermal conductivity	Constant
Heat transfer to surroundings	Rigorous
Gas-wall heat-transfer coefficient	Constant
Solid heat capacity	Constant

3.3.6. Bed Specifications and Feed-Flow-Rate Selection

The geometry of the adsorption column was selected using a bed height-to-diameter ratio of approximately $3:1$. The internal diameter and packed-bed height were therefore specified as:

$$D = 0.25 \text{ m} \tag{3.49}$$

and

$$L = 0.75 \text{ m}. \tag{3.50}$$

The resulting height to diameter ratio was:

$$\frac{L}{D} = \frac{0.75}{0.25} = 3. \tag{3.51}$$

The cross-sectional area of the cylindrical adsorption bed was calculated as:

$$A = \frac{\pi D^2}{4}, \tag{3.52}$$

which gives:

$$A = \frac{\pi(0.25)^2}{4} = 4.91 \times 10^{-2} \text{ m}^2. \tag{3.53}$$

According to *Unit Operations of Chemical Engineering*, the superficial gas velocity in a packed adsorption bed should typically be maintained within the approximate range of 0.15 to 0.45 m s^{-1}. Operation within this range helps limit the pressure drop across the packed bed while maintaining sufficient gas throughput [75].

The upper value of the recommended range,

$$u_s = 0.45 \text{ m s}^{-1}, \tag{3.54}$$

was initially used to determine the maximum feed flow rate. The superficial velocity is defined as:

$$u_s = \frac{\dot{V}}{A}, \tag{3.55}$$

where u_s is the superficial gas velocity, $\dot{V}$ is the volumetric gas-flow rate evaluated at the bed inlet conditions, and A is the cross-sectional area of the bed.

Rearranging Equation 3.55, the inlet volumetric flow rate was calculated as:

$$\dot{V} = u_s A. \tag{3.56}$$

Substituting the selected superficial velocity and bed area gives:

$$\dot{V} = (0.45)\left(4.91 \times 10^{-2}\right) = 2.21 \times 10^{-2}\ \mathrm{m^3\,s^{-1}}. \tag{3.57}$$

The corresponding molar flow rate was estimated using the ideal-gas relationship:

$$P\dot{V} = \dot{n}RT, \tag{3.58}$$

which can be rearranged as:

$$\dot{n} = \frac{P\dot{V}}{RT}. \tag{3.59}$$

Using a feed pressure of $25\ \mathrm{bar}$, equivalent to $2.5 \times 10^6\ \mathrm{Pa}$, and a feed temperature of $298.15\ \mathrm{K}$, the molar flow rate was calculated as:

$$\begin{aligned} \dot{n} &= \frac{\left(2.5 \times 10^6\right)\left(2.21 \times 10^{-2}\right)}{(8.314)(298.15)} \\ &= 22.3\ \mathrm{mol\,s^{-1}} \\ &= 0.0223\ \mathrm{kmol\,s^{-1}}. \end{aligned} \tag{3.60}$$

A feed flow rate of $0.0223\ \mathrm{kmol\,s^{-1}}$ was therefore selected for the Aspen Adsorption simulations. This flow rate corresponds to an inlet superficial velocity of approximately $0.45\ \mathrm{m\,s^{-1}}$ at $25\ \mathrm{bar}$ and $298.15\ \mathrm{K}$.

Although the Peng–Robinson equation of state was used within Aspen Adsorption to calculate the thermodynamic properties of the gas, the ideal-gas relation was considered adequate for the preliminary feed flow rate estimate. The selected flow rate was subsequently entered directly into the rigorous Aspen model.

3.4. Cycle Construction

Following the breakthrough simulation, a cyclic TSA process was constructed in Aspen Adsorption. The cycle consisted of five sequential steps: adsorption, blowdown, heating (thermal regeneration), cooling and repressurisation. Each step was implemented using the Aspen Cycle Organizer, which controlled the opening and closing of the feed, product, purge and waste valves according to the operating sequence. The purpose of each step is described below.

Adsorption

During the adsorption step, wet hydrogen containing $872\ \mathrm{ppmv}$ water vapour entered the bottom of the adsorption column through the feed valve at a flow rate of $0.0223\ \mathrm{kmol\,s^{-1}}$. Simultaneously, the product valve was kept open, allowing the dried hydrogen product to leave the top of the bed.

As the gas flowed through the packed bed, water molecules were adsorbed by the zeolite 4A due to its high affinity towards polar molecules, while hydrogen passed through the bed unadsorbed. The adsorption step was operated for $14\,000\ \mathrm{s}$, corresponding to approximately 73% of the predicted breakthrough time, thereby preventing water breakthrough in the product stream.

Blowdown

At the end of the adsorption step, both the feed and product valves were closed and the waste valve was opened. The bed pressure was reduced from $25\ \mathrm{bar}$ to $1\ \mathrm{bar}$. The depressurisation was divided into two steps to improve the numerical stability and convergence of the simulation.

Reducing the pressure decreased the equilibrium adsorption capacity of the adsorbent, resulting in partial desorption of the adsorbed water. The blowdown step therefore recovered part of the adsorbed moisture while simultaneously preparing the bed for thermal regeneration.

Heating (Thermal Regeneration)

Following blowdown, regeneration of the adsorbent was carried out using a hot hydrogen purge. A fraction of the purified hydrogen product was recycled and introduced counter currently to the original adsorption flow direction while the waste valve remained open.

Heating the bed increased the temperature of both the gas and solid phases, thereby reducing the equilibrium adsorption capacity of zeolite 4A for water and promoting desorption of the retained moisture. The desorbed water was continuously removed from the bed through the waste stream.

To improve numerical stability and avoid large thermal gradients, the regeneration temperature was increased progressively through three temperature levels implemented in four heating stages. Two consecutive stages were operated at $100\,^{\circ}\mathrm{C}$, followed by stages at $150\,^{\circ}\mathrm{C}$ and $175\,^{\circ}\mathrm{C}$..

Cooling

Following thermal regeneration, the adsorption bed was cooled to the adsorption temperature using a flow of dry hydrogen introduced through the purge connection. Cooling reduced the bed temperature to approximately $25\,^{\circ}\mathrm{C}$, restoring favourable adsorption conditions for the subsequent cycle. During this step, the remaining desorbed water was also flushed from the bed before repressurisation.

Repressurisation

In the final step of the cycle, the bed pressure was increased from $1\ \mathrm{bar}$ back to the adsorption pressure of $25\ \mathrm{bar}$ using purified hydrogen. This restored the initial operating conditions of the adsorption column and prepared the bed for the next adsorption cycle.

Table 3.4 gives a summary of the main cycle steps used in the TSA simulation. It presents the duration, pressure range, valve coefficient C_v, and flow rate for each step, including adsorption, blowdown, heating, cooling, and repressurisation.

The cycle step durations were not prescribed from a single analytical correlation, but were determined from the dynamic response of the Aspen Adsorption model. A physical end criterion was defined for each step and the corresponding duration was refined iteratively until the required pressure, temperature or regeneration condition was reached with stable numerical convergence.

The adsorption duration was determined independently from the breakthrough simulation. For the selected kinetic model, water breakthrough occurred at approximately $19{,}250\ \mathrm{s}$. An adsorption time of $14{,}000\ \mathrm{s}$ was therefore selected, corresponding to approximately 72.7% of the predicted breakthrough time and providing a safety margin of $5{,}250\ \mathrm{s}$.

The blowdown duration was selected to reduce the bed pressure progressively from 25 to $1\ \mathrm{bar}$. The pressure reduction was divided into two stages, $25 \rightarrow 6\ \mathrm{bar}$ and $6 \rightarrow 1\ \mathrm{bar}$, to avoid an abrupt pressure transient and to improve numerical stability. The resulting durations were $1{,}500$ and $2{,}000\ \mathrm{s}$, respectively.

The regeneration sequence was similarly developed by progressively increasing the purge temperature and flow rate. The initial $100^{\circ}\mathrm{C}$ stages were used to provide a gradual transition from blowdown to thermal regeneration, after which the purge temperature was increased to $150^{\circ}\mathrm{C}$ and finally $175^{\circ}\mathrm{C}$. The final $175^{\circ}\mathrm{C}$ stage was maintained for the longest period because the thermal front had to propagate through the complete bed and reduce the residual adsorbed water loading before cooling.

Cooling was continued until the bed temperature returned approximately to the adsorption temperature of $25^{\circ}\mathrm{C}$. Repressurisation was then continued until the bed pressure returned from 1 to $25\ \mathrm{bar}$. The final durations reported in Table 3.4 therefore represent the converged cycle settings obtained from the sequential dynamic simulations rather than independently prescribed literature values.

Table 3.4: Operating conditions for the TSA cycle steps.

Cycle step	Time (s)	Pressure (bar)	C_v ($\mathrm{kmol\,s^{-1}\,bar^{-1}}$)	flowrate ($\mathrm{kmol\,s^{-1}}$)
Adsorption	14 000	25	–	2.23×10^{-2}
Blowdown 1	1 500	$25 \rightarrow 6$	2.0×10^{-6}	–
Blowdown 2	2 000	$6 \rightarrow 1$	1.5×10^{-6}	–
Heating at $100\,^{\circ}\mathrm{C}$, Stage 1	1 000	$1.25 \rightarrow 1$	3.0×10^{-7}	–
Heating at $100\,^{\circ}\mathrm{C}$, Stage 2	3 000	$1.25 \rightarrow 1$	–	2.0×10^{-4} (1%)
Heating at $150\,^{\circ}\mathrm{C}$	3 000	$1.25 \rightarrow 1$	–	1.0×10^{-3} (5%)
Heating at $175\,^{\circ}\mathrm{C}$	8 000	$1.25 \rightarrow 1$	–	1.0×10^{-3} (5%)
Cooling	3 000	$1.25 \rightarrow 1$	–	2.0×10^{-3} (10%)
Repressurisation	2 000	$1 \rightarrow 25$	2.5×10^{-6}	–

Note: The percentages indicate the purge gas flow rate relative to the adsorption feed flow rate.

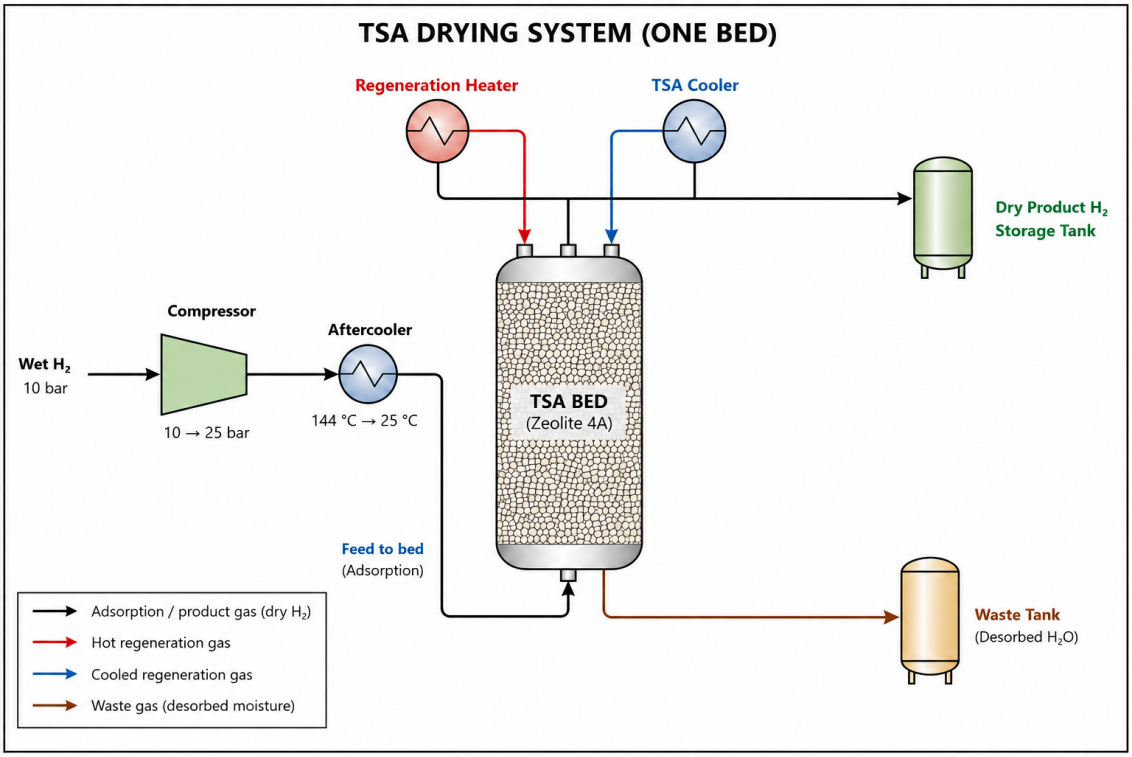

Figure 3.4: Simplified process-flow diagram of the TSA hydrogen-drying system. A single adsorption bed is shown for clarity. Wet hydrogen is compressed, aftercooled and dried in the TSA bed, while a fraction of the dry product hydrogen is used for regeneration and cooling in counter-current operation. The complete continuous process consists of three identical TSA beds operated in a staggered cycle.

3.4.1. Process equipment sizing

The main process equipment was sized using the operating conditions obtained from the Aspen Adsorption simulations together with the corresponding mass and energy requirements of the TSA process. For each unit, the process requirement was first calculated and a design capacity was subsequently selected. The resulting equipment-sizing basis is summarised in Table 3.5.

Table 3.5: Sizing basis and selected capacities of the main TSA process equipment.

Equipment	Sizing basis	Calculated requirement	Selected/design value
Hydrogen compressor	Compression of $0.0223\ \mathrm{kmol\,s^{-1}}$ H_2 from 10 to $25\ \mathrm{bar}$	$76.9\ \mathrm{kW}$ shaft power; $80.9\ \mathrm{kW}$ electrical power	$90\ \mathrm{kW}$ motor
Compressor aftercooler	Cooling compressed hydrogen from approximately $144\,^{\circ}\mathrm{C}$ to $25\,^{\circ}\mathrm{C}$	$76.9\ \mathrm{kW}$ cooling duty	$85\ \mathrm{kW}$ design duty
TSA adsorption vessels	Bed dimensions and adsorbent inventory required by the adsorption model	$D = 0.25\ \mathrm{m}$, $L = 0.75\ \mathrm{m}$, approximately $28\ \mathrm{kg}$ zeolite per bed	Three identical TSA vessels
Regeneration heater	Maximum thermal requirement during hot-gas regeneration	$4.365\ \mathrm{kW}$ maximum thermal duty	$5.238\ \mathrm{kW}$ design thermal duty; approximately $6\ \mathrm{kW}$ electrical capacity
TSA cooling-gas cooler	Sensible heat removed from the regenerated bed during the $3000\ \mathrm{s}$ cooling step	$1.78\ \mathrm{kW}$ cooling duty	$2.5\ \mathrm{kW}$ selected capacity
Waste receiver	Gas and desorbed-water discharge during blowdown and regeneration	Sized from the maximum waste-stream hold-up	Dedicated waste receiver

Hydrogen compressor

The compressor was sized from the hydrogen feed flow rate and the required pressure increase from 10 to $25\ \mathrm{bar}$. The calculated isentropic compression requirement corresponded to a shaft power of $76.9\ \mathrm{kW}$. Accounting for a motor efficiency of 0.95, the electrical requirement was $80.9\ \mathrm{kW}$. A nominal motor capacity of approximately $90\ \mathrm{kW}$ was therefore selected.

Compressor aftercooler

Compression increased the hydrogen temperature to approximately $144\,^{\circ}\mathrm{C}$. The aftercooler was sized to reduce the gas temperature to the adsorption inlet temperature of $25\,^{\circ}\mathrm{C}$. The corresponding calculated cooling duty was $76.9\ \mathrm{kW}$. After application of the design allowance, an aftercooler capacity of approximately $85\ \mathrm{kW}$ was selected.

TSA adsorption vessels

The adsorption vessels were sized directly from the packed-bed dimensions used in the Aspen Adsorption model. Each bed has an internal diameter of $0.25\ \mathrm{m}$ and a packed length of $0.75\ \mathrm{m}$, containing approximately $28\ \mathrm{kg}$ of zeolite 4A. Three identical beds were used to permit staggered operation and continuous hydrogen drying.

Regeneration heater

The regeneration heater was sized from the maximum thermal requirement of the hot hydrogen purge stream. The maximum calculated heater duty was

$$\dot{Q}_{\mathrm{heater,max}} = 4.365\ \mathrm{kW}. \tag{3.61}$$

A 20% design allowance was applied:

$$\dot{Q}_{\mathrm{heater,design}} = 1.20(4.365) = 5.238\ \mathrm{kW}. \tag{3.62}$$

For a heater efficiency of 90%, the corresponding electrical requirement is approximately $5.82\ \mathrm{kW}$. A nominal $6\ \mathrm{kW}$ heater was therefore selected.

TSA cooling-gas cooler

The cooling-gas cooler was sized from the sensible heat that must be removed during the cooling stage. The calculated heat-removal requirement was approximately $5.34\ \mathrm{MJ}$ per bed cycle. For a cooling duration of $3000\ \mathrm{s}$,

$$\dot{Q}_{\mathrm{cool}} = \frac{5.34 \times 10^6}{3000} = 1.78\ \mathrm{kW}. \tag{3.63}$$

After allowing additional design capacity, a cooler capacity of $2.5\ \mathrm{kW}$ was selected.

3.5. Techno-Economic Analysis

A techno-economic analysis (TEA) was performed for the selected three-bed TSA process to estimate the incremental capital investment, annual operating expenditure, and levelized cost associated with drying the hydrogen stream. The economic analysis was carried out using OpenPyTEA, an open source Python based techno-economic analysis framework [76]. Process conditions, equipment duties, and operating requirements obtained from the Aspen Adsorption model were used as the technical basis for equipment sizing and costing. All purchased equipment cost correlations used in the deterministic economic analysis were selected from the built-in OpenPyTEA equipment-cost database [76]. The corresponding correlation types, sizing variables and validity limits were retained as implemented within OpenPyTEA

Upstream hydrogen production by electrolysis was excluded from the economic boundary; therefore, the calculated levelized cost represents only the additional cost of the hydrogen-drying section.

System Boundary

The TEA boundary was defined around the equipment required to compress, cool, dry, regenerate, and return the hydrogen stream to the dry-product header. Wet hydrogen enters the drying section at 10 bar and is compressed to 25 bar, aftercooled, and then treated in the three-bed TSA system. The dry product is sent to the common dry hydrogen product header.

During regeneration, a slipstream of dry product hydrogen is taken from this header, heated, and introduced counter-currently into the bed being regenerated. During the subsequent cooling step, dry hydrogen is passed through the cooling-gas cooler before entering the regenerated bed. Gas discharged during blowdown, regeneration, and cooling is directed to a waste receiver.

The final equipment boundary consequently consists of the hydrogen compressor, compressor aftercooler, three TSA pressure vessels, automated switching valves, regeneration gas heater, TSA cooling-gas cooler, and waste receiver. The process boundary is shown in Figure 3.4.

Equipment Sizing and OpenPyTEA Cost Correlations

Equipment purchase costs were estimated using only correlations contained in the OpenPyTEA equipment-cost database. The cost data underlying these correlations originate from published equipment-cost correlations implemented within OpenPyTEA, including the Towler correlations for compressors and pressure vessels and the Nexant correlation for heat exchangers [76]. The resulting purchased-equipment costs were therefore correlation-based estimates rather than vendor quotations. External equipment-cost correlations were not introduced into the deterministic base case. The correlation selected for each item was chosen according to the physical equipment type, the sizing variable required by the correlation, and its stated validity range. The final basis is summarized in Table 3.6.

Table 3.6: Equipment sizing and OpenPyTEA Cost correlation/source used for the corrected TSA techno-economic analysis.

Equipment	Sizing input	OpenPyTEA representation	Costing basis
Hydrogen compressor	93 kW cost floor; required shaft power 76.9 kW	Reciprocating compressor	Towler correlation; lower validity limit used because the required shaft power lies below the 93 kW correlation minimum
Compressor aftercooler	76.9 kW process duty	Heat exchanger	Nexant duty-based heat-exchanger correlation
TSA vessels (3)	120 kg shell-mass cost floor per vessel	Vertical 304SS pressure vessel	Towler pressure-vessel correlation; actual calculated shell mass is approximately 23.7 kg per vessel
Regeneration-gas heater	5.238 kW design thermal duty	Heat exchanger	Nexant duty-based heat-exchanger correlation used as an indirect small gas-heater cost proxy
TSA cooling-gas cooler	2.5 kW thermal duty	Heat exchanger	Nexant duty-based heat-exchanger correlation
Waste receiver	Shell mass	Horizontal carbon-steel pressure vessel	Towler pressure-vessel correlation

The compressor requires 57.7 kW of ideal-fluid compression power. With an isentropic efficiency of 75%, the required shaft power is 76.9 kW, while the electrical input becomes 80.9 kW after applying a motor efficiency of 95%. These quantities serve different purposes in the TEA: shaft/driver power is the relevant equipment-costing quantity, whereas electrical input determines compressor electricity consumption.

Several compressor correlations available in OpenPyTEA were screened. The reciprocating-compressor correlation was retained because it is the most appropriate built-in representation for the relatively small hydrogen flow and the required pressure increase. Its stated driver-power range begins at 93 kW. Because the calculated shaft power of 76.9 kW is below this lower limit, direct extrapolation was avoided and 93 kW was used only as the CAPEX costing floor. The physical compressor duty was not increased: 76.9 kW remains the required shaft power and 80.9 kW remains the electrical demand used for OPEX.

The compressor aftercooler and TSA cooling-gas cooler were represented using the OpenPyTEA Nexant heat-exchanger correlation. Thermal duties were converted from kW to MMBTU h^{-1} using

$$\dot{Q}_{\mathrm{MMBTU/h}} = 0.00341214\,\dot{Q}_{\mathrm{kW}}. \tag{3.64}$$

The three TSA columns were represented as vertical 304 stainless-steel pressure vessels. For the selected bed dimensions and 5 mm wall thickness, the calculated cylindrical shell mass is approximately 23.7 kg per vessel. This lies below the 120 kg lower validity limit of the selected OpenPyTEA vessel correlation. Therefore, 120 kg per vessel was used as a conservative costing floor, while the physical vessel mass remained 23.7 kg.

For a cylindrical shell,

$$m_{\mathrm{shell}} = \frac{\pi}{4}\left(D_{\mathrm{o}}^2 - D_{\mathrm{i}}^2\right) L \rho_{\mathrm{s}}, \tag{3.65}$$

where D_{o} and D_{i} are the outer and inner diameters, L is the cylindrical shell length, and ρ_{s} is the vessel material density.

The regeneration-gas heater required separate treatment because the dedicated small-heater options in the OpenPyTEA database were not suitable for the present service. The maximum calculated thermal duty delivered to the regeneration gas was 4.365 kW. Applying a 20% design margin gives

$$\dot{Q}_{\mathrm{heater,design}} = 1.20(4.365) = 5.238\ \mathrm{kW}. \tag{3.66}$$

The final CAPEX model therefore represented the regeneration gas heater using the builtin Nexant duty based heat exchanger correlation as a screening level proxy for a small indirect gas heater. This choice remains entirely within the OpenPyTEA cost database and avoids application of the cylindrical-furnace correlation, which produced an implausibly high cost for the very small heater duty. The process equipment is nevertheless referred to as a regeneration gas heater throughout the thesis. The limitation of using a generic duty based heat exchanger as the economic proxy is stated explicitly when interpreting the TEA.

The waste receiver was retained as a preliminary low pressure carbonsteel vessel for gas released during blowdown and regeneration. Its calculated shell mass was supplied to the horizontal pressure-vessel correlation. Detailed sizing and correlation calculations are provided in Appendix B.

OpenPyTEA Installation and Fixed-Capital Method

The purchased-equipment costs obtained from the selected correlations were converted to direct installed costs using the standard installation factors implemented in OpenPyTEA. No external installation multipliers were substituted in the deterministic base case. In general, OpenPyTEA calculates direct cost as

$$C_{\mathrm{direct}} = C_{\mathrm{p}}\left[(1+f_{\mathrm{piping}})f_{\mathrm{material}} + f_{\mathrm{erection}} + f_{\mathrm{electrical}} + f_{\mathrm{instrumentation}} + f_{\mathrm{civil}} + f_{\mathrm{structural}} + f_{\mathrm{lagging}}\right], \tag{3.67}$$

where C_{p} is purchased equipment cost and the f terms are the installation and material factors assigned by OpenPyTEA [76]. For the default fluid process carbonsteel equipment, these factors correspond to a direct to purchased cost ratio of approximately 3.20. For the 304SS TSA vessels the material factor increases the corresponding ratio to approximately 3.74. These default factors were retained to keep the capital-cost methodology internally consistent with OpenPyTEA rather than tuning the installation basis to obtain a particular LCOP value [76].

The Netherlands location factor was subsequently applied to obtain the ISBL capital basis. For the integrated drying-section boundary, the OSBL allowance was set to 20% of ISBL. Design and engineering and contingency were then calculated using 30% and 10%, respectively, consistent with the selected OpenPyTEA project configuration. In simplified form,

$$C_{\mathrm{OSBL}} = f_{\mathrm{OSBL}} C_{\mathrm{ISBL}}, \qquad f_{\mathrm{OSBL}} = 0.20, \tag{3.68}$$

and

$$C_{\mathrm{FCI}} = \left(C_{\mathrm{ISBL}} + C_{\mathrm{OSBL}}\right)\left(1 + f_{\mathrm{D\&E}} + f_{\mathrm{cont}}\right), \tag{3.69}$$

with $f_{\mathrm{D\&E}} = 0.30$ and $f_{\mathrm{cont}} = 0.10$. The 20% OSBL assumption reflects the treatment of the TSA unit as an incremental process section integrated within a larger hydrogen-production facility rather than as a fully independent greenfield plant. The effect of the OSBL assumption was included explicitly in the uncertainty analysis.

Treatment of Switching Valves and Adsorbent

The three-bed TSA configuration requires four principal automated switching valves per bed. The valves are part of the physical process boundary, but no suitable automated process-valve cost correlation was available in the OpenPyTEA equipment database. Consequently, the twelve switching

valves were not entered as separate purchased-equipment items. Their piping, instrumentation, electrical, and installation requirements are partly captured through the general OpenPyTEA installation factors. The omission of a separate valve purchase cost remains a limitation of the screening-level TEA.

Likewise, no applicable built-in OpenPyTEA cost correlation was available for zeolite 4A. To preserve an OpenPyTEA-only equipment-costing basis, no external adsorbent supplier price was added to the deterministic CAPEX. The initial zeolite charge and replacement cost are therefore not represented explicitly and should be considered when interpreting the reported drying cost.

Energy Consumption and Variable OPEX

The variable operating expenditure included electricity for the hydrogen compressor and the regeneration-gas heater. Compressor electricity was calculated from

$$E_{\mathrm{comp,d}} = P_{\mathrm{comp,el}} \times 24, \tag{3.70}$$

where $P_{\mathrm{comp,el}} = 80.9$ kW.

The staged heating calculation gives a sensible-energy requirement of

$$Q_{\mathrm{regen,H_2}} = 47.13\ \mathrm{MJ\,bed^{-1}\,cycle^{-1}}. \tag{3.71}$$

This is the sensible energy supplied to the regeneration hydrogen and was used for heater OPEX. It was not added to the separately calculated 25.18 MJ bed-regeneration thermal requirement, because doing so would double count two different descriptions of the regeneration-energy demand.

For a heater efficiency $\eta_{\mathrm{h}} = 0.90$, the electrical energy per bed cycle is

$$E_{\mathrm{heat,cycle}} = \frac{Q_{\mathrm{regen,H_2}}}{\eta_{\mathrm{h}}\, 3.6}, \tag{3.72}$$

where the factor 3.6 converts MJ to kWh. For cycle time t_{cycle} and N_{bed} beds,

$$E_{\mathrm{heat,d}} = E_{\mathrm{heat,cycle}} \left(\frac{86400}{t_{\mathrm{cycle}}} \right) N_{\mathrm{bed}}, \tag{3.73}$$

and

$$E_{\mathrm{el,d}} = E_{\mathrm{comp,d}} + E_{\mathrm{heat,d}}. \tag{3.74}$$

The base-case active cycle time was 37,500 s and the three-bed arrangement was used in the energy calculation. The later 4,500 s pressurised standby period increases the complete bed-repeat interval to 42,000 s. Retaining 37,500 s for the economic energy conversion is therefore slightly conservative because it predicts a greater number of regeneration events per day.

The thermal duties of the compressor aftercooler and TSA cooling-gas cooler were used for equipment sizing but were not treated as direct electrical loads. No additional cooler electricity was included because a specific cooling-system power requirement was not defined.

Economic Assumptions and Fixed OPEX

A target cost year of 2024 was used. OpenPyTEA escalated the underlying correlations from their original cost years using the indices available within the software. The plant location was specified as the Netherlands and costs were reported in euros. A 2024 annual-average exchange basis of $1\ \mathrm{EUR} = 1.0824\ \mathrm{USD}$ was used for conversion of dollar-based correlations.

The base-case assumptions are summarized in Table 3.7.

Table 3.7: Base-case assumptions used in the corrected OpenPyTEA analysis.

Parameter	Value	Unit
Target cost year	2024	–
Project lifetime	20	years
Discount/interest rate	9	%
Plant utilization	100	%
Electricity price	0.246	EUR kWh^{-1}
Operator hourly rate	35.21	EUR h^{-1}
Allocated operators	1	FTE
OSBL factor	20	% of ISBL
Design and engineering	30	%
Contingency	10	%
Working-capital factor	15	% of FCI
Annual dry H_2 production	1.325388×10^6	kg year^{-1}
Heater efficiency	90	%
Number of TSA beds	3	–
TSA active cycle time	37500	s

The annual dry-hydrogen production was obtained from the continuous three-bed net production rate of 151.3 kg h^{-1}:

$$m_{\mathrm{H_2,annual}} = 151.3(24)(365) = 1.325388 \times 10^6 \ \mathrm{kg\,year^{-1}}. \tag{3.75}$$

The OpenPyTEA default automatic staffing method is intended for a stand-alone process plant and, for the present flowsheet, would assign 13 operators. That assumption was considered inconsistent with the incremental system boundary, where the TSA unit is integrated with an existing hydrogen-production facility. The corrected base case therefore assigns one full-time-equivalent operator to represent the incremental operational workload associated with the drying unit. This does not imply that the hydrogen facility is unattended; it means that only the labour attributable to the TSA section is charged to the incremental drying cost.

For the same reason, fixed-OPEX categories that are not considered incremental to the drying section were set to zero: laboratory charges, additional land rent, general plant overhead, patents and royalties, distribution and selling, and research and development. Labour, supervision, salary overhead, maintenance, taxes and insurance, environmental charges, operating supplies, and working-capital interest were retained. The operator requirement was also examined separately as a deterministic sensitivity because the distinction between integrated and stand-alone staffing is a structural scenario rather than a random process fluctuation.

Levelized Cost of Hydrogen Drying

The economic performance of the TSA unit was represented by the levelized cost calculated using the OpenPyTEA discounted cash-flow model [76]. Because the upstream hydrogen-production cost is outside the system boundary, this quantity is interpreted as the incremental cost of converting wet hydrogen into specification-grade dry hydrogen.

In general,

$$LCOP = \frac{\displaystyle\sum_{t=0}^{N} \frac{C_{\mathrm{CAPEX},t} + C_{\mathrm{OPEX},t}}{(1+i)^t}}{\displaystyle\sum_{t=0}^{N} \frac{m_{\mathrm{H_2},t}}{(1+i)^t}}, \tag{3.76}$$

where $C_{\mathrm{CAPEX},t}$ and $C_{\mathrm{OPEX},t}$ are the capital and operating costs in year t, $m_{\mathrm{H_2},t}$ is the corresponding dry hydrogen production, i is the discount rate, and N is the project lifetime. The LCOP is therefore

reported in EUR per kg of dry hydrogen. The complete OpenPyTEA cash-flow treatment, including construction-period expenditure, production ramp, working capital, and discounting, is documented in Appendix B.

Sensitivity and Monte Carlo Uncertainty Analysis

The deterministic TEA represents one combination of technical and economic assumptions. A combined Monte Carlo uncertainty analysis was therefore used to quantify the spread in LCOP, and Spearman rank correlation coefficients were used to identify which uncertain inputs exert the strongest influence.

The uncertain variables were divided into economic uncertainties and technical process uncertainties. Published statistical distributions were not available for every parameter specific to the present TSA design. Consequently, the ranges were treated as transparent screening-level uncertainty assumptions rather than as experimentally measured population statistics. Bounded truncated-normal distributions were used to prevent physically or economically unreasonable samples. The final uncertainty inputs are summarized in Table 3.8.

Table 3.8: Input uncertainties used for the corrected combined technical–economic Monte Carlo analysis.

Parameter	Base/location	Assumed σ	Lower bound	Upper bound
CAPEX multiplier	1.00	0.20	0.70	1.50
OSBL factor	0.20	0.05	0.10	0.30
Interest rate	0.09	0.02	0.05	0.13
Project lifetime [yr]	20	5	10	30
Electricity price [EUR kWh^{-1}]	0.246	0.04	0.15	0.35
Operator rate [EUR h^{-1}]	35.21	7.0	20.0	50.0
Compressor electrical power [kW]	80.9	8.09	64.72	97.08
Regeneration energy [MJ $cycle^{-1}$]	47.13	7.07	32.99	61.27
TSA cycle time [s]	37500	3750	30000	45000
Dry-H_2 production rate [kg h^{-1}]	151.3	7.565	136.17	166.43

The CAPEX multiplier represents uncertainty in the screening-level equipment and installed-capital estimate. The OSBL factor independently captures uncertainty in the extent to which off-site infrastructure is shared with the surrounding hydrogen facility. Interest rate, project lifetime, electricity price, and operator rate represent economic scenario uncertainty. The technical variables were assigned bounded engineering uncertainties around the Aspen-based base case because plant-specific experimental standard deviations were not available. For the technical parameters, standard deviations of approximately 10% were assumed for compressor electrical power and TSA cycle time, 15% for regeneration energy, and 5% for the dry-hydrogen production rate.

Each Monte Carlo realization propagated the sampled technical variables through the physical cost drivers rather than applying a random multiplier directly to the final LCOP. In particular, sampled compressor power altered annual compressor electricity, sampled regeneration energy and cycle time altered annual heater electricity, and sampled dry-hydrogen production changed the annual product denominator. Sampled CAPEX, OSBL, interest rate, lifetime, electricity price, and labour rate were propagated through the corresponding capital, OPEX, and discounted cash-flow calculations.

A total of 10,000 Monte Carlo realizations were evaluated. The central 95% uncertainty interval was defined from the 2.5th and 97.5th percentiles of the resulting LCOP distribution; it is therefore reported as an uncertainty interval rather than a statistical confidence interval.

The relative influence of each uncertain input was quantified using the Spearman rank correlation coefficient,

$$\rho_{\mathrm{s}} = \mathrm{corr}\left[\mathrm{rank}(X), \mathrm{rank}(LCOP)\right], \tag{3.77}$$

where X denotes an uncertain input. Positive values indicate that increasing the parameter tends to increase LCOP, while negative values indicate an inverse relationship. The magnitude of $|\rho_s|$ provides a measure of the relative strength of the monotonic relationship. The resulting Monte Carlo distribution and sensitivity ranking are presented in the Results section.

4

Results and Discussion

4.1. Selection of TSA over PSA/VPSA

Pressure-based regeneration was investigated before the final TSA cycle was selected. Depressurisation from $25\ \mathrm{bar}$ to $1\ \mathrm{bar}$ produced only a limited reduction in the adsorbed-water loading. This result is consistent with the strong affinity of Zeolite 4A for water: lowering the pressure reduces the water partial pressure and promotes desorption, but under the investigated conditions the pressure reduction alone did not restore sufficient working capacity for repeated deep drying.

Vacuum-assisted regeneration improved desorption. The deepest successfully evaluated vacuum case, at approximately $0.007\ \mathrm{bar}$, produced a lower residual loading than conventional pressure-swing regeneration. However, a stable multi-cycle VPSA solution could not be obtained because the Aspen Adsorption simulation failed during the following cycle. This numerical failure should not be interpreted as proof that VPSA is physically infeasible. It shows that further optimisation of the pressure transitions, valve coefficients, step durations and solver settings would be required before a reliable cyclic comparison with TSA could be made.

In contrast, the TSA configuration could be simulated through repeated cycles to cyclic steady state while maintaining the required product-water specification. TSA was therefore selected for the final process analysis because it was the regeneration strategy for which both effective adsorbent regeneration and stable cyclic operation were demonstrated under the selected model conditions.

4.2. Breakthrough Behaviour and Selection of Adsorption Time

A breakthrough simulation was performed to determine the maximum duration for which the adsorption bed could produce hydrogen satisfying the required water specification. The variation of the outlet water concentration with time is presented in Figure 4.1. Breakthrough was defined as the point at which the outlet water concentration exceeded the product specification of $5\ \mathrm{ppm}$.

At the beginning of the adsorption step, the outlet water concentration remained close to zero because water was strongly adsorbed by the initially regenerated Zeolite 4A. The concentration remained below the required $5\ \mathrm{ppmv}$ limit for an extended period, demonstrating that the bed was capable of producing hydrogen that satisfied the specified moisture requirement.

The first breakthrough was observed at approximately

$$t_{\mathrm{breakthrough}} = 19\,250\ \mathrm{s},$$

when the outlet water concentration increased beyond $5\ \mathrm{ppm}$. After breakthrough, the outlet concentration increased rapidly and eventually approached $872\ \mathrm{ppm}$, corresponding to the water concentration in the wet hydrogen feed. This steep increase indicates that the mass-transfer zone had reached the outlet of the bed and that the available adsorption capacity was nearly exhausted.

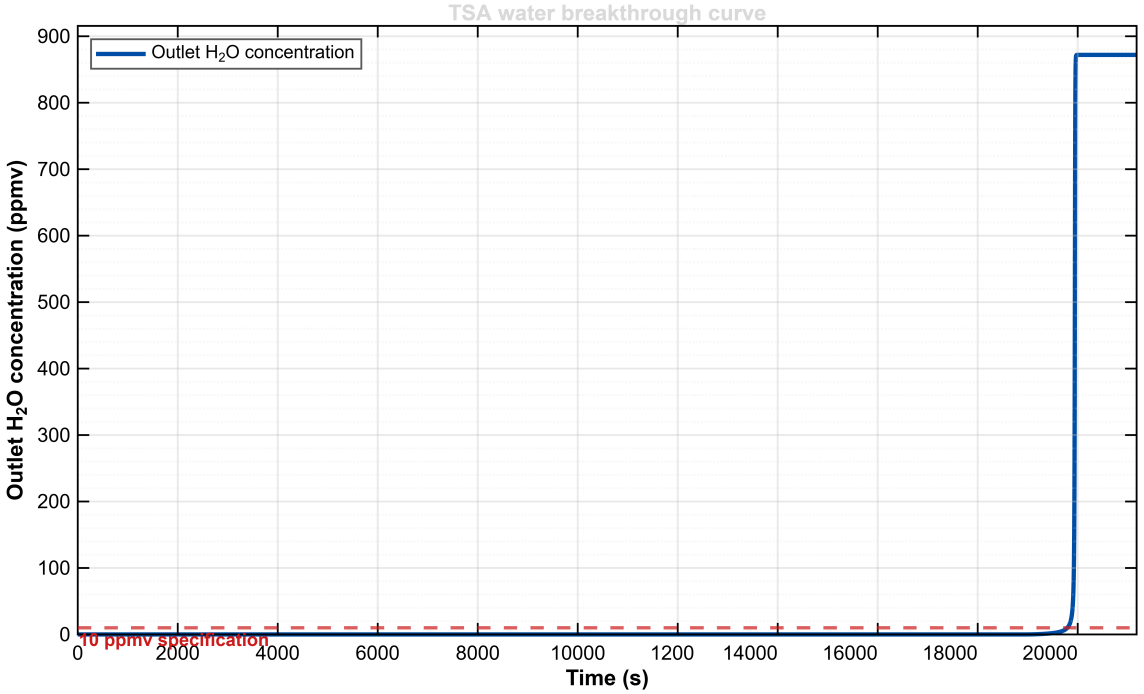

Figure 4.1: Simulated water breakthrough curve for hydrogen drying using Zeolite 4A. The dashed horizontal line represents the product water specification of $5\ \mathrm{ppmv}$.

Although breakthrough occurred at approximately $19\,250\ \mathrm{s}$, an adsorption time of

$$t_{\mathrm{ads}} = 14\,000\ \mathrm{s}$$

was selected for the TSA cycle. The selected adsorption time therefore provides a safety margin of

$$\Delta t_{\mathrm{safety}} = t_{\mathrm{breakthrough}} - t_{\mathrm{ads}} = 19\,250 - 14\,000 = 5\,250\ \mathrm{s}.$$

The adsorption step was therefore terminated at approximately 72.7% of the breakthrough time obtained from the simulated breakthrough curve.

$$\frac{t_{\mathrm{ads}}}{t_{\mathrm{breakthrough}}} \times 100 = \frac{14\,000}{19\,250} \times 100 = 72.7\%.$$

Stopping the adsorption step before the onset of breakthrough prevents the mass-transfer front from reaching the product end of the bed. The selected duration also provides operational flexibility for possible cycle-to-cycle variations in bed loading, regeneration efficiency, temperature and flow conditions. Therefore, $14\,000\ \mathrm{s}$ was used as the adsorption duration in the subsequent TSA cycle simulations to ensure that the produced hydrogen remained below the $5\ \mathrm{ppm}$ water specification.

The selected adsorption time is therefore intentionally shorter than the simulated breakthrough time. Extending the adsorption step would increase bed utilisation and the amount of hydrogen processed per adsorption event, but it would also move the mass-transfer zone closer to the product outlet and reduce the margin against water breakthrough. The $14\,000\ \mathrm{s}$ adsorption period was therefore retained as a compromise between bed utilisation and protection of the product-water specification.

4.3. Solid Water Loading During the TSA Cycle

The variation of the adsorbed water loading at different axial positions of the bed during one complete TSA cycle is presented in Figure 4.2. Nodes 1, 5, 10 and 15 represent progressively higher positions along the adsorption bed, with Node 1 located close to the wet-hydrogen feed inlet.

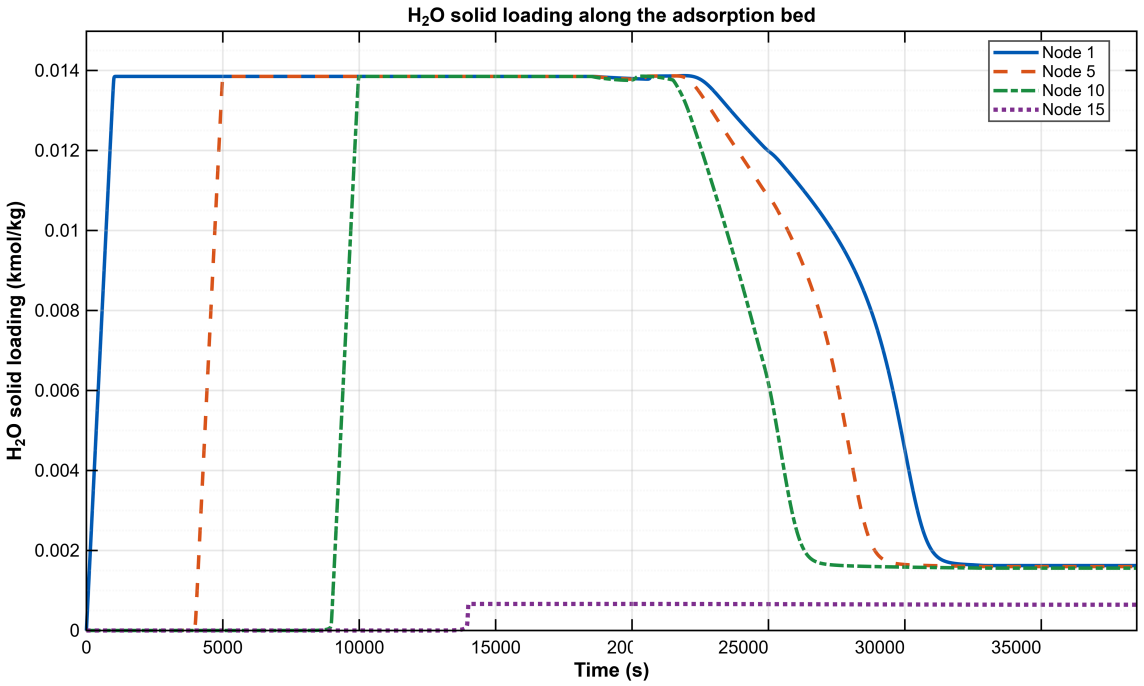

Figure 4.2: Evolution of the water loading on Zeolite 4A at axial nodes 1, 5, 10, and 15 during one complete TSA cycle.

During the adsorption step, extending from 0 to $14\,000$ s, the water loading increased first at the feed end of the bed. Node 1 reached a loading of approximately

$$q_{\mathrm{H_2O}} \approx 0.0138 \ \mathrm{kmol\,kg^{-1}}$$

within the initial part of the adsorption step. Node 5 reached a similar loading after approximately $5\,000$ s, whereas Node 10 became saturated after approximately $10\,000$ s. The delayed increase in loading at successive axial positions represents the movement of the water mass-transfer zone through the bed.

At the end of the selected adsorption period, Nodes 1, 5 and 10 were close to their equilibrium loading. In contrast, the loading at Node 15 remained considerably lower, at approximately

$$q_{\mathrm{H_2O,Node\,15}} \approx 6 \times 10^{-4} \ \mathrm{kmol\,kg^{-1}}.$$

This result indicates that the water adsorption front had not yet reached the upper section of the bed after $14\,000$ s. Therefore, a relatively dry section of adsorbent remained between the mass-transfer zone and the product outlet. This unused section acted as a protective mass-transfer zone and prevented the outlet water concentration from exceeding the 5 ppmv product specification.

During the blowdown period between $14\,000$ and $17\,500$ s, only a small change in solid loading was observed. Reducing the pressure from 25 bar to 1 bar was therefore insufficient to remove a significant fraction of the strongly adsorbed water. This behaviour is expected because water has a high affinity for Zeolite 4A, and pressure reduction alone provides only limited regeneration under the investigated conditions.

A significant reduction in solid loading occurred during the subsequent heating period. The decrease was first observed at Node 10, followed by Nodes 5 and 1. This sequence resulted from the counter-current introduction of heated dry hydrogen from the product end of the bed. The regeneration front moved in the direction opposite to the adsorption front.

The temperature increase reduced the equilibrium water capacity of Zeolite 4A and promoted the transfer of adsorbed water from the solid phase to the gas phase. The desorbed water was subsequently

carried out of the bed through the waste outlet by the regeneration gas. Node 10 reached its regenerated loading earlier than Nodes 5 and 1 because it was located closer to the hot-purge inlet.

At the end of the heating and cooling periods, the loading at Nodes 1, 5 and 10 decreased to approximately

$$q_{\mathrm{end,regen}} \approx 1.8 \times 10^{-3}\ \mathrm{kmol\,kg^{-1}}.$$

The approximate local working capacity of the adsorbent in the substantially loaded regions of the bed can therefore be estimated as

$$\Delta q = q_{\mathrm{end,ads}} - q_{\mathrm{end,regen}},$$

which gives

$$\Delta q \approx 0.0138 - 0.0018 = 0.012\ \mathrm{kmol\,kg^{-1}}.$$

This corresponds to an approximate regeneration of

$$\eta_{\mathrm{regen}} = \frac{q_{\mathrm{end,ads}} - q_{\mathrm{end,regen}}}{q_{\mathrm{end,ads}}} \times 100,$$

resulting in

$$\eta_{\mathrm{regen}} \approx \frac{0.0138 - 0.0018}{0.0138} \times 100 \approx 87\%.$$

The loading remained nearly constant during the final cooling and repressurisation steps, indicating that no significant readsorption occurred when dry hydrogen was used for cooling and repressurisation. Although the adsorbent was not completely regenerated to a zero water loading, the residual loading was substantially lower than the loading reached during adsorption. The resulting working capacity was therefore considered sufficient for operation in the subsequent TSA cycle.

The comparison between blowdown and heating also explains the selection of thermal regeneration. Blowdown alone caused only a small reduction in water loading, whereas the staged heating sequence reduced the loading from about 0.0138 to $0.0018\ \mathrm{kmol\,kg^{-1}}$ in the substantially loaded region of the bed. The large improvement during heating shows that temperature increase was the main driving force for restoring the working capacity of Zeolite 4A under the investigated conditions.

4.4. Temperature Behaviour During the TSA Cycle

The gas and solid temperature profiles at selected axial positions during one complete TSA cycle are presented in Figure 4.3 and Figure 4.4, respectively. Nodes 1, 10 and 20 represent the feed end, middle section and product end of the adsorption bed, respectively. During regeneration, the heated dry hydrogen was introduced counter-currently from the product end of the bed. Node 20 was therefore the first position exposed to the hot regeneration gas.

The simulated gas and solid temperatures were found to be almost identical throughout the cycle. This indicates that the heat-transfer resistance between the hydrogen gas and the Zeolite 4A particles was small under the investigated conditions.

During the adsorption step, from 0 to $14\,000\ \mathrm{s}$, the temperature remained close to the feed temperature of approximately $25^{\circ}\mathrm{C}$ throughout the bed. The absence of a large temperature increase during this period indicates that the heat generated by water adsorption did not produce substantial long-term heat accumulation under the simulated operating conditions.

Following adsorption, the bed was depressurised from $25\ \mathrm{bar}$ to approximately $1\ \mathrm{bar}$. A reduction in temperature was observed during this blowdown step. The strongest cooling occurred at Node 20, where

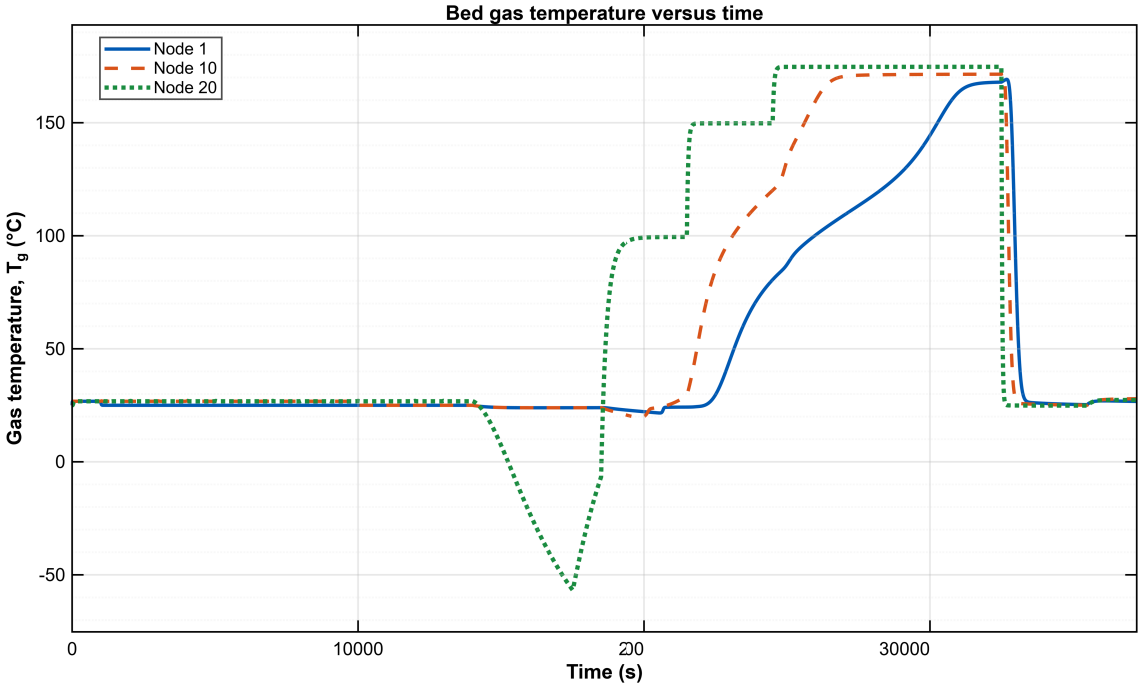

Figure 4.3: Gas-temperature profiles at selected axial positions during one complete TSA cycle. The solid-phase temperature followed an almost identical profile and is therefore not shown separately.

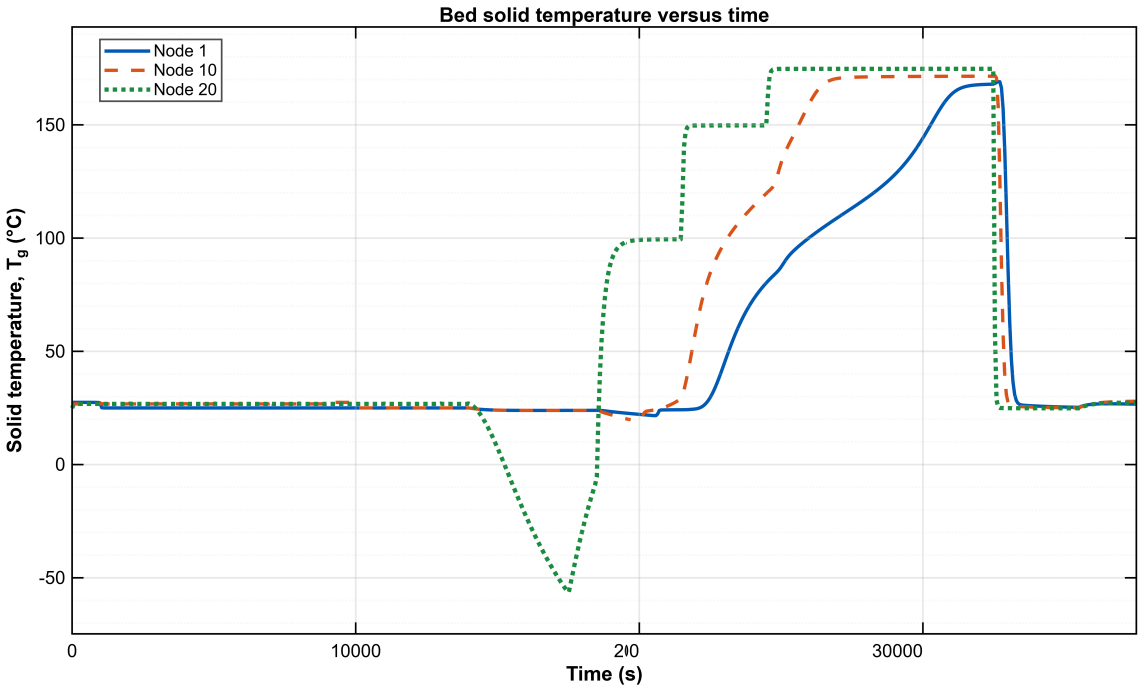

Figure 4.4: Solid-temperature profiles at selected axial positions during one complete TSA cycle.

the temperature decreased to approximately $-55^{\circ}\mathrm{C}$. In comparison, the temperatures at Nodes 1 and 10 decreased only slightly below the initial bed temperature.

The temperature decrease during blowdown cannot be explained by the Joule–Thomson effect alone. The Joule–Thomson calculation predicted a temperature change of only approximately $0.54\,\mathrm{K}$, whereas an ideal adiabatic expansion calculation predicted a much lower final temperature of approximately $-154.4\,^{\circ}\mathrm{C}$. The minimum temperature obtained from the non-isothermal Aspen simulation was about $-55\,^{\circ}\mathrm{C}$, which lies between these two limiting predictions.

For the 25 to $1\ \mathrm{bar}$ blowdown, the Peng–Robinson-based Joule–Thomson estimate gave

$$\mu_{\mathrm{JT}} \approx 0.0227\ \mathrm{K\,bar^{-1}},$$

corresponding to a final temperature of approximately

$$T_{2,\mathrm{JT}} = 297.46\ \mathrm{K} \approx 24.3\,^{\circ}\mathrm{C}.$$

At the opposite limiting case, an ideal reversible adiabatic (isentropic) expansion predicted

$$T_{2,\mathrm{ad}} = 118.79\ \mathrm{K} \approx -154.4\,^{\circ}\mathrm{C}.$$

The minimum temperature obtained from the non-isothermal Aspen simulation was approximately

$$T_{\mathrm{Aspen}} \approx 218.15\ \mathrm{K} \approx -55\,^{\circ}\mathrm{C}.$$

Thus,

$$T_{2,\mathrm{ad}} < T_{\mathrm{Aspen}} < T_{2,\mathrm{JT}}, \tag{4.1}$$

showing that the simulated blowdown cannot be represented as either purely isenthalpic throttling or ideal isentropic expansion. The complete Joule–Thomson and ideal-expansion calculations are provided in Appendix A.9.

The heating stage started after completion of the blowdown step. Since the hot regeneration gas entered from the product end, Node 20 responded first. Its temperature increased rapidly to approximately $100^{\circ}\mathrm{C}$, followed by successive increases to $150^{\circ}\mathrm{C}$ and $175^{\circ}\mathrm{C}$ in accordance with the staged regeneration temperature.

The middle section of the bed, represented by Node 10, displayed a delayed temperature increase relative to Node 20. Node 1, located near the wet-hydrogen feed inlet responded last and required a longer period to approach the final regeneration temperature. This behaviour demonstrates the movement of the thermal front from the hot-purge inlet towards the opposite end of the bed.

The axial temperature delay is important for regeneration because water desorption depends strongly on the local adsorbent temperature. The solid loading results showed that the reduction in water loading occurred first in the region closer to the hot-purge inlet and subsequently progressed towards the feed end. The movement of the desorption front therefore corresponded closely to the propagation of the thermal front through the bed.

By the end of the final heating stage, the temperatures at Nodes 10 and 20 were close to 170–$175^{\circ}\mathrm{C}$, while Node 1 approached a similar temperature after a longer delay. The result indicates that the selected heating duration was sufficient for the thermal front to reach the feed end of the bed.

During the cooling step, dry hydrogen at approximately $25^{\circ}\mathrm{C}$ was introduced from the product end. Node 20 cooled first, followed by Nodes 10 and 1. The temperature decreased rapidly throughout the bed and approached approximately $25^{\circ}\mathrm{C}$ before repressurisation.

A small temperature increase was observed during the final repressurisation step. This increase can be attributed to compression of the gas entering the bed. Nevertheless, the final bed temperature remained close to the required adsorption temperature, indicating that the cooling period was sufficient to prepare the bed for the subsequent adsorption cycle.

Overall, the temperature profiles demonstrate the counter-current propagation of the heating and cooling fronts through the adsorption bed. The close agreement between the gas and solid temperatures also indicates effective gas–solid heat transfer. The staged heating procedure successfully increased the entire bed temperature towards $175°\mathrm{C}$, reducing the equilibrium water capacity of Zeolite 4A and promoting regeneration.

The very low temperature predicted during blowdown is important for the practical interpretation of the TSA cycle. The Aspen minimum of approximately $-55\,°\mathrm{C}$ lies between the small Joule–Thomson temperature change and the much lower ideal isentropic limit. It should therefore be interpreted as the result of the coupled transient pressure change, gas expansion and heat exchange with the adsorbent and vessel wall rather than as a pure Joule–Thomson or ideal isentropic effect. If such low local temperatures occur in practice, they may affect condensation or freezing behaviour and the performance of valves and seals. The magnitude of this transient is therefore an important point for experimental validation.

4.5. Pressure Behaviour During Blowdown and Repressurisation

The pressure profiles at selected axial positions during one complete TSA cycle are presented in Figure 4.5. The upper panel shows the complete pressure variation, whereas the lower panel enlarges the low-pressure region to show the pressure behaviour during regeneration more clearly.

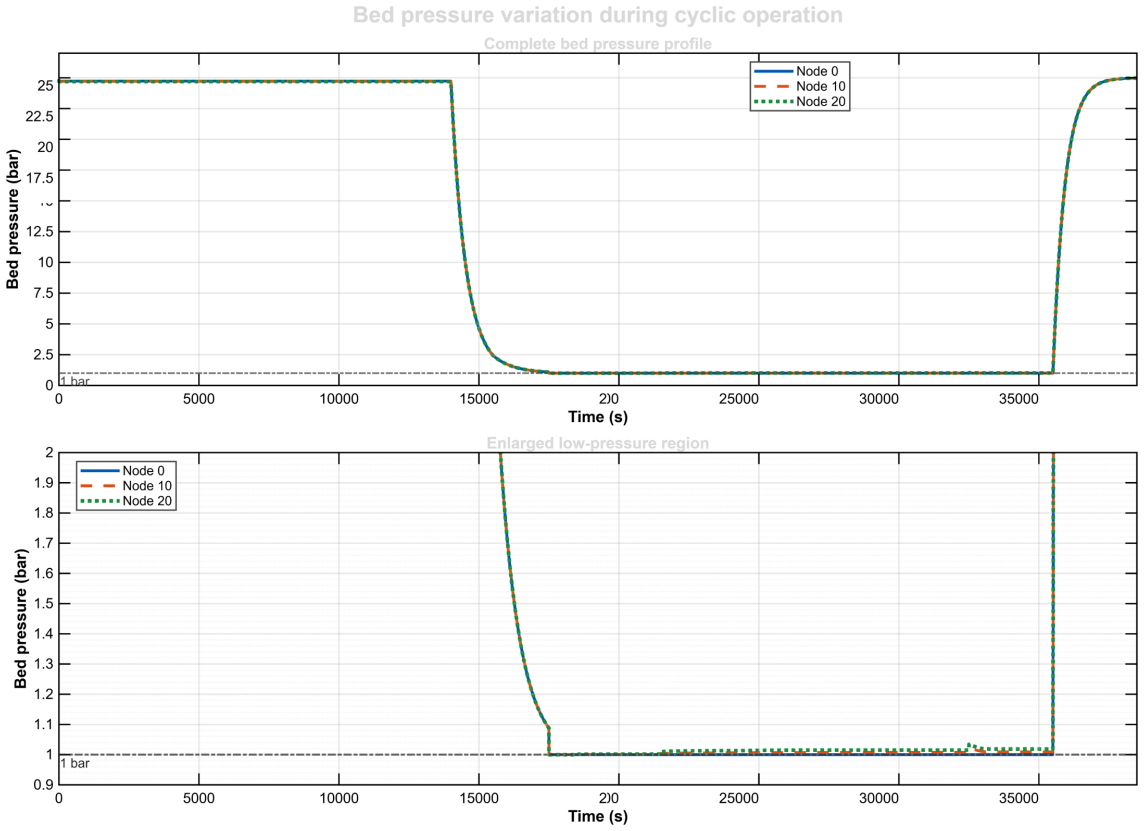

Figure 4.5: Bed-pressure profiles at selected axial positions during one complete TSA cycle. The lower panel shows an enlarged view of the low-pressure regeneration period.

During the adsorption step, from 0 to $14\,000\ \mathrm{s}$, the bed pressure remained approximately constant at

$$P_{\mathrm{ads}} \approx 25\ \mathrm{bar}.$$

The pressure profiles at Nodes 0, 10 and 20 almost completely overlapped. Therefore, the axial pressure drop across the $0.75\ \mathrm{m}$ bed was small relative to the total operating pressure. This indicates that the selected feed flow rate, bed dimensions and particle properties did not produce a significant pressure gradient during adsorption.

At the end of adsorption, the feed and product connections were closed and the bed was depressurised through the waste outlet. During the blowdown step, the pressure decreased from approximately $25\ \mathrm{bar}$ to $1\ \mathrm{bar}$. The pressure initially decreased rapidly and subsequently approached the final blowdown pressure more gradually. A pressure of approximately $1\ \mathrm{bar}$ was reached at about

$$t \approx 17\,500\ \mathrm{s},$$

corresponding to a blowdown duration of approximately $3\,500\ \mathrm{s}$.

The strong pressure reduction during blowdown coincided with the temperature decrease discussed in Section 4.4. In particular, the rapid expansion of hydrogen produced substantial local cooling near the blowdown outlet. The pressure and temperature results therefore demonstrate that depressurisation must be treated non-isothermally when evaluating the thermal behaviour of the TSA bed.

Following blowdown, the bed pressure remained close to atmospheric pressure during the staged heating and cooling steps. The enlarged low-pressure region shows that the pressure was maintained at approximately

$$P_{\mathrm{regen}} \approx 1\ \mathrm{bar}.$$

Only small deviations above $1\ \mathrm{bar}$ were observed during the regeneration period. These variations were associated with changes in the regeneration-gas flow rate and valve configuration between the individual heating and cooling stages. The deviations were small and did not result in a meaningful pressurisation of the bed.

Maintaining the bed close to $1\ \mathrm{bar}$ during heating assisted regeneration in two ways. First, the elevated temperature reduced the equilibrium water loading of Zeolite 4A. Second, the low water partial pressure in the dry purge gas provided a driving force for desorption. The combination of heating and low-pressure purging therefore produced the substantial reduction in solid water loading observed during regeneration.

At approximately $35,500\ \mathrm{s}$, the waste connection was closed and the bed was repressurised using dry hydrogen. The pressure increased from approximately $1\ \mathrm{bar}$ to the adsorption pressure of $25\ \mathrm{bar}$ by the end of the cycle:

$$P_{\mathrm{final}} \approx 25\ \mathrm{bar}.$$

The pressure increased rapidly at the beginning of repressurisation and then approached the final pressure more gradually.

The profiles at all three axial nodes remained closely aligned during blowdown, regeneration and repressurisation. This indicates that the bed pressure responded nearly uniformly and that no substantial axial pressure imbalance developed during valve switching. The selected blowdown and repressurisation durations were therefore sufficient to reach the required low- and high-pressure conditions before the subsequent cycle steps began.

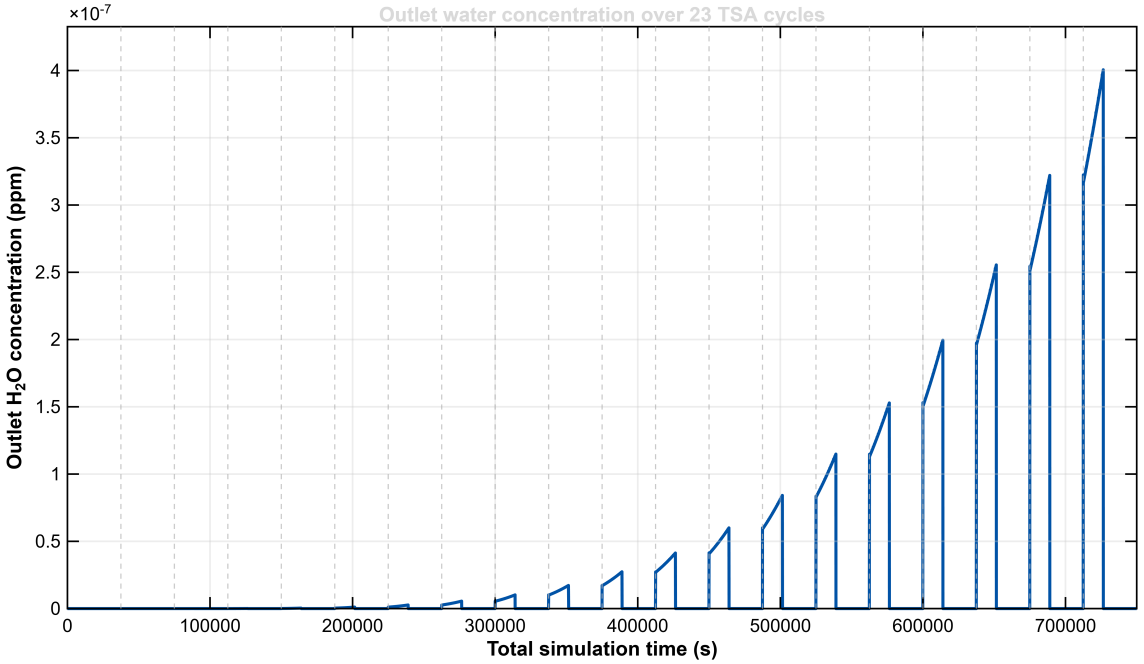

Figure 4.6: Outlet water concentration during the multi-cycle TSA simulation. The concentration peaks correspond to the adsorption period of each cycle.

4.6. Outlet Water Concentration During Multi-Cycle Operation

The outlet water concentration during the complete multi-cycle TSA simulation is presented in Figure 4.6. The results were used to determine whether the dried hydrogen continued to satisfy the required product-water specification over successive adsorption and regeneration cycles.

During each adsorption step, the outlet water concentration increased gradually with time. At the end of the adsorption step, the concentration returned to approximately zero because the product outlet was closed during the subsequent blowdown, heating, cooling and repressurisation steps.

The maximum outlet water concentration increased progressively over the successive cycles. The first cycles produced an outlet concentration close to zero, while the maximum concentration during the final simulated cycle was approximately

$$C_{\mathrm{H_2O,out,max}} \approx 4.0 \times 10^{-7}$$

ppm in Figure 4.6.

The increase in the cycle-wise concentration maxima is mainly related to the transition from the initially dry bed towards its normal cyclic operating condition. A small residual water loading remained after each regeneration step. During the following cycles, the water-loading profile was therefore redistributed through the bed and the mass-transfer zone moved slightly further towards the product end.

This increase does not indicate continuous accumulation of water in the adsorbent. As shown by the solid-loading results in Section 4.7, the maximum and residual loadings became nearly repeatable during the later cycles. The amount of water adsorbed and removed during each cycle therefore approached a balance as the bed moved towards cyclic steady state.

Nevertheless, the outlet water concentration remained considerably below the required product specification of

$$C_{\mathrm{H_2O,spec}} = 5 \text{ ppm}$$

during all simulated cycles. Therefore, no water breakthrough occurred during the selected adsorption duration of $14\,000$ s, and the TSA system continued to produce hydrogen satisfying the specified moisture requirement.

Overall, the multi-cycle results demonstrate that the selected adsorption time provided a sufficient safety margin against breakthrough. The TSA bed maintained the required hydrogen dryness throughout the simulated operation, despite the gradual increase in outlet water concentration over successive cycles.

4.7. Cyclic Steady-State Behaviour

Cyclic steady state (CSS) is reached when the state of the adsorption bed at a given position and at the same time within the cycle becomes independent of the cycle number. In the present simulation, CSS was reached after 23 cycles using a cyclic convergence tolerance of 1×10^{-3} in Aspen Adsorption. This indicates that the changes between consecutive cycles were within the specified numerical tolerance. The CSS condition can be expressed generally as

$$X_i^{(n+1)}(t_c) \approx X_i^{(n)}(t_c),$$

where X_i represents a state variable, such as solid loading, temperature or pressure, at axial position i, n is the cycle number and t_c is the elapsed time within an individual cycle. Therefore long-term stability of the TSA process was investigated through a simulation of 23 consecutive cycles. Each cycle had a duration of $37\,500$ s, resulting in a total simulated operating time of

$$t_{\text{total}} = 23 \times 37\,500 = 862\,500 \text{ s}.$$

Solid-loading behaviour over successive cycles

The water loading at selected axial positions over the complete 23-cycle simulation is presented in Figure 4.7.

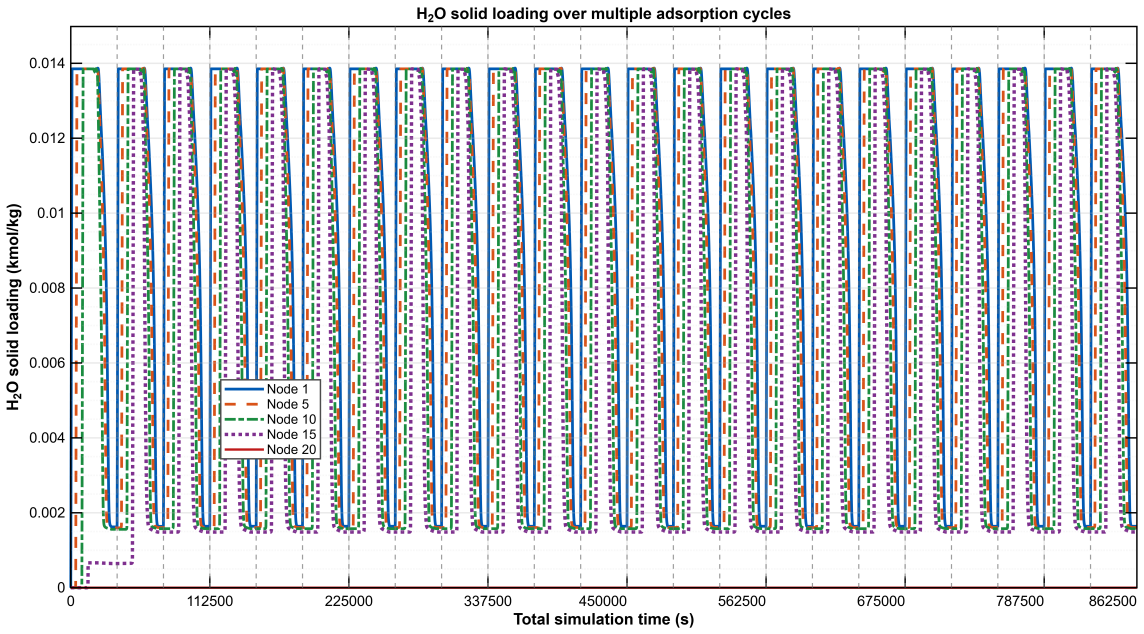

Figure 4.7: Water loading on Zeolite 4A at selected axial positions over 23 consecutive TSA cycles.

The first cycle differed from the subsequent cycles because the simulation was initialised with a nearly water-free adsorption bed. During this start-up cycle, the water adsorption front progressed from the feed end towards the product end of the bed. The loading increased first at Node 1, followed by Nodes 5, 10 and 15.

After the initial cycle, the maximum and minimum solid-loading values became highly repeatable. At Nodes 1, 5, 10 and 15, the maximum loading during adsorption was approximately

$$q_{\max} \approx 0.0138 \text{ kmol kg}^{-1}.$$

During regeneration, the loading at these positions decreased to approximately

$$q_{\min} \approx (1.8) \times 10^{-3} \text{ kmol kg}^{-1}.$$

The corresponding local working capacity was therefore approximately

$$\Delta q = q_{\max} - q_{\min} \approx 0.0138 - 0.0018 = 0.012 \text{ kmol kg}^{-1}.$$

The similarity between the loading profiles of successive cycles indicates that the quantity of water adsorbed and desorbed in the main active region of the bed became nearly constant. No progressive increase in the minimum loading was visible at Nodes 1, 5, 10 and 15, suggesting that significant bulk water accumulation did not occur within these regions.

Node 20, located near the dry-product end of the bed, remained essentially unloaded on the scale shown in Figure 4.7. This indicates that the adsorption front did not reach the final section of the bed during the selected adsorption time. The remaining dry adsorbent therefore acted as a protective section against water breakthrough.

The loading profile at Node 15 changed noticeably between the first and second cycles. During the first cycle, the initially dry bed prevented a large water loading from developing at this position. In the subsequent cycles, residual water redistribution and the repeated progression of the mass-transfer zone caused Node 15 to participate more fully in the cyclic adsorption and regeneration process. After this initial adjustment, its maximum and minimum loading values became repeatable.

Temperature behaviour over successive cycles

The gas-temperature profiles over the 23 cycles are shown in Figure 4.8. The corresponding solid temperatures were nearly identical and are therefore not presented separately.

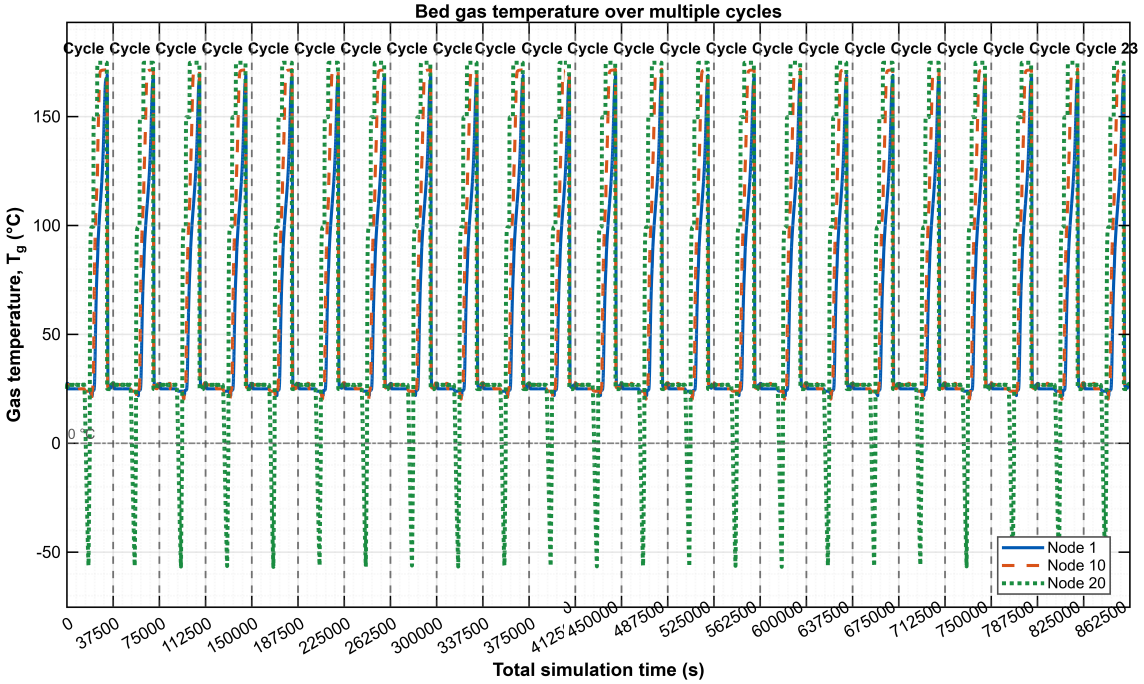

Figure 4.8: Gas-temperature profiles at selected axial positions over 23 consecutive TSA cycles.

The temperature profiles displayed a consistent pattern during every cycle. During adsorption, the bed temperature remained close to

$$T_{\mathrm{ads}} \approx 25^{\circ}\mathrm{C}.$$

A strong local temperature decrease occurred at Node 20 during blowdown, with a minimum temperature of approximately

$$T_{\mathrm{min}} \approx -55^{\circ}\mathrm{C}.$$

This temperature reduction occurred repeatedly during each cycle and was associated with the rapid pressure decrease and expansion of hydrogen near the blowdown outlet.

During regeneration, the temperature increased progressively as the hot purge gas passed countercurrently through the bed. Node 20 heated first, followed by Nodes 10 and 1. The maximum temperature reached approximately

$$T_{\mathrm{regen,max}} \approx 170\text{–}175^{\circ}\mathrm{C}$$

during every cycle.

Following regeneration, the cooling step returned the bed to approximately $25^{\circ}\mathrm{C}$ before the next adsorption step. The maximum, minimum and final temperatures remained nearly unchanged from one cycle to the next. Consequently, no progressive heat accumulation or incomplete cooling was observed over the 23-cycle simulation.

The repeatability of the temperature profiles indicates that the bed attained a periodic thermal state. The selected heating and cooling durations were therefore sufficient to reproduce approximately the same thermal conditions during each successive cycle.

Pressure behaviour over successive cycles

The bed-pressure profiles over the complete 23 cycles are presented in Figure 4.9.

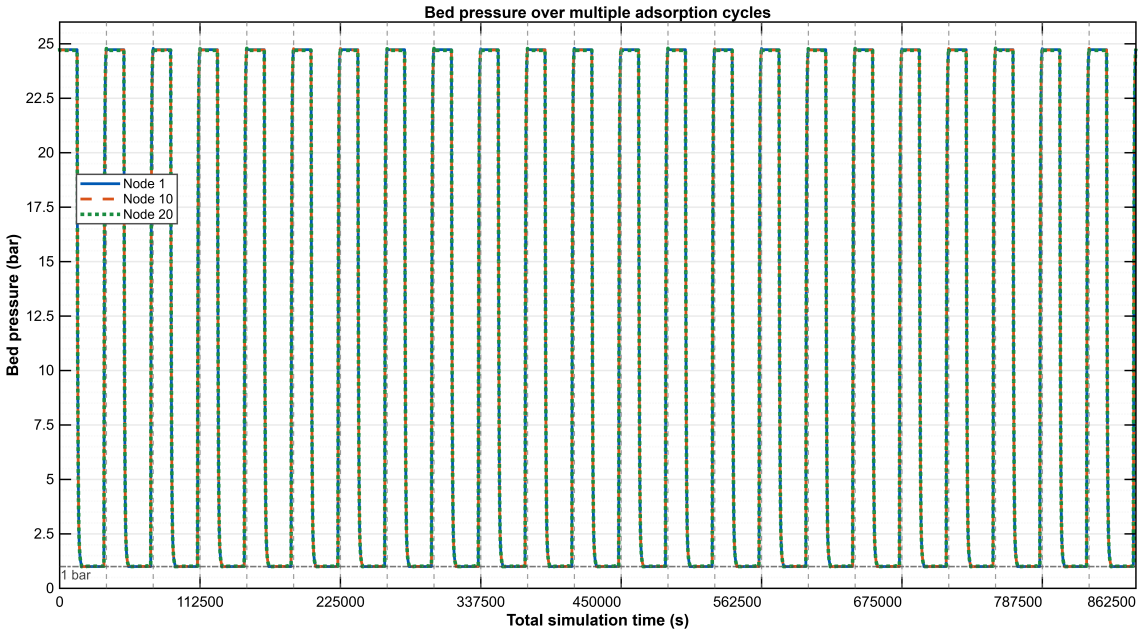

Figure 4.9: Bed-pressure profiles at selected axial positions over 23 consecutive TSA cycles.

The pressure followed an almost identical profile during each cycle. During adsorption, the bed was maintained at approximately

$$P_{\mathrm{ads}} \approx 25 \text{ bar}.$$

The pressure was subsequently reduced to approximately

$$P_{\mathrm{regen}} \approx 1 \text{ bar}$$

during blowdown and remained close to this value throughout the heating and cooling stages. At the end of each cycle, the bed was repressurised to the adsorption pressure.

The pressure curves at Nodes 1, 10 and 20 almost completely overlapped during all 23 cycles. This indicates that the axial pressure gradients were small and that no progressive pressure imbalance developed within the bed. The selected valve coefficients and step durations therefore consistently established the required adsorption and regeneration pressures.

4.7.1. Assessment of cyclic steady state

The repeated pressure and temperature profiles demonstrate that the pressure and thermal conditions reached periodic operation. Similarly, the solid loading in the main active region of the adsorption bed displayed nearly constant maximum and minimum values after the initial start-up cycle. These results indicate that the TSA system approached cyclic steady-state operation within the simulated period.

However, the outlet-water concentration showed a small progressive increase over the 23 cycles, although it remained substantially below the 5 ppmv product specification. This trace-level increase was not visible in the solid-loading profiles because the corresponding change in loading near the product end was extremely small compared with the scale of Figure 4.7.

Overall, the 23-cycle simulation demonstrated stable and repeatable TSA operation. The adsorbent working capacity, regeneration temperature and bed pressure were maintained over successive cycles, while the final dry section of the bed prevented water breakthrough and maintained the required product quality.

The repeatability of the pressure, temperature and solid-loading profiles is important when interpreting the small increase in outlet-water concentration seen during the start-up cycles. The first cycle starts from an almost dry bed, while later cycles start with the residual loading left after regeneration. The bed therefore develops its normal cyclic loading profile over the first several cycles. Once the maximum and minimum solid loadings became nearly repeatable, there was no evidence of continuing bulk water accumulation in the main active region of the bed. The multi-cycle behaviour is therefore interpreted as approach to cyclic steady state rather than an unbounded increase in water inventory.

4.8. Overall TSA Process Performance

The overall separation performance of the TSA process was evaluated in terms of product hydrogen purity, hydrogen recovery and hydrogen productivity. The calculations were performed using the results obtained from the 23-cycle Aspen Adsorption simulation.

Product Hydrogen Purity

The product-stream composition reported by Aspen Adsorption was

$$C_{\mathrm{H_2,product}} = 999\,999.9999998651 \text{ ppm},$$

and

$$C_{\mathrm{H_2O,product}} = 1.3504 \times 10^{-7} \text{ ppm}.$$

The hydrogen purity was calculated from

$$\text{Hydrogen purity} = \frac{C_{\mathrm{H_2,product}}}{10^6} \times 100.$$

Substitution of the Aspen result gives

$$\text{Hydrogen purity} = \frac{999\,999.9999998651}{10^6} \times 100 = 99.9999999999865\%.$$

Therefore, the product hydrogen purity can be reported as

$$\boxed{\text{Hydrogen purity} > 99.9999999\%}$$

for the simulated hydrogen–water system.

The corresponding product-water concentration was considerably below the specified limit of $5\ \mathrm{ppm}$:

$$1.3504 \times 10^{-7}\ \mathrm{ppmv} \ll 5\ \mathrm{ppmv}.$$

The simulation therefore demonstrated that the selected TSA cycle produced hydrogen satisfying the required moisture specification throughout the investigated operation. The extremely small water concentration reported by Aspen is close to the numerical precision of the simulation and should therefore be interpreted as an effectively water-free product rather than as an experimentally measurable level of precision.

Hydrogen Recovery

Hydrogen recovery was defined as the fraction of hydrogen supplied during the adsorption step that remained available as net dry-hydrogen product after accounting for the hydrogen consumed internally during heating, cooling and repressurisation:

$$R_{\mathrm{H_2}} = \frac{n_{\mathrm{H_2,feed}} - n_{\mathrm{H_2,internal}}}{n_{\mathrm{H_2,feed}}} \times 100. \tag{4.2}$$

For the selected TSA cycle, the hydrogen supplied during adsorption was

$$n_{\mathrm{H_2,feed}} = 311.93\ \mathrm{kmol\,cycle^{-1}},$$

while the total hydrogen consumed internally during regeneration, cooling and repressurisation was

$$n_{\mathrm{H_2,internal}} = 17.72\ \mathrm{kmol\,cycle^{-1}}.$$

The net hydrogen available as product was therefore

$$n_{\mathrm{H_2,net}} = 294.21\ \mathrm{kmol\,cycle^{-1}},$$

resulting in a hydrogen recovery of

$$\boxed{R_{\mathrm{H_2}} = 94.32\%}. \tag{4.3}$$

The recovery calculation assumes that the hydrogen required for heating, cooling and repressurisation was withdrawn from the purified product stream and was therefore deducted from the gross hydrogen production. Detailed calculations of the hydrogen consumption during the individual cycle steps are provided in Appendix A.

Hydrogen Productivity

Hydrogen productivity was evaluated using the net hydrogen production after accounting for the hydrogen consumed internally during regeneration, cooling and repressurisation. For the selected TSA cycle, the net hydrogen production was

$$m_{\mathrm{H_2,net}} = 588.42\ \mathrm{kg\,cycle^{-1}}.$$

In the staggered three-bed configuration, an adsorption-production interval was completed every $14\,000\ \mathrm{s}$. The corresponding average net hydrogen-production rate of the complete plant was therefore

$$\dot{m}_{\mathrm{H_2,plant}} = 151.3\ \mathrm{kg\,h^{-1}}.$$

The adsorbent productivity of the continuous three-bed system was defined as

$$\Pi_{\mathrm{H_2,plant}} = \frac{\dot{m}_{\mathrm{H_2,plant}}}{m_{\mathrm{ads,total}}}, \tag{4.4}$$

where the total Zeolite 4A inventory of the three beds was $84\ \mathrm{kg}$. The resulting continuous-plant productivity was

$$\boxed{\Pi_{\mathrm{H_2,plant}} = 1.80\ \mathrm{kg_{H_2}\,kg_{ads}^{-1}\,h^{-1}}}. \tag{4.5}$$

This value was used as the principal productivity indicator because it accounts for the combined adsorbent inventory and staggered operation of all three TSA beds. Detailed calculations of the gross and net hydrogen production are provided in Appendix A.

4.8.1. Heating Duty of the Regeneration Hydrogen

During regeneration, a fraction of the purified hydrogen product was heated and introduced countercurrently through the adsorption bed. The heating sequence consisted of two stages at $100^{\circ}\mathrm{C}$, followed by stages at $150^{\circ}\mathrm{C}$ and $175^{\circ}\mathrm{C}$.

The temperature-dependent enthalpy of hydrogen was calculated using the Shomate equation from the NIST Chemistry WebBook [77]:

$$H^{\circ}(T) - H^{\circ}_{298.15} = At + \frac{Bt^2}{2} + \frac{Ct^3}{3} + \frac{Dt^4}{4} - \frac{E}{t} + F - H, \qquad t = \frac{T}{1000}. \tag{4.6}$$

Using $25^{\circ}\mathrm{C}$ as the reference temperature, the calculated molar enthalpy increases of hydrogen were

$$\Delta h_{25\to100} = 2176.06\ \mathrm{kJ\,kmol^{-1}},$$

$$\Delta h_{25\to150} = 3634.89\ \mathrm{kJ\,kmol^{-1}},$$

and

$$\Delta h_{25\to175} = 4365.41\ \mathrm{kJ\,kmol^{-1}}.$$

The thermal duty during each heating stage was obtained from

$$\dot{Q}_j = \dot{n}_{\mathrm{H_2},j}\Delta h_j, \tag{4.7}$$

and the corresponding thermal energy was calculated from

$$E_j = \dot{Q}_j \Delta t_j. \tag{4.8}$$

Summation over the four heating stages resulted in a total sensible energy requirement for the regeneration hydrogen of

$$\boxed{E_{\text{thermal,cycle}} = 47.13\ \text{MJ}\,\text{cycle}^{-1}}. \tag{4.9}$$

For a heater efficiency of $\eta_{\text{heater}} = 0.90$, the corresponding electrical energy supplied to the heater was

$$E_{\text{electrical,cycle}} = \frac{E_{\text{thermal,cycle}}}{\eta_{\text{heater}}} = 14.55\ \text{kWh}\,\text{cycle}^{-1}.$$

The maximum instantaneous thermal duty occurred during the 175°C heating stage and was

$$\dot{Q}_{\text{thermal,max}} = 4.365\ \text{kW}.$$

Accounting for the heater efficiency, the corresponding maximum electrical input was

$$\dot{W}_{\text{heater,max}} = \frac{\dot{Q}_{\text{thermal,max}}}{\eta_{\text{heater}}} = 4.85\ \text{kW}. \tag{4.10}$$

Applying a design factor of 1.20 resulted in a required design capacity of approximately $5.82\ \text{kW}$. A nominal heater capacity of

$$\boxed{\dot{W}_{\text{heater,selected}} \approx 6\ \text{kW}} \tag{4.11}$$

was therefore selected.

The value of $47.13\ \text{MJ}\,\text{cycle}^{-1}$ represents the sensible energy supplied to the regeneration hydrogen and should not be interpreted as the thermal demand of the adsorption bed itself. The energy required to heat the Zeolite 4A and vessel wall and to overcome the heat of water desorption is evaluated separately in Section 4.8.2. Detailed calculations for the individual regeneration-heating stages are provided in Appendix A.

4.8.2. Thermal Energy Required for Bed Regeneration

In addition to heating the regeneration hydrogen, thermal energy is required within the adsorber to heat the Zeolite 4A, desorb the adsorbed water, and heat the steel vessel wall. The theoretical bed-regeneration energy was therefore estimated from

$$Q_{\text{regen,bed}} = Q_{\text{zeolite}} + Q_{\text{desorption}} + Q_{\text{wall}}. \tag{4.12}$$

The working adsorption capacity was determined from the difference between the water loading at the end of adsorption and the residual loading after regeneration:

$$\Delta q = q_{\text{end,ads}} - q_{\text{end,regen}}. \tag{4.13}$$

Using $q_{\text{end,ads}} = 0.0138\ \text{kmol}\,\text{kg}^{-1}$ and $q_{\text{end,regen}} = 0.0018\ \text{kmol}\,\text{kg}^{-1}$, the working capacity was approximately

$$\Delta q = 0.0120\ \text{kmol}\,\text{kg}^{-1}.$$

For one TSA bed containing approximately $28\ \mathrm{kg}$ of Zeolite 4A, the individual thermal contributions were calculated as

$$Q_{\mathrm{zeolite}} = 3.65\ \mathrm{MJ\,cycle^{-1}},$$

$$Q_{\mathrm{desorption}} = 19.81\ \mathrm{MJ\,cycle^{-1}},$$

and

$$Q_{\mathrm{wall}} = 1.72\ \mathrm{MJ\,cycle^{-1}}.$$

The resulting theoretical regeneration-energy requirement was therefore

$$\boxed{Q_{\mathrm{regen,bed}} = 25.18\ \mathrm{MJ\,cycle^{-1}\,bed^{-1}} \approx 25.2\ \mathrm{MJ\,cycle^{-1}\,bed^{-1}}}. \tag{4.14}$$

The previously calculated $47.13\ \mathrm{MJ\,cycle^{-1}}$ represents the sensible enthalpy supplied to the regeneration hydrogen, whereas $25.18\ \mathrm{MJ\,cycle^{-1}\,bed^{-1}}$ represents an independent estimate of the thermal demand within the adsorber. These quantities are not additive, since heat transferred from the regeneration gas supplies the sensible heating and water-desorption requirements of the bed.

Detailed calculations of the adsorbent heating, water desorption and vessel-wall heating contributions are provided in Appendix A.

4.8.3. Cooling Duty

Following regeneration, the adsorption bed was cooled using dry hydrogen before repressurisation and the subsequent adsorption step. The cooling requirement was estimated from the sensible heat removed from the Zeolite 4A and the steel vessel wall:

$$Q_{\mathrm{cool,total}} = Q_{\mathrm{cool,ads}} + Q_{\mathrm{cool,wall}}. \tag{4.15}$$

The bed temperature decreased from approximately $169^{\circ}\mathrm{C}$ at the end of heating to approximately $25^{\circ}\mathrm{C}$ at the end of cooling. The corresponding sensible heat contributions were

$$Q_{\mathrm{cool,ads}} = 3.63\ \mathrm{MJ\,cycle^{-1}},$$

and

$$Q_{\mathrm{cool,wall}} = 1.71\ \mathrm{MJ\,cycle^{-1}}.$$

The total cooling-energy requirement for one bed was therefore

$$\boxed{Q_{\mathrm{cool,total}} = 5.34\ \mathrm{MJ\,cycle^{-1}\,bed^{-1}}}. \tag{4.16}$$

For a cooling-step duration of $3000\ \mathrm{s}$, the average cooling duty was calculated from

$$\dot{Q}_{\mathrm{cool}} = \frac{Q_{\mathrm{cool,total}}}{\Delta t_{\mathrm{cool}}}, \tag{4.17}$$

giving

$$\dot{Q}_{\mathrm{cool}} = 1.78\ \mathrm{kW}.$$

Applying a design factor of 1.20 increased the required cooling capacity to approximately $2.14\ \mathrm{kW}$. A nominal cooling-gas cooler capacity of

$$\boxed{\dot{Q}_{\mathrm{cool,selected}} = 2.5\ \mathrm{kW}} \tag{4.18}$$

was therefore selected for equipment sizing.

The calculation considers the sensible heat removed from the adsorbent and the cylindrical vessel wall. Additional thermal contributions associated with the vessel heads, piping, insulation and heat transfer to the surroundings were not explicitly included. Detailed cooling-duty calculations are provided in Appendix A.

4.8.4. Hydrogen Compression Duty

The wet-hydrogen feed from the electrolyser was compressed from $10\ \mathrm{bar}$ to the TSA adsorption pressure of $25\ \mathrm{bar}$. The compressor calculation was based on an inlet temperature of $298\ \mathrm{K}$, a hydrogen flow rate of $0.0223\ \mathrm{kmol\,s^{-1}}$, and an isentropic efficiency of $\eta_s = 0.75$.

The isentropic outlet temperature was estimated from

$$\frac{T_{2,s}}{T_1} = \left(\frac{P_2}{P_1}\right)^{(k-1)/k}, \tag{4.19}$$

where $k = 1.4$ was used for hydrogen. The calculated isentropic outlet temperature was

$$T_{2,s} = 387.2\ \mathrm{K}.$$

The required compressor shaft power was determined from

$$\dot{W}_{\mathrm{shaft}} = \frac{\dot{n}_{\mathrm{feed}} C_{p,\mathrm{H_2}} \left(T_{2,s} - T_1\right)}{\eta_s}, \tag{4.20}$$

giving

$$\boxed{\dot{W}_{\mathrm{shaft}} = 76.9\ \mathrm{kW}}.$$

Assuming a motor efficiency of $\eta_{\mathrm{motor}} = 0.95$, the corresponding electrical input was

$$\dot{W}_{\mathrm{electric}} = \frac{\dot{W}_{\mathrm{shaft}}}{\eta_{\mathrm{motor}}} = 80.9\ \mathrm{kW}. \tag{4.21}$$

Applying a design factor of 1.10 resulted in a required motor capacity of approximately $89\ \mathrm{kW}$. A nominal compressor-motor rating of

$$\boxed{\dot{W}_{\mathrm{motor,selected}} \approx 90\ \mathrm{kW}} \tag{4.22}$$

was therefore selected.

The actual compressor discharge temperature was approximately

$$\boxed{T_{2,\mathrm{actual}} \approx 417\ \mathrm{K} \approx 144^{\circ}\mathrm{C}}. \tag{4.23}$$

The compressor shaft power of $76.9\ \mathrm{kW}$ represents the mechanical power requirement, while the $80.9\ \mathrm{kW}$ electrical input accounts for the motor efficiency. The latter was used to determine the compressor electricity consumption. Detailed compressor calculations are provided in Appendix A.

4.8.5. Compressor Aftercooler Duty

Compression increased the hydrogen temperature from approximately $25^{\circ}\mathrm{C}$ to $144^{\circ}\mathrm{C}$. An aftercooler was therefore required to reduce the compressed-gas temperature back to the TSA adsorption temperature of approximately $25^{\circ}\mathrm{C}$.

The aftercooler duty was estimated from

$$\dot{Q}_{\mathrm{AC}} = \dot{n}_{\mathrm{feed}} C_{p,\mathrm{H_2}} \left(T_{2,\mathrm{actual}} - T_{\mathrm{AC,out}}\right). \tag{4.24}$$

For the selected operating conditions, the required thermal duty was

$$\boxed{\dot{Q}_{\mathrm{AC}} = 76.9\ \mathrm{kW}}. \tag{4.25}$$

The similarity between the calculated aftercooler duty and compressor shaft power results from cooling the hydrogen approximately back to its initial inlet temperature following the assumed adiabatic compression.

Applying a design factor of 1.10 resulted in a design duty of approximately

$$\dot{Q}_{\mathrm{AC,design}} = 84.6\ \mathrm{kW}.$$

A nominal aftercooler capacity of

$$\boxed{\dot{Q}_{\mathrm{AC,selected}} \approx 85\ \mathrm{kW}} \tag{4.26}$$

was therefore selected. Detailed calculations are provided in Appendix A.

4.8.6. Continuous Three-Bed Operating Arrangement

To provide a continuous supply of dried hydrogen, three adsorption beds were operated in a staggered sequence. The simulated TSA cycle consisted of adsorption, blowdown, staged heating, cooling and repressurisation, with a total cycle duration of

$$t_{\mathrm{cycle}} = 37\,500\ \mathrm{s}.$$

The adsorption step occupied

$$t_{\mathrm{ads}} = 14\,000\ \mathrm{s}.$$

The minimum number of beds required for continuous operation was estimated from

$$N_{\mathrm{beds,min}} = \left\lceil \frac{t_{\mathrm{cycle}}}{t_{\mathrm{ads}}} \right\rceil, \tag{4.27}$$

which gives

$$\boxed{N_{\mathrm{beds,min}} = 3}.$$

The adsorption periods of the three beds were therefore offset by $14\,000\ \mathrm{s}$. Bed A adsorbed from 0 to $14\,000\ \mathrm{s}$, Bed B from $14\,000$ to $28\,000\ \mathrm{s}$, and Bed C from $28\,000$ to $42\,000\ \mathrm{s}$, after which the sequence was repeated.

Each bed consequently returned to adsorption after

$$t_{\mathrm{bed,repeat}} = 3t_{\mathrm{ads}} = 42\,000\ \mathrm{s}.$$

Since the simulated TSA sequence required $37\,500\ \mathrm{s}$, the remaining time available before the next adsorption period was

$$t_{\mathrm{standby}} = t_{\mathrm{bed,repeat}} - t_{\mathrm{cycle}} = 4\,500\ \mathrm{s}. \tag{4.28}$$

Each bed therefore completed blowdown, heating, cooling and repressurisation before entering a $4\,500\,\mathrm{s}$ pressurised standby period. During standby, the bed was assumed to remain isolated at approximately $25\ \mathrm{bar}$ and close to the adsorption temperature. Since dry hydrogen was used during cooling and repressurisation, significant water readsorption during this period was not expected.

The $4\,500\ \mathrm{s}$ standby period was not explicitly included in the original $37\,500\ \mathrm{s}$ Aspen Adsorption multi-cycle simulation. Negligible changes in bed temperature and adsorbent loading during this additional period were therefore assumed when extending the simulated cycle to the continuous three-bed arrangement.

The staggered configuration ensures that at least one bed remains in adsorption at all times. Consequently, the feed compressor and compressor aftercooler can operate continuously at the selected feed rate of

$$\dot{n}_{\mathrm{feed}} = 0.0223\ \mathrm{kmol\,s^{-1}}.$$

A common regeneration heater and cooling-gas cooler were assumed to be shared between the three beds using automated switching valves. The complete heating sequence of an individual bed lasts $15\,000\ \mathrm{s}$, which is $1000\ \mathrm{s}$ longer than the $14\,000\ \mathrm{s}$ staggered adsorption interval. This nominal overlap occurs during the initial $100^{\circ}\mathrm{C}$ heating stage of the following bed, for which the thermal duty is negligible compared with the subsequent heating stages.

The shared-heater arrangement therefore assumes that this initial low-flow heating stage can be rescheduled within the available $4\,500\ \mathrm{s}$ standby margin. This avoids simultaneous significant heating demand from two beds while maintaining the $14\,000\ \mathrm{s}$ continuous production interval.

The staggered arrangement converts the single-bed cycle into a continuous production concept. It also allows the feed compressor and aftercooler to operate continuously. The $4\,500\ \mathrm{s}$ standby period and the sharing of the regeneration heater and cooling-gas cooler are process-integration assumptions derived from the single-bed cycle. They should therefore be checked in a future fully integrated three-bed dynamic simulation, especially to confirm that the bed state does not change significantly during standby and that the switching schedule avoids simultaneous high thermal demand.

Detailed timing calculations for the staggered three-bed cycle are provided in Appendix A.

Process-performance interpretation The final TSA configuration achieved a hydrogen recovery of 94.32% while maintaining the required product-water specification. The main hydrogen loss was the dry product gas reused for regeneration, cooling and repressurisation. The compressor was the largest continuous electrical load, whereas the regeneration heater had a relatively small peak electrical requirement. For operating-cost calculations, the regeneration-gas energy of $47.13\ \mathrm{MJ\,bed^{-1}\,cycle^{-1}}$ is more relevant than the peak heater power alone. The separate $25.18\ \mathrm{MJ\,bed^{-1}\,cycle^{-1}}$ calculation represents the theoretical thermal demand of the adsorbent, desorbed water and vessel wall; it is supplied by the hot regeneration gas and is therefore not added to the regeneration-gas enthalpy requirement.

4.9. Techno-Economic Analysis

The techno-economic performance of the proposed three-bed TSA hydrogen-drying process was evaluated using OpenPyTEA. The analysis represents the incremental cost of the hydrogen-drying section and therefore excludes the upstream cost of hydrogen production by electrolysis. The final economic boundary includes the hydrogen compressor, compressor aftercooler, three TSA pressure vessels,

regeneration-gas heater, TSA cooling-gas cooler and waste receiver. A separate dry-hydrogen storage vessel was not included because regeneration, cooling and repressurisation gas were assumed to be supplied from the common dry-product header of the integrated hydrogen facility.

4.9.1. Capital-Cost Results

The purchased-equipment costs estimated with the selected OpenPyTEA correlations are summarised in Table 4.1. The hydrogen compressor was the largest purchased-cost item, followed by the compressor aftercooler and the three TSA pressure vessels.

Table 4.1: Purchased-equipment costs estimated using OpenPyTEA for the final TSA process boundary.

Equipment	Purchased cost (EUR)
Hydrogen compressor	457,386
Compressor aftercooler	184,147
Three TSA pressure vessels	88,656
Regeneration-gas heater	36,737
TSA cooling-gas cooler	23,571
Waste receiver	23,426
Total purchased equipment	**813,923**

The compressor accounts for approximately 56% of the purchased-equipment subtotal. The three TSA vessels contribute a much smaller share because their physical size is small. For costing, however, the vessel mass was below the lower validity limit of the corresponding OpenPyTEA correlation and the minimum allowable correlation value was therefore used as a costing floor. Similarly, the reciprocating-compressor correlation was evaluated at its $93\ \mathrm{kW}$ lower costing limit, while the actual process shaft-power requirement remained $76.9\ \mathrm{kW}$. The regeneration-gas heater was represented economically by the OpenPyTEA duty-based heat-exchanger correlation, using a design thermal duty of $5.238\ \mathrm{kW}$.

The purchased costs were converted to installed and fixed-capital costs using the standard OpenPyTEA installation methodology. No external reduction of the OpenPyTEA installation factors was applied. The resulting direct-installed cost was $2.652\ \mathrm{million\ EUR}$, corresponding to an overall direct-installed-to-purchased-cost ratio of approximately 3.26 for the combined equipment set. The final capital-cost breakdown is given in Table 4.2.

Table 4.2: Capital-cost results for the final three-bed TSA hydrogen-drying process.

Capital component	Cost (EUR)
Purchased equipment	813,923
Direct installed cost	2,652,428
ISBL	3,156,389
OSBL	631,278
Design and engineering	1,136,300
Contingency	378,767
Fixed capital investment	**5,302,733**

The resulting fixed capital investment was therefore

$$\boxed{C_{\mathrm{FCI}} = 5.303\ \mathrm{million\ EUR}}. \tag{4.29}$$

The difference between the purchased-equipment subtotal and the final fixed capital investment is substantial because OpenPyTEA includes installation, location, outside-battery-limits, design-and-engineering and contingency allowances. In the final base case, OSBL was taken as 20% of ISBL, whereas design

and engineering and contingency were retained at 30% and 10%, respectively. The result should therefore be interpreted as a factored screening-level capital estimate rather than a vendor-quoted project cost.

4.9.2. Operating-Cost Results

The principal variable operating cost considered in the final OpenPyTEA model was electricity consumption by the hydrogen compressor and regeneration-gas heater. The compressor electrical requirement was $80.9\ \mathrm{kW}$. The heater electricity consumption was calculated from the sensible energy supplied to the regeneration hydrogen,

$$Q_{\mathrm{regen,H_2}} = 47.13\ \mathrm{MJ\,bed^{-1}\,cycle^{-1}},$$

together with a heater efficiency of 90%, three TSA beds and a complete single-bed cycle time of $37\,500\ \mathrm{s}$. This corresponds to a total compressor-plus-heater electricity demand of approximately

$$E_{\mathrm{electricity}} \approx 2042\ \mathrm{kWh\,day^{-1}}.$$

At the base-case electricity price of $0.246\ \mathrm{EUR\,kWh^{-1}}$, the annual variable operating expenditure was

$$\boxed{C_{\mathrm{OPEX,var}} = 183{,}364\ \mathrm{EUR\,year^{-1}}}. \tag{4.30}$$

For the integrated drying-unit boundary, one full-time-equivalent operator was allocated to the TSA section. OpenPyTEA fixed-cost categories directly associated with operation of the drying unit were retained, including labour, supervision, salary overhead, maintenance, taxes and insurance, environmental charges, operating supplies and working-capital interest. Laboratory charges, additional land rent, general plant overhead, patents and royalties, distribution and selling, and research and development were treated as non-incremental costs of the wider hydrogen-production facility and were not charged again to the TSA unit.

The resulting fixed operating expenditure was

$$\boxed{C_{\mathrm{OPEX,fixed}} = 472{,}429\ \mathrm{EUR\,year^{-1}}}. \tag{4.31}$$

The fixed-OPEX breakdown is shown in Table 4.3. Maintenance is the largest fixed-cost component, followed by working-capital interest and direct labour.

Table 4.3: Fixed operating-cost breakdown for the integrated TSA drying section.

Fixed-OPEX component	Cost (EUR/year)	Share of fixed OPEX (%)
Labour	69,009	14.6
Supervision	17,252	3.7
Salary overhead	43,131	9.1
Maintenance	157,819	33.4
Taxes and insurance	47,346	10.0
Environmental charges	37,877	8.0
Operating supplies	28,407	6.0
Working-capital interest	71,587	15.2
Total fixed OPEX	**472,429**	**100.0**

The total annual operating expenditure was consequently

$$C_{\mathrm{OPEX,total}} = C_{\mathrm{OPEX,var}} + C_{\mathrm{OPEX,fixed}}, \tag{4.32}$$

giving

$$\boxed{C_{\mathrm{OPEX,total}} = 655{,}793\ \mathrm{EUR\,year^{-1}}}. \tag{4.33}$$

The overall OPEX split is summarised in Table 4.4.

Table 4.4: Annual operating-cost results obtained using OpenPyTEA.

OPEX component	Cost (EUR/year)	Share of total OPEX (%)
Variable OPEX	183,364	28.0
Fixed OPEX	472,429	72.0
Total OPEX	**655,793**	**100.0**

Fixed costs remain larger than the direct electricity cost, but they no longer dominate the economics to the extent expected for a stand-alone facility with its own full operating organisation. This is consistent with the selected incremental system boundary, in which the TSA unit is integrated with a larger hydrogen-production facility.

4.9.3. Levelized Cost of Hydrogen Drying

The continuous three-bed process produced dry hydrogen at an average rate of

$$\dot{m}_{\mathrm{H_2,plant}} = 151.3\ \mathrm{kg\,h^{-1}}.$$

At the deterministic base-case plant utilisation of 100%, the corresponding annual dry-hydrogen production was

$$m_{\mathrm{H_2,annual}} = 151.3(24)(365) \tag{4.34}$$

$$= 1.325388 \times 10^{6}\ \mathrm{kg\,year^{-1}}. \tag{4.35}$$

Using a project lifetime of 20 years, a discount rate of 9%, and the capital and operating costs described above, OpenPyTEA gave a deterministic levelized cost of hydrogen drying of

$$\boxed{LCOP_{\mathrm{base}} = 1.179\ \mathrm{EUR\,kg_{H_2}^{-1}}}. \tag{4.36}$$

The unrounded result was

$$LCOP_{\mathrm{base}} = 1.179195\ \mathrm{EUR\,kg_{H_2}^{-1}}.$$

This quantity represents the incremental levelized cost of the TSA drying section only. It is therefore not the total hydrogen-production cost and does not include the upstream electrolyser or other hydrogen-production equipment.

The calculated value is close to the order of $1\ \mathrm{EUR\,kg_{H_2}^{-1}}$, but remains slightly above it in the deterministic base case. No reduction was applied to the standard OpenPyTEA installation factors solely to force the result below $1\ \mathrm{EUR\,kg_{H_2}^{-1}}$. Consequently, the deterministic value retains the internally consistent OpenPyTEA factored-cost basis used throughout the economic analysis. The uncertainty analysis presented below shows that lower drying costs are nevertheless possible within the considered technical and economic uncertainty ranges.

4.9.4. Sensitivity Analysis

The relative influence of the uncertain technical and economic parameters was quantified using Spearman rank correlation coefficients. The resulting ranking is summarised in Table 4.5 and illustrated in Figure 4.10.

Table 4.5: Spearman rank correlation coefficients between uncertain inputs and levelized TSA drying cost.

Parameter	Spearman ρ_s
CAPEX multiplier	0.693
Interest rate	0.479
Project lifetime	-0.339
Dry-H_2 production rate	-0.240
Operator hourly rate	0.105
OSBL factor	0.103
Electricity price	0.094
Compressor electrical power	0.048
Regeneration energy	0.015
TSA cycle time	0.006

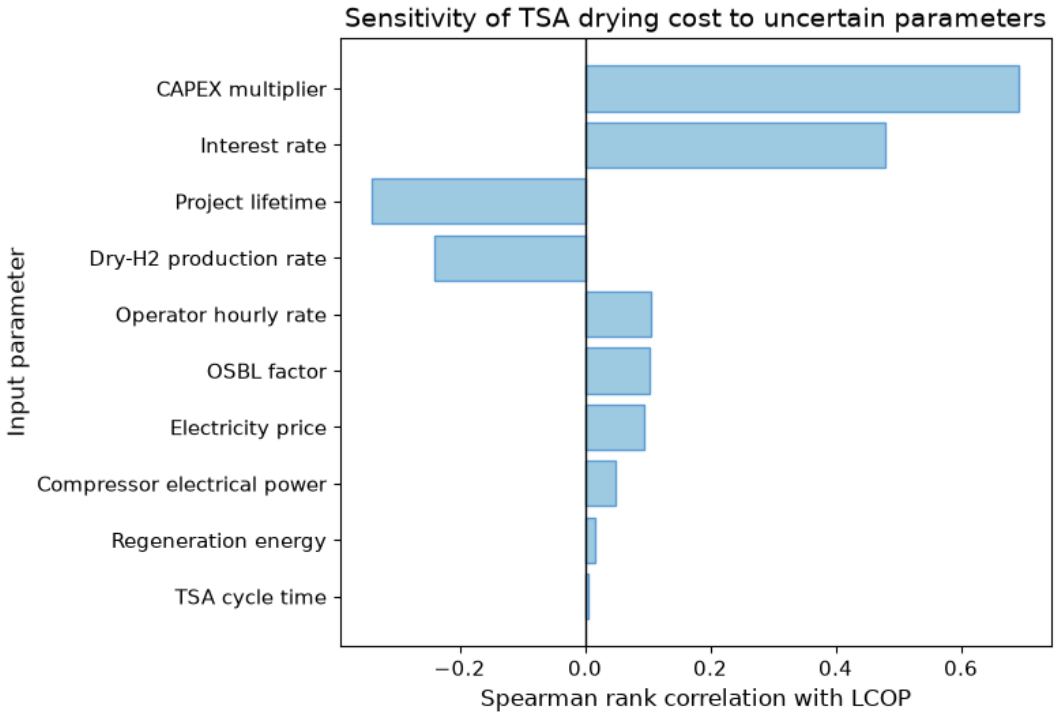

Figure 4.10: Spearman rank correlation coefficients between uncertain technical and economic input parameters and the levelized cost of TSA hydrogen drying. Positive coefficients indicate an increase in LCOP with increasing parameter value, whereas negative coefficients indicate an inverse relationship.

The CAPEX multiplier showed the strongest positive influence on LCOP ($\rho_s = 0.693$), followed by the interest rate ($\rho_s = 0.479$). Project lifetime showed the strongest negative influence ($\rho_s = -0.339$), because a longer economic life distributes the capital burden over a greater cumulative quantity of dry hydrogen. The dry-hydrogen production rate also showed a negative correlation ($\rho_s = -0.240$), reflecting the reduction in levelized cost when more product is obtained from essentially the same installed plant.

The operator hourly rate, OSBL factor and electricity price had comparatively small effects over their selected uncertainty ranges, while compressor electrical power had only a weak positive correlation.

Regeneration energy and TSA cycle time showed negligible rank correlations ($\rho_s = 0.015$ and 0.006, respectively); their corresponding p-values were greater than 0.05. Hence, within the ranges investigated, the uncertainty in LCOP was governed primarily by capital and financing assumptions rather than by modest variations in regeneration energy or cycle duration.

4.9.5. Monte Carlo Uncertainty Analysis

A combined technical–economic Monte Carlo analysis was performed using 10,000 realisations. The sampled economic variables were the CAPEX multiplier, OSBL factor, interest rate, project lifetime, electricity price and operator hourly rate. The sampled technical variables were compressor electrical power, regeneration energy, TSA cycle time and dry-hydrogen production rate. Each sampled variable was propagated through the corresponding physical or economic calculation rather than being applied as an arbitrary multiplier to the final LCOP.

The resulting LCOP distribution is summarised in Table 4.6.

Table 4.6: Results of the combined technical–economic Monte Carlo analysis based on 10,000 realisations.

Statistic	**LCOP (EUR $\mathrm{kg}_{\mathrm{H_2}}^{-1}$)**
Deterministic base case	1.179
Monte Carlo mean	1.232
Standard deviation	0.225
Median	1.211
2.5th percentile	0.852
5th percentile	0.901
95th percentile	1.636
97.5th percentile	1.723

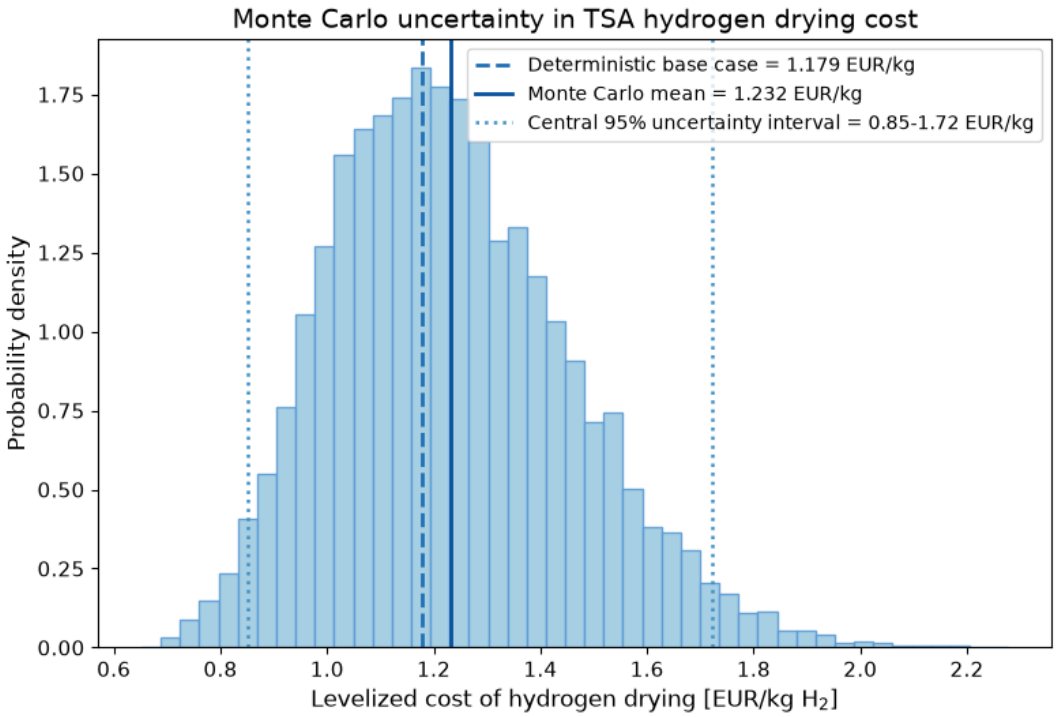

Figure 4.11: Monte Carlo distribution of the levelized TSA hydrogen-drying cost based on 10,000 combined technical and economic uncertainty realisations. The deterministic base case is $1.179\ \mathrm{EUR\,kg}_{\mathrm{H_2}}^{-1}$, while the Monte Carlo mean is $1.232\ \mathrm{EUR\,kg}_{\mathrm{H_2}}^{-1}$. The central 95% uncertainty interval extends from 0.852 to $1.723\ \mathrm{EUR\,kg}_{\mathrm{H_2}}^{-1}$.

The Monte Carlo mean was

$$\overline{LCOP} = 1.232\ \mathrm{EUR\,kg_{H_2}^{-1}}, \tag{4.37}$$

with a median of

$$1.211\ \mathrm{EUR\,kg_{H_2}^{-1}}.$$

The central 95% uncertainty interval was

$$\boxed{0.852 \leq LCOP \leq 1.723\ \mathrm{EUR\,kg_{H_2}^{-1}}}.$$

The deterministic value lies close to the centre of the Monte Carlo distribution. The slightly higher Monte Carlo mean reflects the nonlinear response of LCOP to combinations of capital cost, financing, project lifetime and production-rate uncertainty. The lower tail of the distribution extends below $1\ \mathrm{EUR\,kg_{H_2}^{-1}}$, while the upper tail remains above this value. The result therefore indicates that an incremental drying cost of approximately $1\ \mathrm{EUR\,kg_{H_2}^{-1}}$ is plausible, but the exact value is sensitive to the project-specific capital and financial assumptions.

4.9.6. Economic Assessment Summary

The principal economic results of the three-bed TSA hydrogen drying process are summarised in Table 4.7. The estimated fixed capital investment (FCI) is $5.303\ \mathrm{million\ EUR}$, while the total annual operating expenditure is approximately $0.656\ \mathrm{million\ EUR\,year^{-1}}$. At an annual dry-hydrogen production of $1.325388 \times 10^6\ \mathrm{kg\,year^{-1}}$, the deterministic levelised drying cost is $1.179\ \mathrm{EUR\,kg_{H_2}^{-1}}$.

Table 4.7: Principal techno-economic results for the three-bed TSA hydrogen drying process.

Economic indicator	Value
Purchased equipment cost	$0.814\ \mathrm{million\ EUR}$
Direct installed cost	$2.652\ \mathrm{million\ EUR}$
Fixed capital investment	$5.303\ \mathrm{million\ EUR}$
Variable OPEX	$0.183\ \mathrm{million\ EUR\,year^{-1}}$
Fixed OPEX	$0.472\ \mathrm{million\ EUR\,year^{-1}}$
Total OPEX	$0.656\ \mathrm{million\ EUR\,year^{-1}}$
Annual dry-H_2 production	$1.325388 \times 10^6\ \mathrm{kg\,year^{-1}}$
Deterministic levelised drying cost	$1.179\ \mathrm{EUR\,kg_{H_2}^{-1}}$
Monte Carlo mean	$1.232\ \mathrm{EUR\,kg_{H_2}^{-1}}$
Monte Carlo median	$1.211\ \mathrm{EUR\,kg_{H_2}^{-1}}$
Central 95% uncertainty interval	$0.852 - 1.723\ \mathrm{EUR\,kg_{H_2}^{-1}}$

The composition of the fixed capital investment is shown in Figure 4.12. The inside-battery-limits (ISBL) investment represents the largest contribution, accounting for approximately 59.5% of the total FCI, corresponding to $3.16\ \mathrm{million\ EUR}$. Design and engineering contribute a further 21.4%, while the outside-battery-limits (OSBL) investment and contingency account for 11.9% and 7.1%, respectively. The resulting distribution indicates that the economic performance of the TSA process is strongly influenced by the installed process equipment and the associated indirect capital requirements.

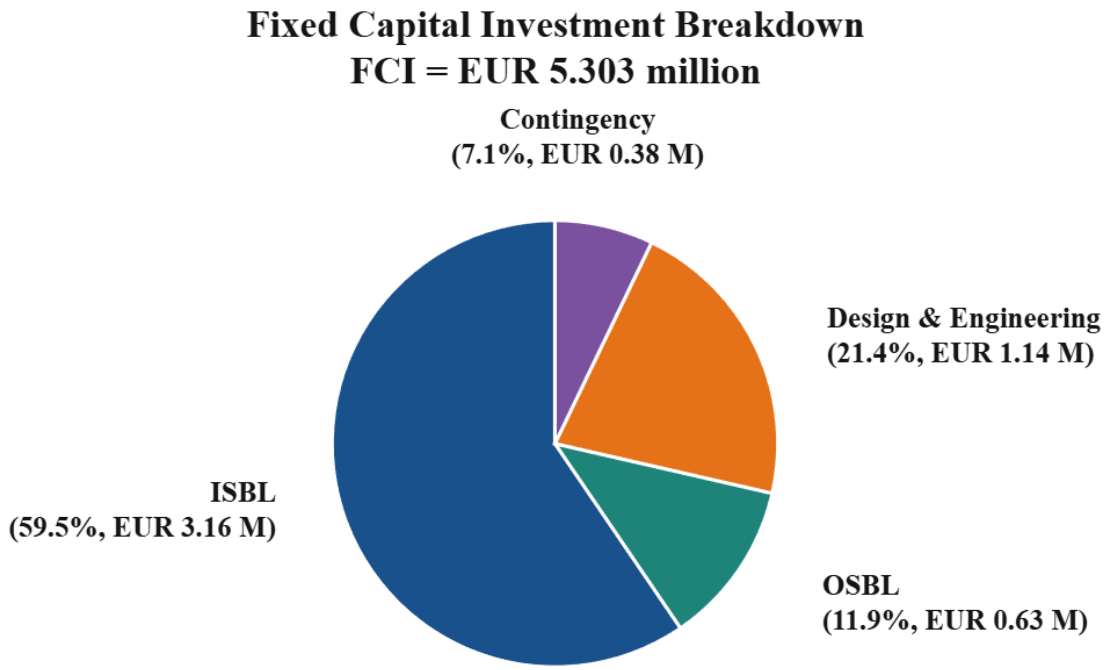

Figure 4.12: Breakdown of the fixed capital investment for the three-bed TSA hydrogen drying process.

The annual operating-cost distribution is presented in Figure 4.13. Fixed operating expenditure constitutes approximately 72.0% of the total annual OPEX, compared with 28.0% for variable operating expenditure. This result shows that, under the assumptions adopted in the present analysis, the annual economics are governed more strongly by fixed operating costs than by the direct consumption-dependent costs of the process.

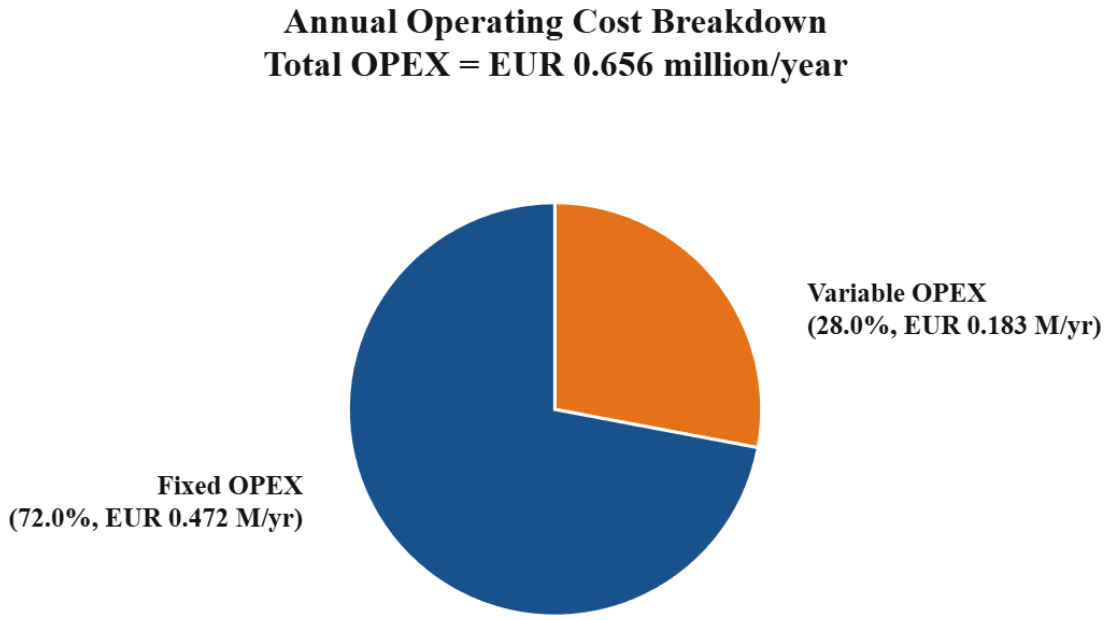

Figure 4.13: Breakdown of the annual operating expenditure for the three-bed TSA hydrogen drying process.

The relative contributions to the deterministic levelised hydrogen drying cost are shown in Figure 4.14. Capital-related costs represent the largest contribution at approximately 58.0%, equivalent to $0.684\,\mathrm{EUR\,kg_{H_2}^{-1}}$. Fixed operating expenditure contributes a further 30.2%, or $0.356\,\mathrm{EUR\,kg_{H_2}^{-1}}$, whereas variable operating expenditure contributes only 11.7%, corresponding to $0.138\,\mathrm{EUR\,kg_{H_2}^{-1}}$. Consequently, approxi-

mately 88% of the calculated drying cost originates from the annualised capital requirement and fixed operating expenditure, demonstrating that the economics of the selected TSA configuration are predominantly capital- and fixed-cost-driven rather than being dominated by direct process-energy consumption.

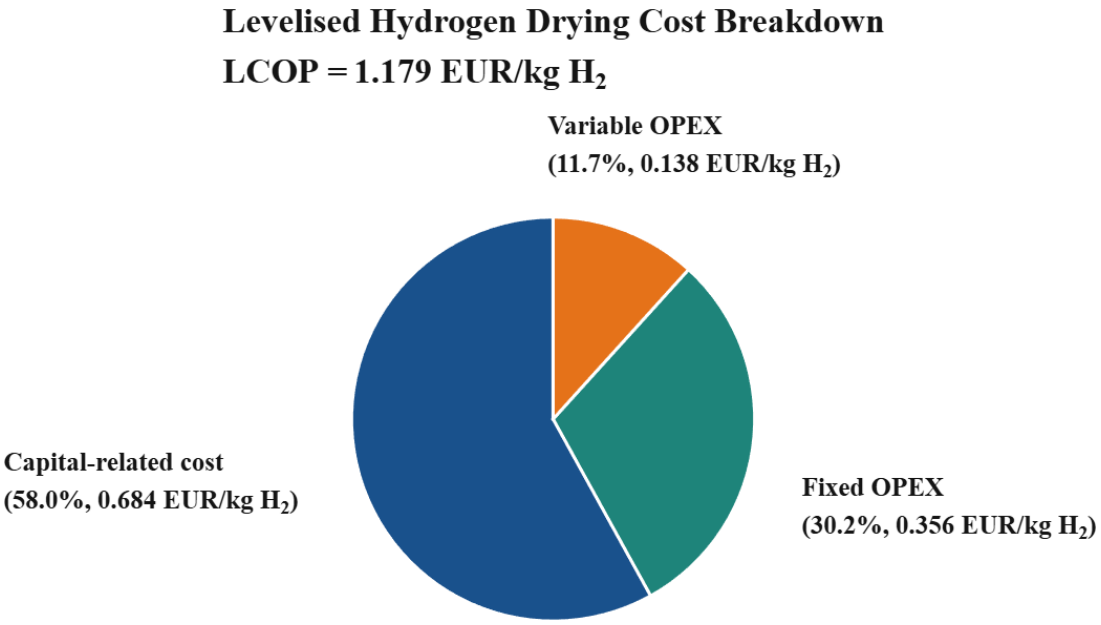

Figure 4.14: Breakdown of the deterministic levelised hydrogen drying cost for the three-bed TSA process.

The uncertainty analysis further indicates that the deterministic result should not be interpreted as a single definitive commercial cost. The Monte Carlo analysis gives a mean levelised drying cost of $1.232\ \mathrm{EUR\,kg_{H_2}^{-1}}$ and a median value of $1.211\ \mathrm{EUR\,kg_{H_2}^{-1}}$, with a central 95% uncertainty interval of $0.852 - 1.723\ \mathrm{EUR\,kg_{H_2}^{-1}}$. Capital-cost and financing assumptions, together with project lifetime and annual hydrogen throughput, therefore remain important determinants of the calculated economics.

Overall, the deterministic value of $1.179\ \mathrm{EUR\,kg_{H_2}^{-1}}$ should be interpreted as a screening-level incremental cost of hydrogen drying for the process boundary considered in this study. It is based on the selected OpenPyTEA cost correlations, installation methodology, economic assumptions and simulated hydrogen throughput, and should therefore not be interpreted as a vendor-quoted cost for a fully engineered commercial TSA installation.

4.10. Limitations of the Present Study

Several limitations should be considered when interpreting the results. First, the Aspen Adsorption model was not validated against experimental breakthrough or cyclic TSA data obtained for the same bed geometry, feed composition, pressure and regeneration conditions. The absolute breakthrough time, regeneration time and temperature profiles therefore depend on the selected equilibrium, kinetic and heat-transfer parameters.

Second, the Linear Driving Force coefficient and the gas–solid and gas–wall heat-transfer coefficients were obtained from correlations and engineering assumptions rather than being fitted to experiments for the exact Zeolite 4A pellets used in the model. These parameters influence the movement of the mass-transfer and thermal fronts and are therefore important sources of model uncertainty.

Third, continuous production was constructed from three identical beds using the timing of the single-bed cycle. The additional $4\,500\ \mathrm{s}$ standby period and the sharing of the heater and cooling-gas cooler were not simulated in one complete three-bed dynamic flowsheet. These assumptions should be checked when a fully integrated control and switching model is developed.

Fourth, the PSA/VPSA comparison was limited by numerical convergence. Deep vacuum improved

desorption, but a stable multi-cycle VPSA solution was not obtained. The present results therefore support TSA for the conditions that were successfully simulated, but they do not prove that an optimised VPSA process is physically infeasible.

Finally, the techno-economic assessment is based on the equipment-cost correlations and installation methodology available in OpenPyTEA rather than vendor quotations. The TSA vessel and compressor costing required use of the lower validity limits of their selected correlations, and the small regeneration heater was represented using a duty-based heat-exchanger cost proxy. The one-operator allocation, integrated-site OSBL assumption and non-incremental fixed-cost treatment also influence the final LCOP. The reported economic values should therefore be interpreted as screening-level estimates for comparison of cost drivers and process assumptions.

5

Overall Conclusions

Within the scope of the present study, temperature swing adsorption was the only regeneration strategy that could be demonstrated at cyclic steady state while maintaining the required hydrogen-drying performance. Pressure swing regeneration between $25\ \mathrm{bar}$ and $1\ \mathrm{bar}$ did not provide sufficient regeneration of Zeolite 4A, while deeper vacuum improved desorption but could not be demonstrated reliably over repeated cycles because of numerical convergence limitations. These VPSA results should therefore be interpreted as inconclusive rather than as evidence that vacuum regeneration is physically infeasible.

The final TSA configuration used an adsorption time of $14\,000\ \mathrm{s}$ within a $37\,500\ \mathrm{s}$ active bed cycle. Thermal regeneration reduced the water loading from approximately

$$0.0138 \quad \text{to} \quad 0.0018\ \mathrm{kmol\,kg^{-1}},$$

which provided sufficient working capacity for repeated adsorption. Cyclic steady state was achieved after 23 simulated cycles, and the product-water concentration remained below the selected $5\ \mathrm{ppmv}$ specification.

Continuous production was represented using three identical TSA beds operated in a staggered sequence. The resulting system produced approximately

$$151.3\ \mathrm{kg_{H_2}\,h^{-1}},$$

with a hydrogen recovery of

$$94.32\%.$$

The analysis also showed that the thermal behaviour of the bed is important. In particular, the temperature decrease to approximately -50 to $-55\,^{\circ}\mathrm{C}$ during blowdown should be validated experimentally because it may influence practical operation and equipment selection.

The screening-level OpenPyTEA analysis resulted in a fixed capital investment of approximately

$$5.303\ \mathrm{million\ EUR},$$

and a total annual operating expenditure of approximately

$$0.656\ \mathrm{million\ EUR\,year^{-1}}.$$

The corresponding deterministic levelized TSA drying cost was

$$1.179\ \mathrm{EUR\,kg_{H_2}^{-1}}.$$

The combined technical–economic Monte Carlo analysis gave a mean LCOP of

$$1.232\ \mathrm{EUR\,kg_{H_2}^{-1}},$$

with a median value of

$$1.211\ \mathrm{EUR\,kg_{H_2}^{-1}},$$

and a central 95% uncertainty interval of

$$0.852 - 1.723\ \mathrm{EUR\,kg_{H_2}^{-1}}.$$

The sensitivity analysis showed that the levelized drying cost was influenced most strongly by the capital-cost assumption, followed by the interest rate and project lifetime. The dry-hydrogen production rate also had an important influence because higher production distributes the capital and operating costs over a larger quantity of product. In comparison, uncertainty in regeneration energy and cycle time had a relatively small influence over the ranges investigated. The absolute economic result should therefore be regarded as a screening-level estimate and interpreted together with the assumptions used for equipment costing, financing and plant integration.

Overall, the present simulations support TSA with Zeolite 4A as a technically feasible option for deep drying of hydrogen under the investigated conditions. The most important remaining steps are experimental validation of the cyclic TSA model, further investigation of the blowdown thermal behaviour, and a better-validated comparison with optimised PSA/VPSA regeneration.

5.1. Recommendations

Experimental validation should be the highest priority for future work. Breakthrough and cyclic TSA experiments should be performed using Zeolite 4A pellets and operating conditions representative of the present model. The resulting data should be used to validate the equilibrium model and calibrate the Linear Driving Force coefficient, gas–solid heat-transfer coefficient and gas–wall heat-transfer coefficient.

The very low temperature predicted near the top of the bed during blowdown should also be investigated experimentally. Local temperature measurements during depressurisation would determine whether the simulated -50 to $-55\,^{\circ}\mathrm{C}$ excursion is realistic. If confirmed, slower blowdown, staged depressurisation or controlled heat input should be evaluated as possible methods for reducing excessive cooling and limiting the risk of local condensation or freezing.

Further work should also revisit PSA and VPSA regeneration. The pressure transition strategy, valve coefficients, vacuum level, purge conditions and solver settings should be systematically optimised, and the resulting process should be simulated to cyclic steady state before a definitive comparison with TSA is made.

For TSA regeneration, the present hot-purge approach should be compared with alternative methods such as external jacket heating or internal heating elements. The comparison should consider regeneration time, temperature uniformity, hydrogen consumption, energy demand, equipment complexity and economic performance.

The continuous three-bed arrangement should be implemented as an integrated dynamic flowsheet to confirm the assumed $4\,500\ \mathrm{s}$ standby period, heater scheduling, cooler scheduling and switching-valve logic. This would allow the proposed continuous-production concept to be tested directly rather than inferred from the single-bed cycle.

Future techno-economic work should further validate the site-specific operating-labour requirement used for the TSA section. In particular, the assumed allocation of one full-time-equivalent operator should be checked against the operating philosophy of an actual electrolyser facility, where operators, utilities and supporting infrastructure may be shared with the upstream hydrogen-production process. Vendor quotations for hydrogen-service compressors, heaters, coolers, pressure vessels and automated switching valves should also be obtained to reduce the uncertainty associated with the generic equipment-cost correlations used in the present screening-level analysis.

A

Detailed Process and Equipment Calculations

This appendix presents the detailed numerical calculations supporting the process-performance indicators and equipment-sizing results reported in the main text. The Results chapter presents only the governing equations and the principal calculated values, while the numerical substitutions and intermediate calculations are provided here for completeness.

A.1. Hydrogen Recovery Calculation

Hydrogen recovery was defined as the fraction of hydrogen supplied during the adsorption step that remained available as net product after accounting for the purified hydrogen consumed internally during regeneration heating, cooling and repressurisation:

$$R_{\mathrm{H_2}} = \frac{n_{\mathrm{H_2,feed}} - n_{\mathrm{H_2,internal}}}{n_{\mathrm{H_2,feed}}} \times 100. \tag{A.1}$$

The hydrogen supplied during one adsorption step was calculated from

$$n_{\mathrm{H_2,feed}} = \dot{n}_{\mathrm{feed}} t_{\mathrm{ads}} y_{\mathrm{H_2,feed}}. \tag{A.2}$$

The corresponding operating conditions were

$$\dot{n}_{\mathrm{feed}} = 0.0223 \ \mathrm{kmol\,s^{-1}},$$

$$t_{\mathrm{ads}} = 14\,000 \ \mathrm{s},$$

and

$$y_{\mathrm{H_2,feed}} = 0.999128.$$

Therefore,

$$n_{\mathrm{H_2,feed}} = (0.0223)(14\,000)(0.999128) \tag{A.3}$$

$$= 311.9278 \ \mathrm{kmol\,cycle^{-1}}. \tag{A.4}$$

Hydrogen Consumption During Regeneration Heating

The hydrogen consumed during the four heating stages was calculated from

$$n_{\mathrm{H_2,heating}} = \sum_j \dot{n}_{\mathrm{H_2},j} \Delta t_j. \tag{A.5}$$

For the first heating stage at $100^\circ\mathrm{C}$,

$$\begin{aligned} n_{\mathrm{H_2,h1}} &= (7.5 \times 10^{-8})(1000) && \text{(A.6)} \\ &= 7.5 \times 10^{-5}\ \mathrm{kmol}. && \text{(A.7)} \end{aligned}$$

For the second heating stage at $100^\circ\mathrm{C}$,

$$\begin{aligned} n_{\mathrm{H_2,h2}} &= (2.0 \times 10^{-4})(3000) && \text{(A.8)} \\ &= 0.6000\ \mathrm{kmol}. && \text{(A.9)} \end{aligned}$$

For the heating stage at $150^\circ\mathrm{C}$,

$$\begin{aligned} n_{\mathrm{H_2,h3}} &= (1.0 \times 10^{-3})(3000) && \text{(A.10)} \\ &= 3.0000\ \mathrm{kmol}. && \text{(A.11)} \end{aligned}$$

For the final heating stage at $175^\circ\mathrm{C}$,

$$\begin{aligned} n_{\mathrm{H_2,h4}} &= (1.0 \times 10^{-3})(8000) && \text{(A.12)} \\ &= 8.0000\ \mathrm{kmol}. && \text{(A.13)} \end{aligned}$$

The total hydrogen consumed during regeneration heating was therefore

$$\begin{aligned} n_{\mathrm{H_2,heating}} &= n_{\mathrm{H_2,h1}} + n_{\mathrm{H_2,h2}} + n_{\mathrm{H_2,h3}} + n_{\mathrm{H_2,h4}} && \text{(A.14)} \\ &= 0.000075 + 0.6000 + 3.0000 + 8.0000 && \text{(A.15)} \\ &= 11.6001\ \mathrm{kmol\,cycle^{-1}}. && \text{(A.16)} \end{aligned}$$

Hydrogen Consumption During Cooling

During the cooling step, dry hydrogen was supplied at

$$\dot{n}_{\mathrm{H_2,cooling}} = 0.002\ \mathrm{kmol\,s^{-1}}$$

for

$$\Delta t_{\mathrm{cool}} = 3000\ \mathrm{s}.$$

The corresponding hydrogen consumption was

$$\begin{aligned} n_{\mathrm{H_2,cooling}} &= \dot{n}_{\mathrm{H_2,cooling}} \Delta t_{\mathrm{cool}} && \text{(A.17)} \\ &= (0.002)(3000) && \text{(A.18)} \\ &= 6.0000\ \mathrm{kmol\,cycle^{-1}}. && \text{(A.19)} \end{aligned}$$

Hydrogen Consumption During Repressurisation

The repressurisation hydrogen flow rate was

$$\dot{n}_{\mathrm{H_2,repress}} = 5.97 \times 10^{-5}\ \mathrm{kmol\,s^{-1}},$$

and the repressurisation step lasted

$$\Delta t_{\mathrm{repress}} = 2000\ \mathrm{s}.$$

The hydrogen required for repressurisation was therefore

$$\begin{aligned} n_{\mathrm{H_2,repress}} &= \dot{n}_{\mathrm{H_2,repress}} \Delta t_{\mathrm{repress}} && \text{(A.20)} \\ &= (5.97 \times 10^{-5})(2000) && \text{(A.21)} \\ &= 0.1194\ \mathrm{kmol\,cycle^{-1}}. && \text{(A.22)} \end{aligned}$$

Total Internal Hydrogen Consumption

The total hydrogen withdrawn from the purified product stream was

$$n_{\mathrm{H_2,internal}} = n_{\mathrm{H_2,heating}} + n_{\mathrm{H_2,cooling}} + n_{\mathrm{H_2,repress}}. \tag{A.23}$$

Substitution gives

$$\begin{aligned} n_{\mathrm{H_2,internal}} &= 11.6001 + 6.0000 + 0.1194 && \text{(A.24)} \\ &= 17.7195\ \mathrm{kmol\,cycle^{-1}}. && \text{(A.25)} \end{aligned}$$

The net hydrogen available as useful product was therefore

$$\begin{aligned} n_{\mathrm{H_2,net}} &= n_{\mathrm{H_2,feed}} - n_{\mathrm{H_2,internal}} && \text{(A.26)} \\ &= 311.9278 - 17.7195 && \text{(A.27)} \\ &= 294.2083\ \mathrm{kmol\,cycle^{-1}}. && \text{(A.28)} \end{aligned}$$

Substitution into Equation A.1 gives

$$\begin{aligned} R_{\mathrm{H_2}} &= \frac{294.2083}{311.9278} \times 100 && \text{(A.29)} \\ &= 94.32\%. && \text{(A.30)} \end{aligned}$$

Hence,

$$\boxed{R_{\mathrm{H_2}} = 94.32\%}. \tag{A.31}$$

Verification Over 23 Cycles

The cumulative hydrogen supplied during the 23-cycle cyclic-steady-state simulation was

$$n_{\mathrm{H_2,feed},23} = 23(311.9278) \tag{A.32}$$
$$= 7174.34\ \mathrm{kmol}. \tag{A.33}$$

The cumulative internal hydrogen consumption was

$$n_{\mathrm{H_2,internal},23} = 23(17.7195) \tag{A.34}$$
$$= 407.55\ \mathrm{kmol}. \tag{A.35}$$

The cumulative net hydrogen product was therefore

$$n_{\mathrm{H_2,net},23} = 7174.34 - 407.55 \tag{A.36}$$
$$= 6766.79\ \mathrm{kmol}. \tag{A.37}$$

The cumulative recovery was consequently

$$R_{\mathrm{H_2}} = \frac{6766.79}{7174.34} \times 100 \tag{A.38}$$
$$= 94.32\%. \tag{A.39}$$

The identical recovery obtained from the single-cycle and cumulative calculations confirms the consistency of the adopted hydrogen balance. The calculation assumes that hydrogen used for heating, cooling and repressurisation is withdrawn from the purified product stream and is therefore unavailable as net dry-hydrogen product.

A.2. Hydrogen Productivity Calculation

The gross hydrogen production associated with one adsorption step was

$$n_{\mathrm{H_2,gross}} = 311.9278\ \mathrm{kmol\,cycle^{-1}}.$$

Using a rounded hydrogen molecular weight of

$$M_{\mathrm{H_2}} = 2\ \mathrm{kg\,kmol^{-1}},$$

the corresponding gross hydrogen mass produced per cycle was

$$m_{\mathrm{H_2,gross}} = n_{\mathrm{H_2,gross}} M_{\mathrm{H_2}} \tag{A.40}$$
$$= 311.9278(2) \tag{A.41}$$
$$= 623.86\ \mathrm{kg\,cycle^{-1}}. \tag{A.42}$$

The hydrogen used internally for regeneration heating, cooling and repressurisation was

$$n_{\mathrm{H_2,internal}} = 17.7195\ \mathrm{kmol\,cycle^{-1}}.$$

The equivalent internal hydrogen mass was therefore

$$m_{\mathrm{H_2,internal}} = n_{\mathrm{H_2,internal}} M_{\mathrm{H_2}} \tag{A.43}$$
$$= 17.7195(2) \tag{A.44}$$
$$= 35.44\ \mathrm{kg\,cycle^{-1}}. \tag{A.45}$$

The net hydrogen production per completed adsorption-production interval was

$$m_{\mathrm{H_2,net}} = m_{\mathrm{H_2,gross}} - m_{\mathrm{H_2,internal}} \tag{A.46}$$
$$= 623.86 - 35.44 \tag{A.47}$$
$$= 588.42\ \mathrm{kg\,cycle^{-1}}. \tag{A.48}$$

Thus,

$$\boxed{m_{\mathrm{H_2,net}} = 588.42\ \mathrm{kg\,cycle^{-1}}}. \tag{A.49}$$

Continuous Plant Hydrogen-Production Rate

In the staggered three-bed configuration, a new adsorption-production interval was completed every

$$t_{\mathrm{slot}} = 14\,000\ \mathrm{s}.$$

Expressed in hours,

$$t_{\mathrm{slot}} = \frac{14\,000}{3600} \tag{A.50}$$
$$= 3.8889\ \mathrm{h}. \tag{A.51}$$

The average net hydrogen-production rate of the complete three-bed plant was therefore

$$\dot{m}_{\mathrm{H_2,plant}} = \frac{m_{\mathrm{H_2,net}}}{t_{\mathrm{slot}}} \tag{A.52}$$
$$= \frac{588.42}{3.8889} \tag{A.53}$$
$$= 151.3\ \mathrm{kg\,h^{-1}}. \tag{A.54}$$

Hence,

$$\boxed{\dot{m}_{\mathrm{H_2,plant}} = 151.3\ \mathrm{kg\,h^{-1}}}. \tag{A.55}$$

Total Adsorbent Inventory

Each TSA bed contained approximately

$$m_{\mathrm{ads,bed}} = 28\ \mathrm{kg}$$

of Zeolite 4A.

For three adsorption beds, the total adsorbent inventory was

$$m_{\mathrm{ads,total}} = 3m_{\mathrm{ads,bed}} \tag{A.56}$$
$$= 3(28) \tag{A.57}$$
$$= 84\ \mathrm{kg}. \tag{A.58}$$

Continuous-Plant Adsorbent Productivity

The continuous-plant hydrogen productivity was defined as the net hydrogen production rate divided by the total adsorbent inventory:

$$\Pi_{\mathrm{H_2,plant}} = \frac{\dot{m}_{\mathrm{H_2,plant}}}{m_{\mathrm{ads,total}}}. \tag{A.59}$$

Substitution gives

$$\Pi_{\mathrm{H_2,plant}} = \frac{151.3}{84} \tag{A.60}$$
$$= 1.80\ \mathrm{kg_{H_2}\,kg_{ads}^{-1}\,h^{-1}}. \tag{A.61}$$

Therefore,

$$\boxed{\Pi_{\mathrm{H_2,plant}} = 1.80\ \mathrm{kg_{H_2}\,kg_{ads}^{-1}\,h^{-1}}}. \tag{A.62}$$

This productivity is based on the complete three-bed adsorbent inventory and the staggered $14\,000\ \mathrm{s}$ adsorption-production interval. It therefore represents the continuous-plant productivity rather than the productivity of an individual adsorption bed considered in isolation.

A.3. Regeneration-Hydrogen Heating Calculation

During regeneration, a portion of the purified hydrogen product was heated and introduced counter-currently through the adsorption bed. The heating sequence consisted of two stages at $100^{\circ}\mathrm{C}$, followed by stages at $150^{\circ}\mathrm{C}$ and $175^{\circ}\mathrm{C}$.

Hydrogen Enthalpy Change

The temperature-dependent enthalpy of hydrogen was calculated using the Shomate equation from the NIST Chemistry WebBook [77]:

$$H^{\circ}(T) - H^{\circ}_{298.15} = At + \frac{Bt^2}{2} + \frac{Ct^3}{3} + \frac{Dt^4}{4} - \frac{E}{t} + F - H, \tag{A.63}$$

where

$$t = \frac{T}{1000}.$$

The enthalpy change relative to $298.15\ \mathrm{K}$ was therefore evaluated as

$$\Delta h_{25\to T} = H^{\circ}(T) - H^{\circ}(298.15). \tag{A.64}$$

The calculated enthalpy differences were

$$\Delta h_{25\to 100} = 2176.06\ \mathrm{kJ\,kmol^{-1}},$$

$$\Delta h_{25\to150} = 3634.89\ \mathrm{kJ\,kmol^{-1}},$$

and

$$\Delta h_{25\to175} = 4365.41\ \mathrm{kJ\,kmol^{-1}}.$$

Heating-Stage Thermal Duties

The thermal duty during each regeneration-heating stage was calculated from

$$\dot{Q}_j = \dot{n}_{\mathrm{H_2},j}\Delta h_j, \tag{A.65}$$

and the corresponding energy supplied during the stage was obtained from

$$E_j = \dot{Q}_j \Delta t_j. \tag{A.66}$$

Since

$$\left(\mathrm{kmol\,s^{-1}}\right)\left(\mathrm{kJ\,kmol^{-1}}\right) = \mathrm{kW},$$

Equation A.65 gives the thermal duty directly in kilowatts.

First Heating Stage at $100^\circ\mathrm{C}$

For the first heating stage,

$$\dot{n}_{\mathrm{H_2},1} = 7.5\times10^{-8}\ \mathrm{kmol\,s^{-1}},$$

and

$$\Delta t_1 = 1000\ \mathrm{s}.$$

The corresponding thermal duty was

$$\begin{aligned}
\dot{Q}_1 &= \dot{n}_{\mathrm{H_2},1}\Delta h_{25\to100} && \text{(A.67)}\\
&= (7.5\times10^{-8})(2176.06) && \text{(A.68)}\\
&= 1.63\times10^{-4}\ \mathrm{kW}. && \text{(A.69)}
\end{aligned}$$

The energy supplied during the stage was

$$\begin{aligned}
E_1 &= \dot{Q}_1\Delta t_1 && \text{(A.70)}\\
&= (1.63\times10^{-4})(1000) && \text{(A.71)}\\
&= 0.163\ \mathrm{kJ}. && \text{(A.72)}
\end{aligned}$$

Converting to kilowatt-hours,

$$\begin{aligned}
E_1 &= \frac{0.163}{3600} && \text{(A.73)}\\
&= 4.53\times10^{-5}\ \mathrm{kWh}. && \text{(A.74)}
\end{aligned}$$

Second Heating Stage at $100°\mathrm{C}$

For the second heating stage,

$$\dot{n}_{\mathrm{H_2},2} = 2.0 \times 10^{-4}\ \mathrm{kmol\,s^{-1}},$$

and

$$\Delta t_2 = 3000\ \mathrm{s}.$$

The thermal duty was

$$\begin{aligned} \dot{Q}_2 &= (2.0 \times 10^{-4})(2176.06) && \text{(A.75)} \\ &= 0.435\ \mathrm{kW}. && \text{(A.76)} \end{aligned}$$

The corresponding energy requirement was

$$\begin{aligned} E_2 &= (0.435)(3000) && \text{(A.77)} \\ &= 1305.64\ \mathrm{kJ} && \text{(A.78)} \\ &= 0.363\ \mathrm{kWh}. && \text{(A.79)} \end{aligned}$$

Heating Stage at $150°\mathrm{C}$

For the $150°\mathrm{C}$ heating stage,

$$\dot{n}_{\mathrm{H_2},3} = 1.0 \times 10^{-3}\ \mathrm{kmol\,s^{-1}},$$

and

$$\Delta t_3 = 3000\ \mathrm{s}.$$

The corresponding thermal duty was

$$\begin{aligned} \dot{Q}_3 &= (1.0 \times 10^{-3})(3634.89) && \text{(A.80)} \\ &= 3.635\ \mathrm{kW}. && \text{(A.81)} \end{aligned}$$

The thermal energy supplied was

$$\begin{aligned} E_3 &= (3.635)(3000) && \text{(A.82)} \\ &= 10\,904.67\ \mathrm{kJ} && \text{(A.83)} \\ &= 3.029\ \mathrm{kWh}. && \text{(A.84)} \end{aligned}$$

Heating Stage at $175^{\circ}\mathrm{C}$

For the final heating stage,

$$\dot{n}_{\mathrm{H_2},4} = 1.0 \times 10^{-3}\ \mathrm{kmol\,s^{-1}},$$

and

$$\Delta t_4 = 8000\ \mathrm{s}.$$

The thermal duty was

$$\begin{aligned} \dot{Q}_4 &= (1.0 \times 10^{-3})(4365.41) && \text{(A.85)} \\ &= 4.365\ \mathrm{kW}. && \text{(A.86)} \end{aligned}$$

The corresponding energy requirement was

$$\begin{aligned} E_4 &= (4.365)(8000) && \text{(A.87)} \\ &= 34\,923.28\ \mathrm{kJ} && \text{(A.88)} \\ &= 9.701\ \mathrm{kWh}. && \text{(A.89)} \end{aligned}$$

Total Regeneration-Hydrogen Heating Energy

The total sensible energy supplied to the regeneration hydrogen during one heating sequence was

$$E_{\mathrm{thermal,cycle}} = E_1 + E_2 + E_3 + E_4. \tag{A.90}$$

Therefore,

$$\begin{aligned} E_{\mathrm{thermal,cycle}} &= 0.000045 + 0.363 + 3.029 + 9.701 && \text{(A.91)} \\ &= 13.093\ \mathrm{kWh\,cycle^{-1}}. && \text{(A.92)} \end{aligned}$$

Converting to megajoules,

$$\begin{aligned} E_{\mathrm{thermal,cycle}} &= 13.093(3.6) && \text{(A.93)} \\ &= 47.13\ \mathrm{MJ\,cycle^{-1}}. && \text{(A.94)} \end{aligned}$$

Hence,

$$\boxed{E_{\mathrm{thermal,cycle}} = 47.13\ \mathrm{MJ\,cycle^{-1}}}. \tag{A.95}$$

Electrical Heater Requirement

For an assumed heater efficiency of

$$\eta_{\text{heater}} = 0.90,$$

the electrical energy supplied to the heater was calculated from

$$E_{\text{electrical,cycle}} = \frac{E_{\text{thermal,cycle}}}{\eta_{\text{heater}}}. \tag{A.96}$$

Thus,

$$E_{\text{electrical,cycle}} = \frac{13.093}{0.90} \tag{A.97}$$

$$= 14.55\ \text{kWh}\,\text{cycle}^{-1}. \tag{A.98}$$

Equivalently,

$$E_{\text{electrical,cycle}} = 52.37\ \text{MJ}\,\text{cycle}^{-1}.$$

Heater Capacity

The maximum instantaneous thermal duty occurred during the final 175°C heating stage:

$$\dot{Q}_{\text{thermal,max}} = 4.365\ \text{kW}.$$

Accounting for heater efficiency, the maximum electrical input requirement was

$$\dot{W}_{\text{heater,max}} = \frac{\dot{Q}_{\text{thermal,max}}}{\eta_{\text{heater}}} \tag{A.99}$$

$$= \frac{4.365}{0.90} \tag{A.100}$$

$$= 4.85\ \text{kW}. \tag{A.101}$$

A design factor of 1.20 was then applied:

$$\dot{W}_{\text{heater,design}} = 1.20\dot{W}_{\text{heater,max}} \tag{A.102}$$

$$= 1.20(4.85) \tag{A.103}$$

$$= 5.82\ \text{kW}. \tag{A.104}$$

A nominal heater capacity of

$$\boxed{\dot{W}_{\text{heater,selected}} \approx 6\ \text{kW}} \tag{A.105}$$

was therefore selected.

The calculated $47.13\ \text{MJ}\,\text{cycle}^{-1}$ represents the sensible enthalpy supplied to the regeneration hydrogen. It is not added independently to the theoretical bed-regeneration energy because the heat transferred from the regeneration gas provides the energy required to heat the adsorbent and vessel and to desorb water from the bed.

A.4. Bed-Regeneration Energy Calculation

In addition to heating the regeneration hydrogen, thermal energy is required within the adsorber to heat the Zeolite 4A, overcome the heat associated with water desorption, and heat the steel vessel wall. The theoretical bed-regeneration energy was estimated as

$$Q_{\mathrm{regen,bed}} = Q_{\mathrm{zeolite}} + Q_{\mathrm{desorption}} + Q_{\mathrm{wall}}. \tag{A.106}$$

The calculation was performed for one TSA bed and one regeneration cycle.

Adsorbent Inventory

The internal packed-bed volume was calculated from

$$V_{\mathrm{bed}} = \frac{\pi D_i^2}{4} L, \tag{A.107}$$

where

$$D_i = 0.25\ \mathrm{m},$$

and

$$L = 0.75\ \mathrm{m}.$$

Therefore,

$$V_{\mathrm{bed}} = \frac{\pi(0.25)^2}{4}(0.75) \tag{A.108}$$

$$= 0.03682\ \mathrm{m}^3. \tag{A.109}$$

Using a Zeolite 4A bulk density of

$$\rho_{\mathrm{bulk}} = 760\ \mathrm{kg\,m^{-3}},$$

the adsorbent mass contained in one bed was

$$m_{\mathrm{ads}} = \rho_{\mathrm{bulk}} V_{\mathrm{bed}} \tag{A.110}$$

$$= 760(0.03682) \tag{A.111}$$

$$= 27.98\ \mathrm{kg}. \tag{A.112}$$

For subsequent calculations, the adsorbent inventory was therefore taken as approximately

$$m_{\mathrm{ads}} \approx 28\ \mathrm{kg\,bed^{-1}}.$$

Sensible Heating of Zeolite 4A

The sensible heat required to increase the temperature of the adsorbent was calculated from

$$Q_{\text{zeolite}} = m_{\text{ads}} C_{p,\text{ads}} \Delta T. \tag{A.113}$$

The initial bed temperature was approximately

$$T_{\text{initial}} = 25^{\circ}\text{C},$$

while the representative temperature at the end of the heating step was

$$T_{\text{final}} \approx 170^{\circ}\text{C}.$$

The corresponding temperature increase was

$$\begin{aligned} \Delta T &= T_{\text{final}} - T_{\text{initial}} && \text{(A.114)} \\ &= 170 - 25 && \text{(A.115)} \\ &= 145 \text{ K}. && \text{(A.116)} \end{aligned}$$

Using a Zeolite 4A heat capacity of

$$C_{p,\text{ads}} = 900 \text{ J}\,\text{kg}^{-1}\,\text{K}^{-1},$$

the sensible heat required to heat the adsorbent was

$$\begin{aligned} Q_{\text{zeolite}} &= (27.98)(900)(145) && \text{(A.117)} \\ &= 3.65 \times 10^{6} \text{ J} && \text{(A.118)} \\ &= 3.65 \text{ MJ}\,\text{cycle}^{-1}. && \text{(A.119)} \end{aligned}$$

Heat Required for Water Desorption

The working adsorption capacity was estimated from the difference between the water loading at the end of adsorption and the residual loading following regeneration:

$$\Delta q = q_{\text{end,ads}} - q_{\text{end,regen}}. \tag{A.120}$$

Using

$$q_{\text{end,ads}} = 0.0138 \text{ kmol}\,\text{kg}^{-1},$$

and

$$q_{\text{end,regen}} = 0.0018 \text{ kmol}\,\text{kg}^{-1},$$

the working capacity was

$$\begin{aligned} \Delta q &= 0.0138 - 0.0018 && \text{(A.121)} \\ &= 0.0120 \text{ kmol}\,\text{kg}^{-1}. && \text{(A.122)} \end{aligned}$$

The amount of water desorbed from one bed during regeneration was calculated from

$$n_{\mathrm{H_2O,des}} = m_{\mathrm{ads}} \Delta q. \tag{A.123}$$

Therefore,

$$\begin{aligned} n_{\mathrm{H_2O,des}} &= 27.98(0.0120) && \text{(A.124)} \\ &= 0.3358 \ \mathrm{kmol\,cycle^{-1}}. && \text{(A.125)} \end{aligned}$$

Using a water molecular weight of

$$M_{\mathrm{H_2O}} = 18 \ \mathrm{kg\,kmol^{-1}},$$

the corresponding mass of water removed was

$$\begin{aligned} m_{\mathrm{H_2O,des}} &= n_{\mathrm{H_2O,des}} M_{\mathrm{H_2O}} && \text{(A.126)} \\ &= 0.3358(18) && \text{(A.127)} \\ &= 6.04 \ \mathrm{kg\,cycle^{-1}}. && \text{(A.128)} \end{aligned}$$

Using a heat of adsorption magnitude of

$$|\Delta H_{\mathrm{ads}}| = 59 \ \mathrm{MJ\,kmol^{-1}},$$

the corresponding desorption-energy requirement was estimated from

$$Q_{\mathrm{desorption}} = n_{\mathrm{H_2O,des}} \left|\Delta H_{\mathrm{ads}}\right|. \tag{A.129}$$

Thus,

$$\begin{aligned} Q_{\mathrm{desorption}} &= 0.3358(59) && \text{(A.130)} \\ &= 19.81 \ \mathrm{MJ\,cycle^{-1}}. && \text{(A.131)} \end{aligned}$$

Sensible Heating of the Vessel Wall

The TSA vessel was represented as a cylindrical steel shell having an internal diameter of

$$D_i = 0.25 \ \mathrm{m}$$

and a wall thickness of

$$\delta = 0.005 \ \mathrm{m}.$$

The corresponding outer diameter was

$$\begin{aligned} D_o &= D_i + 2\delta && \text{(A.132)} \\ &= 0.25 + 2(0.005) && \text{(A.133)} \\ &= 0.26 \ \mathrm{m}. && \text{(A.134)} \end{aligned}$$

The cylindrical shell volume was calculated from

$$V_{\mathrm{wall}} = \frac{\pi}{4}\left(D_o^2 - D_i^2\right) L. \tag{A.135}$$

Therefore,

$$V_{\mathrm{wall}} = \frac{\pi}{4}\left[(0.26)^2 - (0.25)^2\right](0.75) \tag{A.136}$$

$$= 3.00 \times 10^{-3}\ \mathrm{m}^3. \tag{A.137}$$

Using a steel density of

$$\rho_{\mathrm{steel}} = 7900\ \mathrm{kg\,m^{-3}},$$

the cylindrical vessel-wall mass was

$$m_{\mathrm{wall}} = \rho_{\mathrm{steel}} V_{\mathrm{wall}} \tag{A.138}$$

$$= 7900(3.00 \times 10^{-3}) \tag{A.139}$$

$$= 23.73\ \mathrm{kg}. \tag{A.140}$$

The sensible heat required to heat the vessel wall was calculated from

$$Q_{\mathrm{wall}} = m_{\mathrm{wall}} C_{p,\mathrm{steel}} \Delta T. \tag{A.141}$$

Using

$$C_{p,\mathrm{steel}} = 500\ \mathrm{J\,kg^{-1}\,K^{-1}},$$

and

$$\Delta T = 145\ \mathrm{K},$$

the vessel-wall heating requirement was

$$Q_{\mathrm{wall}} = (23.73)(500)(145) \tag{A.142}$$

$$= 1.72 \times 10^6\ \mathrm{J} \tag{A.143}$$

$$= 1.72\ \mathrm{MJ\,cycle^{-1}}. \tag{A.144}$$

Total Theoretical Bed-Regeneration Energy

The total theoretical thermal requirement was obtained by summing the adsorbent sensible heat, water-desorption energy, and vessel-wall sensible heat:

$$Q_{\mathrm{regen,bed}} = Q_{\mathrm{zeolite}} + Q_{\mathrm{desorption}} + Q_{\mathrm{wall}} \tag{A.145}$$

$$= 3.65 + 19.81 + 1.72 \tag{A.146}$$

$$= 25.18\ \mathrm{MJ\,cycle^{-1}}. \tag{A.147}$$

Therefore,

$$\boxed{Q_{\mathrm{regen,bed}} = 25.18\ \mathrm{MJ\,cycle^{-1}\,bed^{-1}} \approx 25.2\ \mathrm{MJ\,cycle^{-1}\,bed^{-1}}}. \tag{A.148}$$

The calculated regeneration-gas heating requirement of $47.13\,\mathrm{MJ\,cycle^{-1}}$ and the theoretical bed-regeneration demand of $25.18\ \mathrm{MJ\,cycle^{-1}\,bed^{-1}}$ represent different energy quantities and are not added together. The former represents the sensible enthalpy supplied to the regeneration hydrogen, while the latter estimates the thermal demand within the adsorber that is supplied through heat transfer from the hot regeneration gas.

A.5. Cooling-Duty Calculation

Following regeneration, the adsorption bed was cooled using dry hydrogen before repressurisation and the start of the subsequent adsorption step. The cooling requirement was estimated from the sensible heat removed from the Zeolite 4A and the cylindrical steel vessel wall.

The total cooling-energy requirement was calculated from

$$Q_{\mathrm{cool,total}} = Q_{\mathrm{cool,ads}} + Q_{\mathrm{cool,wall}}. \tag{A.149}$$

Temperature Difference

At the end of the heating step, the representative bed temperature was approximately

$$T_{\mathrm{hot}} = 169^{\circ}\mathrm{C}.$$

Following cooling, the bed temperature decreased to approximately

$$T_{\mathrm{cold}} = 298.482\ \mathrm{K} \approx 25^{\circ}\mathrm{C}.$$

The temperature difference used in the cooling calculation was therefore

$$\begin{aligned} \Delta T &= T_{\mathrm{hot}} - T_{\mathrm{cold}} && \text{(A.150)}\\ &\approx 169 - 25 && \text{(A.151)}\\ &= 144\ \mathrm{K}. && \text{(A.152)} \end{aligned}$$

Heat Removed from Zeolite 4A

The sensible heat removed from the adsorbent was calculated from

$$Q_{\mathrm{cool,ads}} = m_{\mathrm{ads}} C_{p,\mathrm{ads}} \Delta T. \tag{A.153}$$

Using

$$m_{\mathrm{ads}} = 27.98\ \mathrm{kg},$$

$$C_{p,\mathrm{ads}} = 900\ \mathrm{J\,kg^{-1}\,K^{-1}},$$

and

$$\Delta T = 144\ \mathrm{K},$$

the cooling energy associated with the adsorbent was

$$Q_{\mathrm{cool,ads}} = (27.98)(900)(144) \tag{A.154}$$
$$= 3.63 \times 10^{6}\ \mathrm{J} \tag{A.155}$$
$$= 3.63\ \mathrm{MJ\,cycle^{-1}}. \tag{A.156}$$

Converting to kilowatt-hours,

$$Q_{\mathrm{cool,ads}} = \frac{3.63}{3.6} \tag{A.157}$$
$$= 1.01\ \mathrm{kWh\,cycle^{-1}}. \tag{A.158}$$

Heat Removed from the Vessel Wall

The sensible heat removed from the cylindrical steel vessel wall was calculated from

$$Q_{\mathrm{cool,wall}} = m_{\mathrm{wall}} C_{p,\mathrm{steel}} \Delta T. \tag{A.159}$$

Using the previously calculated vessel-wall mass,

$$m_{\mathrm{wall}} = 23.73\ \mathrm{kg},$$

together with

$$C_{p,\mathrm{steel}} = 500\ \mathrm{J\,kg^{-1}\,K^{-1}},$$

the vessel-wall cooling requirement was

$$Q_{\mathrm{cool,wall}} = (23.73)(500)(144) \tag{A.160}$$
$$= 1.71 \times 10^{6}\ \mathrm{J} \tag{A.161}$$
$$= 1.71\ \mathrm{MJ\,cycle^{-1}}. \tag{A.162}$$

In kilowatt-hours,

$$Q_{\mathrm{cool,wall}} = \frac{1.71}{3.6} \tag{A.163}$$
$$= 0.47\ \mathrm{kWh\,cycle^{-1}}. \tag{A.164}$$

Total Cooling Energy

The total sensible heat removed from one TSA bed was therefore

$$Q_{\mathrm{cool,total}} = Q_{\mathrm{cool,ads}} + Q_{\mathrm{cool,wall}} \tag{A.165}$$
$$= 3.63 + 1.71 \tag{A.166}$$
$$= 5.34\ \mathrm{MJ\,cycle^{-1}}. \tag{A.167}$$

Equivalently,

$$Q_{\mathrm{cool,total}} = \frac{5.34}{3.6} \tag{A.168}$$
$$= 1.48\ \mathrm{kWh\,cycle^{-1}}. \tag{A.169}$$

Thus,

$$\boxed{Q_{\mathrm{cool,total}} = 5.34\ \mathrm{MJ\,cycle^{-1}\,bed^{-1}}}. \tag{A.170}$$

Average Cooling Duty

The cooling step had a duration of

$$\Delta t_{\mathrm{cool}} = 3000\ \mathrm{s}.$$

The average cooling duty was calculated from

$$\dot{Q}_{\mathrm{cool}} = \frac{Q_{\mathrm{cool,total}}}{\Delta t_{\mathrm{cool}}}. \tag{A.171}$$

Substitution gives

$$\dot{Q}_{\mathrm{cool}} = \frac{5.34 \times 10^3\ \mathrm{kJ}}{3000\ \mathrm{s}} \tag{A.172}$$
$$= 1.78\ \mathrm{kJ\,s^{-1}} \tag{A.173}$$
$$= 1.78\ \mathrm{kW}. \tag{A.174}$$

Selected Cooling Capacity

A design factor of 1.20 was applied to account for operating variations, heat-transfer limitations and additional thermal loads:

$$\dot{Q}_{\mathrm{cool,design}} = 1.20\dot{Q}_{\mathrm{cool}} \tag{A.175}$$
$$= 1.20(1.78) \tag{A.176}$$
$$= 2.14\ \mathrm{kW}. \tag{A.177}$$

A nominal cooling-gas cooler capacity of

$$\boxed{\dot{Q}_{\mathrm{cool,selected}} = 2.5\ \mathrm{kW}} \tag{A.178}$$

was therefore selected.

The calculation includes the sensible heat removed from the Zeolite 4A and the cylindrical portion of the steel vessel wall. Thermal contributions from the vessel heads, piping, insulation and heat exchange with the surroundings were not explicitly included.

A.6. Hydrogen Compressor Calculation

The wet-hydrogen feed from the electrolyser was compressed from $10\ \mathrm{bar}$ to the TSA adsorption pressure of $25\ \mathrm{bar}$. The compressor sizing calculation was based on the following operating conditions:

$$P_1 = 10\ \mathrm{bar}, \qquad P_2 = 25\ \mathrm{bar},$$

$$T_1 = 298\ \mathrm{K}, \qquad \dot{n}_{\mathrm{feed}} = 0.0223\ \mathrm{kmol\,s^{-1}}.$$

The pressure ratio was therefore

$$r_p = \frac{P_2}{P_1} \tag{A.179}$$
$$= \frac{25}{10} \tag{A.180}$$
$$= 2.5. \tag{A.181}$$

The compression was approximated as adiabatic compression of an ideal gas with a hydrogen heat-capacity ratio of

$$k = 1.4.$$

Isentropic Outlet Temperature

The isentropic compressor-outlet temperature was calculated from

$$\frac{T_{2,s}}{T_1} = \left(\frac{P_2}{P_1}\right)^{(k-1)/k}. \tag{A.182}$$

Substitution gives

$$T_{2,s} = 298\,(2.5)^{(1.4-1)/1.4} \tag{A.183}$$
$$= 387.2\ \mathrm{K}. \tag{A.184}$$

The corresponding isentropic temperature increase was

$$\Delta T_s = T_{2,s} - T_1 \tag{A.185}$$
$$= 387.2 - 298 \tag{A.186}$$
$$= 89.2\ \mathrm{K}. \tag{A.187}$$

Isentropic Compressor Power

Using a representative hydrogen molar heat capacity of

$$C_{p,\mathrm{H_2}} = 29\ \mathrm{kJ\,kmol^{-1}\,K^{-1}},$$

the isentropic enthalpy increase was estimated from

$$\Delta h_s = C_{p,\mathrm{H_2}}\,(T_{2,s} - T_1)\,. \tag{A.188}$$

Therefore,

$$\Delta h_s = 29(89.2) \tag{A.189}$$
$$= 2586 \text{ kJ kmol}^{-1}. \tag{A.190}$$

The corresponding isentropic compressor power was

$$\dot{W}_s = \dot{n}_{\text{feed}} \Delta h_s. \tag{A.191}$$

Thus,

$$\dot{W}_s = 0.0223(2586) \tag{A.192}$$
$$= 57.7 \text{ kW}. \tag{A.193}$$

Required Compressor Shaft Power

An isentropic compressor efficiency of

$$\eta_s = 0.75$$

was assumed.

The actual specific enthalpy increase was calculated from

$$\Delta h_{\text{actual}} = \frac{\Delta h_s}{\eta_s}. \tag{A.194}$$

Hence,

$$\Delta h_{\text{actual}} = \frac{2586}{0.75} \tag{A.195}$$
$$= 3448 \text{ kJ kmol}^{-1}. \tag{A.196}$$

The required compressor shaft power was therefore

$$\dot{W}_{\text{shaft}} = \dot{n}_{\text{feed}} \Delta h_{\text{actual}}. \tag{A.197}$$

Substitution gives

$$\dot{W}_{\text{shaft}} = 0.0223(3448) \tag{A.198}$$
$$= 76.9 \text{ kW}. \tag{A.199}$$

Thus,

$$\boxed{\dot{W}_{\text{shaft}} = 76.9 \text{ kW}}. \tag{A.200}$$

Compressor Electrical Input

Assuming a motor efficiency of

$$\eta_{\text{motor}} = 0.95,$$

the compressor electrical input was calculated from

$$\dot{W}_{\text{electric}} = \frac{\dot{W}_{\text{shaft}}}{\eta_{\text{motor}}}. \tag{A.201}$$

Therefore,

$$\dot{W}_{\text{electric}} = \frac{76.9}{0.95} \tag{A.202}$$

$$= 80.9 \text{ kW}. \tag{A.203}$$

Hence,

$$\boxed{\dot{W}_{\text{electric}} = 80.9 \text{ kW}}. \tag{A.204}$$

A design factor of 1.10 was applied to the required electrical power:

$$\dot{W}_{\text{motor,design}} = 1.10\dot{W}_{\text{electric}} \tag{A.205}$$

$$= 1.10(80.9) \tag{A.206}$$

$$= 89.0 \text{ kW}. \tag{A.207}$$

A nominal compressor-motor rating of

$$\boxed{\dot{W}_{\text{motor,selected}} \approx 90 \text{ kW}} \tag{A.208}$$

was therefore selected.

Actual Compressor Outlet Temperature

The compressor isentropic efficiency can also be expressed as

$$\eta_s = \frac{T_{2,s} - T_1}{T_{2,\text{actual}} - T_1}. \tag{A.209}$$

Rearranging gives

$$T_{2,\text{actual}} = T_1 + \frac{T_{2,s} - T_1}{\eta_s}. \tag{A.210}$$

Therefore,

$$T_{2,\text{actual}} = 298 + \frac{387.2 - 298}{0.75} \tag{A.211}$$

$$= 416.9 \text{ K}. \tag{A.212}$$

Converting to degrees Celsius,

$$T_{2,\mathrm{actual}} \approx 143.8^{\circ}\mathrm{C}.$$

Thus,

$$\boxed{T_{2,\mathrm{actual}} \approx 417\ \mathrm{K} \approx 144^{\circ}\mathrm{C}}. \tag{A.213}$$

The compressor shaft power of $76.9\ \mathrm{kW}$ was used as the equipment sizing parameter in the OpenPyTEA compressor-cost correlation, whereas the electrical input of $80.9\ \mathrm{kW}$ was used for electricity-consumption and operating-cost calculations.

A.7. Compressor Aftercooler Calculation

Compression increased the hydrogen temperature from approximately $25^{\circ}\mathrm{C}$ to $144^{\circ}\mathrm{C}$. An aftercooler was therefore required to reduce the compressed hydrogen temperature back to the TSA adsorption temperature of approximately $25^{\circ}\mathrm{C}$.

The aftercooler duty was calculated from

$$\dot{Q}_{\mathrm{AC}} = \dot{n}_{\mathrm{feed}} C_{p,\mathrm{H_2}} \left(T_{2,\mathrm{actual}} - T_{\mathrm{AC,out}}\right). \tag{A.214}$$

The corresponding operating conditions were

$$\dot{n}_{\mathrm{feed}} = 0.0223\ \mathrm{kmol\,s^{-1}},$$

$$C_{p,\mathrm{H_2}} = 29\ \mathrm{kJ\,kmol^{-1}\,K^{-1}},$$

$$T_{2,\mathrm{actual}} = 416.9\ \mathrm{K},$$

and

$$T_{\mathrm{AC,out}} = 298\ \mathrm{K}.$$

The enthalpy removed from the hydrogen during cooling was therefore

$$\begin{aligned} \Delta h_{\mathrm{AC}} &= C_{p,\mathrm{H_2}} \left(T_{2,\mathrm{actual}} - T_{\mathrm{AC,out}}\right) && \text{(A.215)} \\ &= 29(416.9 - 298) && \text{(A.216)} \\ &= 3448\ \mathrm{kJ\,kmol^{-1}}. && \text{(A.217)} \end{aligned}$$

The required aftercooler thermal duty was consequently

$$\begin{aligned} \dot{Q}_{\mathrm{AC}} &= \dot{n}_{\mathrm{feed}} \Delta h_{\mathrm{AC}} && \text{(A.218)} \\ &= 0.0223(3448) && \text{(A.219)} \\ &= 76.9\ \mathrm{kW}. && \text{(A.220)} \end{aligned}$$

Thus,

$$\boxed{\dot{Q}_{\mathrm{AC}} = 76.9\ \mathrm{kW}}. \tag{A.221}$$

The calculated aftercooler duty is approximately equal to the compressor shaft power because the hydrogen was assumed to undergo adiabatic compression and was subsequently cooled approximately back to its original inlet temperature.

Selected Aftercooler Capacity

A design factor of 1.10 was applied to account for operating variations and additional thermal load:

$$\begin{aligned} \dot{Q}_{\mathrm{AC,design}} &= 1.10\dot{Q}_{\mathrm{AC}} && \text{(A.222)} \\ &= 1.10(76.9) && \text{(A.223)} \\ &= 84.6\ \mathrm{kW}. && \text{(A.224)} \end{aligned}$$

A nominal aftercooler capacity of

$$\boxed{\dot{Q}_{\mathrm{AC,selected}} \approx 85\ \mathrm{kW}} \tag{A.225}$$

was therefore selected.

The calculated thermal duty of $76.9\ \mathrm{kW}$ was used as the sizing parameter for the OpenPyTEA heat-exchanger cost correlation, whereas the $85\ \mathrm{kW}$ value represents the rounded nominal design capacity.

A.8. Continuous Three-Bed Scheduling Calculation

A staggered three-bed arrangement was proposed to provide a continuous supply of dried hydrogen while allowing each individual bed sufficient time for blowdown, regeneration, cooling and repressurisation.

Duration of One TSA Cycle

The complete simulated TSA cycle consisted of the following steps:

- adsorption: $14\,000\ \mathrm{s}$;
- first blowdown step: $1\,500\ \mathrm{s}$;
- second blowdown step: $2\,000\ \mathrm{s}$;
- first heating stage: $1\,000\ \mathrm{s}$;
- second heating stage: $3\,000\ \mathrm{s}$;
- third heating stage: $3\,000\ \mathrm{s}$;
- fourth heating stage: $8\,000\ \mathrm{s}$;
- cooling: $3\,000\ \mathrm{s}$; and
- repressurisation: $2\,000\ \mathrm{s}$.

The total simulated cycle duration was therefore

$$\begin{aligned} t_{\mathrm{cycle}} &= 14\,000 + 1\,500 + 2\,000 + 1\,000 + 3\,000 \\ &\quad + 3\,000 + 8\,000 + 3\,000 + 2\,000 && \text{(A.226)} \\ &= 37\,500\ \mathrm{s}. && \text{(A.227)} \end{aligned}$$

Thus,

$$\boxed{t_{\mathrm{cycle}} = 37\,500\ \mathrm{s}}. \tag{A.228}$$

The non-adsorption portion of the cycle occupied

$$\begin{aligned} t_{\mathrm{non-ads}} &= t_{\mathrm{cycle}} - t_{\mathrm{ads}} && \text{(A.229)}\\ &= 37\,500 - 14\,000 && \text{(A.230)}\\ &= 23\,500\ \mathrm{s}. && \text{(A.231)} \end{aligned}$$

Minimum Number of Beds

The minimum number of beds required to maintain continuous adsorption was estimated from

$$N_{\mathrm{beds,min}} = \left\lceil \frac{t_{\mathrm{cycle}}}{t_{\mathrm{ads}}} \right\rceil. \tag{A.232}$$

Substitution gives

$$\begin{aligned} N_{\mathrm{beds,min}} &= \left\lceil \frac{37\,500}{14\,000} \right\rceil && \text{(A.233)}\\ &= \lceil 2.679 \rceil && \text{(A.234)}\\ &= 3. && \text{(A.235)} \end{aligned}$$

Therefore,

$$\boxed{N_{\mathrm{beds,min}} = 3}. \tag{A.236}$$

Staggered Adsorption Schedule

The adsorption steps of the three beds were offset by the adsorption duration of $14\,000\ \mathrm{s}$. The proposed sequence was therefore:

$$\text{Bed A:} \qquad 0 \le t < 14\,000\ \mathrm{s},$$

$$\text{Bed B:} \qquad 14\,000 \le t < 28\,000\ \mathrm{s},$$

and

$$\text{Bed C:} \qquad 28\,000 \le t < 42\,000\ \mathrm{s}.$$

Bed A subsequently returned to adsorption at $t = 42\,000\ \mathrm{s}$, after which the sequence was repeated.

The repeat period of an individual bed was therefore

$$t_{\mathrm{bed,repeat}} = N_{\mathrm{beds}} t_{\mathrm{ads}}. \tag{A.237}$$

Thus,

$$\begin{aligned} t_{\mathrm{bed,repeat}} &= 3(14\,000) && \text{(A.238)}\\ &= 42\,000\ \mathrm{s}. && \text{(A.239)} \end{aligned}$$

Pressurised Standby Period

Since the simulated adsorption and regeneration sequence required only

$$t_{\mathrm{cycle}} = 37\,500\ \mathrm{s},$$

while the same bed was required to return to adsorption after

$$t_{\mathrm{bed,repeat}} = 42\,000\ \mathrm{s},$$

the available standby period was

$$t_{\mathrm{standby}} = t_{\mathrm{bed,repeat}} - t_{\mathrm{cycle}}. \tag{A.240}$$

Substitution gives

$$t_{\mathrm{standby}} = 42\,000 - 37\,500 \tag{A.241}$$
$$= 4\,500\ \mathrm{s}. \tag{A.242}$$

Hence,

$$\boxed{t_{\mathrm{standby}} = 4\,500\ \mathrm{s}}. \tag{A.243}$$

During this period, the bed was assumed to remain isolated at approximately $25\ \mathrm{bar}$ after repressurisation and close to the adsorption temperature.

The $4\,500\ \mathrm{s}$ standby period was not explicitly included in the original $37\,500\ \mathrm{s}$ Aspen Adsorption multi-cycle simulation. When extending the simulated cycle to the continuous three-bed arrangement, it was therefore assumed that the additional standby period did not significantly change the bed temperature or adsorbent water loading.

Since dry hydrogen was used during cooling and repressurisation, significant water readsorption during this pressurised standby period was not expected.

Continuous Feed Operation

Because the adsorption periods of the three beds are staggered, at least one bed remains in adsorption at all times. The common hydrogen compressor and compressor aftercooler can therefore operate continuously at the selected feed rate of

$$\boxed{\dot{n}_{\mathrm{feed}} = 0.0223\ \mathrm{kmol\,s^{-1}}}. \tag{A.244}$$

A new adsorption-production interval is completed every

$$t_{\mathrm{slot}} = 14\,000\ \mathrm{s},$$

even though the complete adsorption–regeneration sequence of an individual bed requires $37\,500\ \mathrm{s}$.

Shared Regeneration-Heater Scheduling

The complete heating sequence of one TSA bed consisted of four heating stages with a total duration of

$$t_{\text{heating}} = 1000 + 3000 + 3000 + 8000 \tag{A.245}$$
$$= 15\,000 \text{ s}. \tag{A.246}$$

A new bed completes adsorption every

$$14\,000 \text{ s}.$$

If the simulated schedules were applied without modification, the heating periods of two consecutive beds would therefore overlap by

$$t_{\text{overlap}} = 15\,000 - 14\,000 \tag{A.247}$$
$$= 1000 \text{ s}. \tag{A.248}$$

Thus,

$$\boxed{t_{\text{overlap}} = 1000 \text{ s}}. \tag{A.249}$$

This overlap corresponds to the initial 100°C heating stage of the following bed. The thermal duty associated with this stage was

$$\dot{Q}_1 = 1.63 \times 10^{-4} \text{ kW},$$

which is negligible compared with the later regeneration-heating stages.

A single common regeneration heater was therefore assumed to be sufficient, provided that the initial low-flow heating stage is rescheduled within the available standby margin. Since

$$t_{\text{standby}} = 4500 \text{ s} > t_{\text{overlap}} = 1000 \text{ s},$$

the available scheduling margin is sufficient to avoid simultaneous significant heating demand from two beds without changing the $14\,000$ s continuous production interval.

The TSA cooling-gas cooler was similarly assumed to be shared between the three beds through the automated switching system.

A.9. Blowdown Temperature Estimates

During the TSA blowdown step, the bed pressure decreased from approximately

$$P_1 = 25 \text{ bar}$$

to

$$P_2 = 1 \text{ bar}.$$

The non-isothermal Aspen Adsorption simulation predicted a minimum local temperature of approximately

$$T_{\mathrm{Aspen}} \approx 218.15\ \mathrm{K} \approx -55\,^{\circ}\mathrm{C}.$$

To assess whether this temperature reduction was thermodynamically reasonable, two limiting calculations were performed: a Joule–Thomson estimate based on the Peng–Robinson equation of state and an ideal reversible adiabatic expansion.

A.9.1. Joule--Thomson Expansion

The Joule–Thomson coefficient is defined as

$$\mu_{\mathrm{JT}} = \left(\frac{\partial T}{\partial P}\right)_h, \tag{A.250}$$

where the expansion is considered at constant enthalpy,

$$h_1 = h_2. \tag{A.251}$$

For a real gas, the Joule–Thomson coefficient can be expressed as

$$\mu_{\mathrm{JT}} = \frac{1}{C_p}\left[T\left(\frac{\partial v}{\partial T}\right)_P - v\right]. \tag{A.252}$$

The thermodynamic properties of hydrogen were estimated using the Peng–Robinson equation of state:

$$P = \frac{RT}{v-b} - \frac{a(T)}{v^2 + 2bv - b^2}. \tag{A.253}$$

The temperature-dependent attraction parameter is

$$a(T) = a_c \alpha(T), \tag{A.254}$$

$$a_c = 0.45724 \frac{R^2 T_c^2}{P_c}, \tag{A.255}$$

$$b = 0.07780 \frac{R T_c}{P_c}, \tag{A.256}$$

with

$$\alpha(T) = \left[1 + \kappa\left(1 - \sqrt{T_r}\right)\right]^2, \tag{A.257}$$

$$T_r = \frac{T}{T_c}, \tag{A.258}$$

and

$$\kappa = 0.37464 + 1.54226\omega - 0.26992\omega^2. \tag{A.259}$$

For hydrogen, the properties used were

$$T_c = 33.18\ \mathrm{K}, \tag{A.260}$$
$$P_c = 13\ \mathrm{bar}, \tag{A.261}$$
$$\omega = -0.216, \tag{A.262}$$
$$R = 8.314\ \mathrm{J\,mol^{-1}\,K^{-1}}. \tag{A.263}$$

At the initial blowdown condition,

$$T_1 = 298\ \mathrm{K}, \qquad P_1 = 25\ \mathrm{bar}.$$

The Peng–Robinson parameter κ was

$$\kappa = 0.37464 + 1.54226(-0.216) - 0.26992(-0.216)^2 \tag{A.264}$$
$$= 0.028918. \tag{A.265}$$

The reduced temperature was

$$T_r = \frac{298}{33.18} \tag{A.266}$$
$$\approx 8.99. \tag{A.267}$$

Therefore,

$$\alpha(T) = \left[1 + 0.028918\left(1 - \sqrt{8.99}\right)\right]^2 \tag{A.268}$$
$$\approx 0.888. \tag{A.269}$$

The resulting Peng–Robinson parameters were approximately

$$a_c \approx 2.68 \times 10^{-2}\ \mathrm{Pa\,m^6\,mol^{-2}}, \tag{A.270}$$
$$a(T) \approx 2.38 \times 10^{-2}\ \mathrm{Pa\,m^6\,mol^{-2}}, \tag{A.271}$$
$$b \approx 1.65 \times 10^{-5}\ \mathrm{m^3\,mol^{-1}}. \tag{A.272}$$

The dimensionless Peng–Robinson parameters were calculated as

$$A = \frac{a(T)P}{R^2T^2}, \qquad B = \frac{bP}{RT}. \tag{A.273}$$

At $298\ \mathrm{K}$ and $25\ \mathrm{bar}$,

$$A \approx 0.0097, \tag{A.274}$$
$$B \approx 0.0167. \tag{A.275}$$

The compressibility factor was determined from

$$Z^3 - (1-B)Z^2 + \left(A - 3B^2 - 2B\right)Z - \left(AB - B^2 - B^3\right) = 0. \tag{A.276}$$

The gas-phase root was approximately

$$Z \approx 1.$$

The corresponding molar volume was

$$\begin{aligned} v &= \frac{ZRT}{P} && \text{(A.277)} \\ &\approx 9.9 \times 10^{-4}\ \mathrm{m^3\,mol^{-1}}. && \text{(A.278)} \end{aligned}$$

The required temperature derivative of molar volume was obtained from

$$\left(\frac{\partial v}{\partial T}\right)_P = -\frac{\left(\dfrac{\partial P}{\partial T}\right)_v}{\left(\dfrac{\partial P}{\partial v}\right)_T}, \tag{A.279}$$

giving approximately

$$\left(\frac{\partial v}{\partial T}\right)_P \approx 3.34 \times 10^{-6}\ \mathrm{m^3\,mol^{-1}\,K^{-1}}. \tag{A.280}$$

Using

$$C_p \approx 29\ \mathrm{J\,mol^{-1}\,K^{-1}},$$

the Joule–Thomson coefficient was

$$\begin{aligned} \mu_{\mathrm{JT}} &= \frac{1}{29}\left[298\left(3.34 \times 10^{-6}\right) - 9.9 \times 10^{-4}\right] && \text{(A.281)} \\ &\approx 2.27 \times 10^{-7}\ \mathrm{K\,Pa^{-1}} && \text{(A.282)} \\ &= 0.0227\ \mathrm{K\,bar^{-1}}. && \text{(A.283)} \end{aligned}$$

The pressure change was

$$\begin{aligned} \Delta P &= P_2 - P_1 && \text{(A.284)} \\ &= 1 - 25 && \text{(A.285)} \\ &= -24\ \mathrm{bar}. && \text{(A.286)} \end{aligned}$$

The corresponding Joule–Thomson temperature change was

$$\begin{aligned} \Delta T_{\mathrm{JT}} &= \mu_{\mathrm{JT}} \Delta P && \text{(A.287)} \\ &= \left(0.0227\ \mathrm{K\,bar^{-1}}\right)\left(-24\ \mathrm{bar}\right) && \text{(A.288)} \\ &= -0.5448\ \mathrm{K}. && \text{(A.289)} \end{aligned}$$

The final temperature predicted from this approximation was therefore

$$T_{2,\mathrm{JT}} = T_1 + \Delta T_{\mathrm{JT}} \tag{A.290}$$
$$= 298 - 0.5448 \tag{A.291}$$
$$= 297.46\ \mathrm{K} \tag{A.292}$$
$$\approx 24.3\,^{\circ}\mathrm{C}. \tag{A.293}$$

Thus,

$$\boxed{T_{2,\mathrm{JT}} \approx 297.46\ \mathrm{K} \approx 24.3\,^{\circ}\mathrm{C}}. \tag{A.294}$$

The Joule–Thomson effect therefore predicts only a small temperature decrease for the 25 to $1\ \mathrm{bar}$ pressure reduction.

A.9.2. Ideal Reversible Adiabatic Expansion

For comparison, the opposite limiting case was estimated by treating the blowdown as an ideal reversible adiabatic, or isentropic, expansion of an ideal gas:

$$\frac{T_2}{T_1} = \left(\frac{P_2}{P_1}\right)^{\frac{\gamma-1}{\gamma}}. \tag{A.295}$$

A heat-capacity ratio of

$$\gamma = 1.4$$

was assumed for hydrogen.

Substitution gives

$$T_{2,\mathrm{ad}} = 298\left(\frac{1}{25}\right)^{\frac{1.4-1}{1.4}} \tag{A.296}$$
$$= 118.79\ \mathrm{K}. \tag{A.297}$$

Converting to degrees Celsius,

$$T_{2,\mathrm{ad}} = 118.79 - 273.15 \tag{A.298}$$
$$= -154.36\,^{\circ}\mathrm{C}. \tag{A.299}$$

Therefore,

$$\boxed{T_{2,\mathrm{ad}} \approx 118.79\ \mathrm{K} \approx -154.4\,^{\circ}\mathrm{C}}. \tag{A.300}$$

This represents an idealised limiting case in which the expanding gas receives no heat from the adsorbent particles or vessel wall.

A.9.3. Comparison with the Aspen Adsorption Result

The three temperature estimates were

$$T_{2,\mathrm{JT}} \approx 297.46\ \mathrm{K} = 24.3\,^{\circ}\mathrm{C}, \tag{A.301}$$

$$T_{\mathrm{Aspen}} \approx 218.15\ \mathrm{K} = -55\,^{\circ}\mathrm{C}, \tag{A.302}$$

$$T_{2,\mathrm{ad}} \approx 118.79\ \mathrm{K} = -154.4\,^{\circ}\mathrm{C}. \tag{A.303}$$

Consequently,

$$\boxed{T_{2,\mathrm{ad}} < T_{\mathrm{Aspen}} < T_{2,\mathrm{JT}}}. \tag{A.304}$$

The Aspen Adsorption prediction lies between the two limiting estimates. The simulated blowdown should therefore not be interpreted as either a purely isenthalpic Joule–Thomson throttling process or an ideal reversible isentropic expansion. Instead, the transient temperature response reflects the combined effects of gas expansion, pressure variation and heat transfer between the gas, adsorbent and vessel wall.

B

Detailed Techno-Economic Analysis

This appendix presents the detailed inputs, equipment-costing basis and economic assumptions used in the final OpenPyTEA techno-economic analysis of the three-bed TSA hydrogen-drying process. The main text presents the principal methodology and economic results, whereas the detailed model inputs, equipment correlations and intermediate calculations are documented here for reproducibility.

B.1. OpenPyTEA Model Configuration

The techno-economic assessment was implemented using [76]. Process equipment sizes and operating requirements obtained from the TSA process analysis were supplied to the corresponding equipment-cost correlations available in the OpenPyTEA database.

The economic model represents the incremental cost of the hydrogen-drying section integrated within a larger hydrogen-production facility. Upstream hydrogen production by electrolysis and downstream hydrogen distribution infrastructure were therefore excluded from the economic boundary.

The principal OpenPyTEA configuration parameters are summarised in Table B.1.

Table B.1: Base-case OpenPyTEA model configuration.

Parameter	Value	Unit
Plant name	TSA Green Hydrogen Drying	–
Process type	Fluids	–
Plant location	Netherlands	–
Target cost year	2024	–
Reporting currency	EUR	–
Exchange-rate basis	$1\ \mathrm{EUR} = 1.0824\ \mathrm{USD}$	–
Project lifetime	20	years
Interest rate	9	%
Base-case plant utilisation	100	%
Electricity price	0.246	EUR kWh^{-1}
Operator hourly rate	35.21	EUR h^{-1}
Allocated operating labour	1	FTE
OSBL factor	20	% of ISBL
Design and engineering	30	%
Contingency	10	%
Working-capital factor	15	% of FCI
Heater efficiency	90	%
Number of TSA beds	3	–
TSA active cycle time	37,500	s
Annual dry-H_2 production	1.325388×10^6	kg year^{-1}

The annual dry-hydrogen production was obtained from the continuous three-bed production rate of $151.3\ \mathrm{kg\,h^{-1}}$. At the base-case plant utilisation of 100%,

$$m_{\mathrm{H_2,annual}} = 151.3(24)(365) = 1.325388 \times 10^{6}\ \mathrm{kg\,year^{-1}}. \tag{B.1}$$

The exchange-rate conversion used in the OpenPyTEA model was

$$F_{\mathrm{USD}\to\mathrm{EUR}} = \frac{1}{1.0824} = 0.9239. \tag{B.2}$$

OpenPyTEA equipment costs expressed on a US-dollar basis were therefore converted to euros using this factor.

B.2. Equipment Included in the Final Economic Model

The final OpenPyTEA model contained eight equipment objects. The three TSA adsorption vessels were represented individually because each pressure vessel is a separate installed equipment item. The final equipment inputs are listed in Table B.2.

Table B.2: Equipment inputs supplied to OpenPyTEA in the final TSA model.

Equipment	OpenPyTEA input	Equipment type	Costing basis
Hydrogen compressor	$93\ \mathrm{kW}$ cost floor	Reciprocating compressor	Towler driver-power correlation; actual process shaft power is $76.9\ \mathrm{kW}$
Compressor aftercooler	$76.9\ \mathrm{kW}$	Heat exchanger	Nexant duty-based correlation
TSA vessel 1	$120\ \mathrm{kg}$	Vertical 304SS vessel	Minimum shell-mass correlation limit
TSA vessel 2	$120\ \mathrm{kg}$	Vertical 304SS vessel	Minimum shell-mass correlation limit
TSA vessel 3	$120\ \mathrm{kg}$	Vertical 304SS vessel	Minimum shell-mass correlation limit
Regeneration-gas heater	$5.238\ \mathrm{kW}$ thermal duty	Heat exchanger	Nexant duty-based correlation used as a small indirect gas-heater proxy
TSA cooling-gas cooler	$2.5\ \mathrm{kW}$	Heat exchanger	Nexant duty-based correlation
Waste receiver	$613.2\ \mathrm{kg}$	Horizontal carbon-steel vessel	Preliminary shell-mass input

For the compressor, three power values are distinguished. The ideal-fluid compression power is approximately $57.7\ \mathrm{kW}$, the required shaft power is $76.9\ \mathrm{kW}$, and the electrical input after motor losses is $80.9\ \mathrm{kW}$. The reciprocating-compressor cost correlation begins at $93\ \mathrm{kW}$. Since the actual shaft requirement lies below this lower limit, $93\ \mathrm{kW}$ was used only as the CAPEX costing floor. The physical process duty was not increased; $76.9\ \mathrm{kW}$ remains the required shaft power and $80.9\ \mathrm{kW}$ remains the electrical demand used for OPEX.

The regeneration-gas heater was not represented using the OpenPyTEA cylindrical-furnace option in the final model. The furnace correlation produced an implausibly high equipment cost for the very small heater required in this process. Instead, the heater was represented by the built-in Nexant duty-based heat-exchanger correlation using the design thermal duty of $5.238\ \mathrm{kW}$. The physical process unit remains a regeneration-gas heater; the heat-exchanger representation is only an economic proxy.

A separate dry-hydrogen storage vessel was not included in the final economic boundary. The preliminary $21\ \mathrm{m}^3$ vessel represented approximately one cycle of internal regeneration and cooling hydrogen. In the final integrated configuration, this gas is taken from the continuously available dry-product header. Including a dedicated storage vessel in addition to that shared header would therefore double count storage capacity within the selected incremental boundary.

B.3. Treatment of TSA Vessels, Valves and Zeolite

The calculated cylindrical shell mass of one TSA vessel was approximately

$$m_{\mathrm{shell,actual}} = 23.73\ \mathrm{kg}.$$

The OpenPyTEA correlation selected for a vertical 304 stainless-steel pressure vessel is applicable from a minimum shell mass of

$$m_{\mathrm{shell,min}} = 120\ \mathrm{kg}.$$

Since $23.73 < 120\ \mathrm{kg}$, direct extrapolation below the stated correlation range was avoided. The minimum correlation value was therefore applied as a costing floor:

$$\boxed{m_{\mathrm{TSA,cost}} = 120\ \mathrm{kg\,vessel}^{-1}}. \tag{B.3}$$

The actual calculated shell mass remained $23.73\ \mathrm{kg}$; the $120\ \mathrm{kg}$ value was used only for economic costing.

The physical three-bed TSA system requires twelve automated switching valves, corresponding to four principal valves per bed. However, the OpenPyTEA cost database did not contain an applicable automated process-valve correlation. The valves were therefore retained within the physical process boundary but were not included as separate purchased-equipment items. Their associated piping, instrumentation, electrical and installation requirements are partly represented through the general OpenPyTEA installation factors.

Similarly, no applicable built-in OpenPyTEA equipment-cost correlation was available for Zeolite 4A. To maintain an OpenPyTEA-only deterministic costing basis, no external adsorbent supplier price was introduced. The initial zeolite charge and replacement cost are therefore not explicitly represented and remain limitations of the screening-level economic assessment.

B.4. OpenPyTEA Equipment Cost Correlations

Equipment purchase costs were estimated using correlations contained within the OpenPyTEA equipment-cost database. The final correlation basis is summarised in Table B.3.

Table B.3: OpenPyTEA equipment-cost correlations used in the final TSA economic model.

Equipment	OpenPyTEA correlation	Sizing variable	Validity treatment	Original cost basis
Hydrogen compressor	Reciprocating compressor	Driver power [kW]	Lower correlation limit of $93\ \mathrm{kW}$ used	Towler
Compressor aftercooler	Heat exchanger	Duty [MMBTU h^{-1}]	Duty used directly	Nexant
TSA pressure vessels	Vertical 304SS pressure vessel	Shell mass [kg]	$120\ \mathrm{kg}$ lower limit used	Towler
Regeneration-gas heater	Heat exchanger	Duty [MMBTU h^{-1}]	Screening-level heater proxy	Nexant
TSA cooling-gas cooler	Heat exchanger	Duty [MMBTU h^{-1}]	Duty used directly	Nexant
Waste receiver	Horizontal carbon-steel pressure vessel	Shell mass [kg]	Preliminary shell mass within correlation range	Towler

B.4.1. Hydrogen Compressor Correlation

The final model used the OpenPyTEA reciprocating-compressor correlation. The required process shaft power was

$$\dot{W}_{\mathrm{shaft}} = 76.9\ \mathrm{kW}.$$

Because the lower driver-power limit of the selected correlation is $93\ \mathrm{kW}$, direct extrapolation below the stated range was avoided. The CAPEX input was therefore

$$\boxed{\dot{W}_{\mathrm{comp,cost}} = 93\ \mathrm{kW}}. \tag{B.4}$$

The compressor electrical input of $80.9\ \mathrm{kW}$ was used separately for the electricity calculation and was not used as the equipment-costing input.

B.4.2. Heat-Exchanger Correlations

The compressor aftercooler, regeneration-gas heater proxy and TSA cooling-gas cooler were represented using the Nexant duty-based heat-exchanger correlation. The conversion from kilowatts to MMBTU h^{-1} was

$$\dot{Q}_{\mathrm{MMBTU/h}} = 0.00341214 \dot{Q}_{\mathrm{kW}}. \tag{B.5}$$

For the compressor aftercooler,

$$\dot{Q}_{\mathrm{AC,cost}} = 76.9(0.00341214) = 0.2624\ \mathrm{MMBTU\,h^{-1}}. \tag{B.6}$$

For the regeneration-gas heater,

$$\dot{Q}_{\mathrm{heater,cost}} = 5.238(0.00341214) = 0.01787\ \mathrm{MMBTU\,h^{-1}}. \tag{B.7}$$

For the TSA cooling-gas cooler,

$$\dot{Q}_{\mathrm{cooler,cost}} = 2.5(0.00341214) = 0.00853\ \mathrm{MMBTU\,h^{-1}}. \tag{B.8}$$

B.4.3. TSA Pressure-Vessel Correlation

The three TSA vessels were represented using the vertical 304 stainless-steel pressure-vessel correlation. The actual cylindrical shell mass was $23.73\ \mathrm{kg}$ per vessel, below the $120\ \mathrm{kg}$ lower correlation limit. Therefore,

$$\boxed{m_{\mathrm{TSA,cost}} = 120\ \mathrm{kg\,vessel^{-1}}} \tag{B.9}$$

was used for each of the three separate OpenPyTEA vessel objects.

B.4.4. Waste-Receiver Correlation

The waste receiver was represented using the horizontal carbon-steel pressure-vessel correlation. The preliminary shell mass supplied to OpenPyTEA was

$$\boxed{m_{\mathrm{waste}} = 613.2\ \mathrm{kg}}. \tag{B.10}$$

This value lies within the stated $160 - -50\,000\ \mathrm{kg}$ correlation range. The receiver remains a screening-level design because its final volume, wall thickness and allowable pressure require detailed transient and mechanical design.

B.5. Preliminary Waste-Receiver Sizing

A preliminary waste-gas receiver volume of

$$V_{\mathrm{waste}} = 5\ \mathrm{m^3}$$

was retained for the screening-level economic analysis. The vessel provides short-duration surge capacity for gas discharged during blowdown and regeneration rather than permanent storage of the complete waste stream. A cylindrical geometry with

$$\frac{L}{D_i} = 3$$

was assumed. The internal diameter was obtained from

$$D_i = \left(\frac{4V_{\mathrm{waste}}}{3\pi}\right)^{1/3} = 1.285\ \mathrm{m}, \tag{B.11}$$

and the corresponding cylindrical length was

$$L = 3D_i = 3.855\ \mathrm{m}. \tag{B.12}$$

A practical nominal shell thickness of

$$t_{\mathrm{waste}} = 5\ \mathrm{mm} = 0.005\ \mathrm{m}$$

was assumed for the preliminary calculation. The outer diameter was therefore $D_o = 1.295\ \mathrm{m}$. The cylindrical shell volume was

$$V_{\text{shell,waste}} = \frac{\pi}{4}(D_o^2 - D_i^2)L \approx 0.0781 \text{ m}^3. \tag{B.13}$$

Using a carbon-steel density of $\rho_{\text{CS}} = 7850 \text{ kg m}^{-3}$,

$$m_{\text{waste}} = \rho_{\text{CS}} V_{\text{shell,waste}} = 613.2 \text{ kg}. \tag{B.14}$$

The assumed 5 m^3 volume and 5 mm shell thickness should be regarded as preliminary screening assumptions. Final sizing requires the transient blowdown flow, maximum allowable receiver pressure, downstream discharge conditions and a complete mechanical design.

B.6. Purchased and Direct Installed Equipment Costs

OpenPyTEA was used to calculate the purchased and direct installed cost for each equipment item. The final results are summarised in Table B.4.

Table B.4: Purchased and direct installed equipment costs obtained using OpenPyTEA.

Equipment	Purchased cost (EUR)	Direct installed cost (EUR)
Hydrogen compressor	457,386	1,463,634
Compressor aftercooler	184,147	589,270
Three TSA pressure vessels	88,656	331,573
Regeneration-gas heater	36,737	117,560
TSA cooling-gas cooler	23,571	75,426
Waste receiver	23,426	74,964
Total	**813,923**	**2,652,428**

The unrounded purchased-equipment subtotal was approximately

$$\boxed{C_{\text{purchased}} = 813{,}923 \text{ EUR}}. \tag{B.15}$$

The direct installed cost was

$$\boxed{C_{\text{direct}} = 2{,}652{,}428 \text{ EUR}}. \tag{B.16}$$

The hydrogen compressor is the largest purchased-cost item. The regeneration heater is no longer a dominant CAPEX item because the final model uses the small duty-based heat-exchanger proxy rather than the cylindrical-furnace correlation.

OpenPyTEA calculates the direct installed cost from purchased cost using its standard material and installation factors. In general,

$$C_{\text{direct}} = C_p \left[(1 + f_{\text{piping}}) f_{\text{material}} + f_{\text{erection}} + f_{\text{electrical}} + f_{\text{instrumentation}} + f_{\text{civil}} + f_{\text{structural}} + f_{\text{lagging}}\right]. \tag{B.17}$$

For the default carbon-steel fluid-process equipment, the retained OpenPyTEA factors give a direct-to-purchased-cost ratio of approximately 3.20. For the 304 stainless-steel TSA vessels, the material factor increases the ratio to approximately 3.74. Across the complete equipment set, the resulting ratio is approximately

$$\frac{2.652}{0.814} \approx 3.26. \tag{B.18}$$

No external reduction of the installation factors was applied in the final base case.

B.7. Capital-Cost Calculation

The total direct installed cost was

$$C_{\mathrm{direct}} = 2{,}652{,}428\ \mathrm{EUR}. \tag{B.19}$$

For the Netherlands, the OpenPyTEA location factor was

$$F_{\mathrm{loc}} = 1.19.$$

The inside-battery-limits cost was therefore

$$C_{\mathrm{ISBL}} = F_{\mathrm{loc}} C_{\mathrm{direct}} \approx 3{,}156{,}389\ \mathrm{EUR}. \tag{B.20}$$

For the final integrated hydrogen-drying boundary, the OSBL factor was set to

$$F_{\mathrm{OSBL}} = 0.20.$$

Thus,

$$C_{\mathrm{OSBL}} = 0.20 C_{\mathrm{ISBL}} \approx 631{,}278\ \mathrm{EUR}. \tag{B.21}$$

Design and engineering and contingency were retained at 30% and 10%, respectively, of the combined ISBL and OSBL basis:

$$C_{\mathrm{D\&E}} = 0.30(C_{\mathrm{ISBL}} + C_{\mathrm{OSBL}}) \approx 1{,}136{,}300\ \mathrm{EUR}, \tag{B.22}$$

$$C_{\mathrm{cont}} = 0.10(C_{\mathrm{ISBL}} + C_{\mathrm{OSBL}}) \approx 378{,}767\ \mathrm{EUR}. \tag{B.23}$$

The fixed capital investment was therefore

$$C_{\mathrm{FCI}} = C_{\mathrm{ISBL}} + C_{\mathrm{OSBL}} + C_{\mathrm{D\&E}} + C_{\mathrm{cont}}, \tag{B.24}$$

which gives

$$\boxed{C_{\mathrm{FCI}} = 5{,}302{,}733\ \mathrm{EUR} \approx 5.303\ \mathrm{million\ EUR}}. \tag{B.25}$$

The resulting capital-cost breakdown is summarised in Table B.5.

Table B.5: Detailed capital-cost breakdown obtained using OpenPyTEA.

Capital-cost component	Cost (EUR)
Total purchased equipment	813,923
Total direct installed equipment	2,652,428
ISBL	3,156,389
OSBL	631,278
Design and engineering	1,136,300
Contingency	378,767
Fixed capital investment	**5,302,733**

Working capital is treated separately in the OpenPyTEA economic model and is not included in the FCI reported above.

B.8. Electricity Consumption and Variable OPEX Calculation

The variable operating expenditure included electricity consumed by the hydrogen compressor and regeneration-gas heater. The thermal duties of the compressor aftercooler and TSA cooling-gas cooler were used for equipment sizing but were not converted to additional electrical loads because a specific cooling-system power requirement was not defined.

The compressor electrical input was

$$\dot{W}_{\mathrm{comp,el}} = 80.9\ \mathrm{kW}.$$

Since the compressor operates continuously,

$$E_{\mathrm{comp,d}} = 80.9(24) = 1941.6\ \mathrm{kWh\,day^{-1}}. \tag{B.26}$$

The staged regeneration calculation gave a sensible energy supplied to the regeneration hydrogen of

$$Q_{\mathrm{regen,H_2}} = 47.13\ \mathrm{MJ\,cycle^{-1}\,bed^{-1}}.$$

This quantity was used for heater OPEX. The separately calculated $25.18\ \mathrm{MJ\,cycle^{-1}\,bed^{-1}}$ theoretical bed-regeneration requirement was not added to it, because the hot regeneration gas supplies that bed heating and desorption demand.

For a heater efficiency of $\eta_{\mathrm{heater}} = 0.90$,

$$E_{\mathrm{heater,cycle}} = \frac{47.13}{0.90(3.6)} = 14.55\ \mathrm{kWh\,cycle^{-1}\,bed^{-1}}. \tag{B.27}$$

Using the active single-bed cycle time of $37\,500\ \mathrm{s}$, one bed completes

$$N_{\mathrm{cycle,bed,d}} = \frac{86\,400}{37\,500} = 2.304\ \mathrm{cycles\,day^{-1}}. \tag{B.28}$$

For three beds,

$$N_{\mathrm{cycle,total,d}} = 3(2.304) = 6.912\ \mathrm{bed\ cycles\,day^{-1}}. \tag{B.29}$$

The daily heater electricity consumption was therefore

$$E_{\mathrm{heater,d}} = 14.5463(6.912) = 100.544\ \mathrm{kWh\,day^{-1}}. \tag{B.30}$$

The total electricity use was

$$E_{\mathrm{el,d}} = 1941.6 + 100.544 = 2042.144\ \mathrm{kWh\,day^{-1}}, \tag{B.31}$$

or

$$E_{\mathrm{el,annual}} = 2042.144(365) = 745{,}382.6\ \mathrm{kWh\,year^{-1}}. \tag{B.32}$$

At the base-case electricity price of $0.246\ \mathrm{EUR\,kWh^{-1}}$,

$$C_{\mathrm{OPEX,var}} = 745{,}382.6(0.246) = 183{,}364\ \mathrm{EUR\,year^{-1}}. \tag{B.33}$$

The electricity-cost breakdown is summarised in Table B.6.

Table B.6: Base-case electricity consumption and variable operating cost.

Electrical load	Consumption (kWh/year)	Cost (EUR/year)
Hydrogen compressor	708,684	174,336
Regeneration-gas heater	36,699	9,028
Total	**745,383**	**183,364**

The compressor accounts for approximately 95% of the electricity consumption included in the base case.

B.9. Fixed Operating Expenditure Calculation

The final fixed-OPEX calculation was modified to reflect the incremental TSA boundary. OpenPyTEA's automatic staffing routine would assign approximately 2.685 operators per shift and, after allowance for shift coverage, would produce a total requirement of 13 operators for the small stand-alone flowsheet [76]. This was judged inappropriate for an automated drying section integrated within an existing hydrogen-production facility.

The final deterministic base case therefore allocated one full-time-equivalent operator to the TSA section. This does not imply that the complete hydrogen facility is operated by one person; it represents only the incremental labour charged to the drying section.

The unrounded hourly labour rate used in the calculation was approximately $35.2088\ \mathrm{EUR\,h^{-1}}$. With $1960\ \mathrm{h\,year^{-1}}$ per FTE,

$$C_{\mathrm{labor}} = 1(1960)(35.2088) = 69{,}009.24\ \mathrm{EUR\,year^{-1}}. \tag{B.34}$$

Supervision was retained at 25% of operating labour:

$$C_{\mathrm{supervision}} = 17{,}252.31\ \mathrm{EUR\,year^{-1}}. \tag{B.35}$$

Direct salary overhead was retained at 50% of labour plus supervision:

$$C_{\mathrm{salary}} = 43{,}130.77\ \mathrm{EUR\,year^{-1}}. \tag{B.36}$$

Maintenance was calculated as 5% of ISBL:

$$C_{\mathrm{maintenance}} = 0.05(3{,}156{,}389) \approx 157{,}819.44\ \mathrm{EUR\,year^{-1}}. \tag{B.37}$$

Taxes and insurance were calculated as 1.5% of ISBL:

$$C_{\mathrm{tax+insurance}} = 0.015(3{,}156{,}389) \approx 47{,}345.83\ \mathrm{EUR\,year^{-1}}. \tag{B.38}$$

Environmental charges were calculated as 1% of the combined ISBL and OSBL basis:

$$C_{\mathrm{environment}} = 0.01(3{,}156{,}389 + 631{,}278) \approx 37{,}876.67\ \mathrm{EUR\,year^{-1}}. \tag{B.39}$$

Operating supplies were calculated as 0.9% of ISBL:

$$C_{\mathrm{supplies}} = 0.009(3{,}156{,}389) \approx 28{,}407.50\ \mathrm{EUR\,year^{-1}}. \tag{B.40}$$

Working capital was estimated as 15% of FCI:

$$C_{\mathrm{WC}} = 0.15(5{,}302{,}733) \approx 795{,}410\ \mathrm{EUR}. \tag{B.41}$$

At a 9% interest rate,

$$C_{\mathrm{WC,int}} = 0.09 C_{\mathrm{WC}} \approx 71{,}586.90\ \mathrm{EUR\,year^{-1}}. \tag{B.42}$$

Fixed-OPEX categories that were not considered incremental to the integrated drying section were set to zero: laboratory charges, additional land rent, general plant overhead, patents and royalties, distribution and selling, and research and development. These costs were excluded to avoid charging the TSA section again for services assumed to exist at the surrounding hydrogen-production facility.

The final fixed-OPEX breakdown is given in Table B.7.

Table B.7: Detailed fixed operating-cost breakdown for the integrated TSA drying section.

Fixed-OPEX component	Cost (EUR/year)
Operating labour	69,009
Supervision	17,252
Direct salary overhead	43,131
Laboratory charges	0
Maintenance	157,819
Taxes and insurance	47,346
Rent of additional land	0
Environmental charges	37,877
Operating supplies	28,407
General plant overhead	0
Interest on working capital	71,587
Patents and royalties	0
Distribution and selling	0
Research and development	0
Total fixed OPEX	**472,429**

Thus,

$$\boxed{C_{\mathrm{OPEX,fixed}} = 472{,}429\ \mathrm{EUR\,year^{-1}}}. \tag{B.43}$$

Combining fixed and variable OPEX gives

$$C_{\mathrm{OPEX,total}} = 472{,}429 + 183{,}364 = 655{,}793\ \mathrm{EUR\,year^{-1}}. \tag{B.44}$$

The fixed and variable shares are approximately 72% and 28%, respectively. Fixed costs remain larger than electricity expenditure, but the corrected integrated model is no longer dominated by the stand-alone staffing and overhead assumptions of the preliminary analysis.

B.10. Levelized Cost Calculation

The deterministic OpenPyTEA model used

$$C_{\mathrm{FCI}} = 5.303\ \text{million EUR},$$

$$C_{\mathrm{OPEX,fixed}} = 0.472\ \text{million EUR\,year}^{-1},$$

$$C_{\mathrm{OPEX,var}} = 0.183 \text{ million EUR}\,\mathrm{year}^{-1},$$

and

$$m_{\mathrm{H_2,annual}} = 1.325388 \times 10^{6} \text{ kg}\,\mathrm{year}^{-1}.$$

The project lifetime and discount rate were

$$N = 20 \text{ years}, \qquad i = 0.09.$$

The levelized cost is calculated from discounted capital and operating costs divided by discounted dry-hydrogen production:

$$LCOP = \frac{\sum_t \frac{C_{\mathrm{CAPEX},t} + C_{\mathrm{OPEX},t}}{(1+i)^t}}{\sum_t \frac{m_{\mathrm{H_2},t}}{(1+i)^t}}. \tag{B.45}$$

The OpenPyTEA capital-expenditure profile distributes FCI over the construction period according to

$$f_{\mathrm{CAPEX}} = [0.30,\ 0.60,\ 0.10].$$

Using $C_{\mathrm{FCI}} = 5{,}302{,}733 \text{ EUR}$, this corresponds to approximately

$$C_{\mathrm{CAPEX},1} = 1.591 \text{ million EUR}, \tag{B.46}$$
$$C_{\mathrm{CAPEX},2} = 3.182 \text{ million EUR}, \tag{B.47}$$
$$C_{\mathrm{CAPEX},3} = 0.530 \text{ million EUR}. \tag{B.48}$$

Working capital was approximately $0.795 \text{ million EUR}$, introduced and released according to the OpenPyTEA cash-flow treatment. The production ramp used in the model was

$$f_{\mathrm{prod}} = [0,\ 0,\ 0.40,\ 0.80,\ 1.00, \ldots, 1.00].$$

At full production, the annual operating cost was approximately

$$C_{\mathrm{OPEX,full}} = 0.472 + 0.183 = 0.656 \text{ million EUR}\,\mathrm{year}^{-1}. \tag{B.49}$$

Application of the complete OpenPyTEA discounted cash-flow calculation gave

$$LCOP_{\mathrm{base}} = 1.179195 \text{ EUR}\,\mathrm{kg}_{\mathrm{H_2}}^{-1}, \tag{B.50}$$

reported as

$$\boxed{LCOP_{\mathrm{base}} = 1.179 \text{ EUR}\,\mathrm{kg}_{\mathrm{H_2}}^{-1}}. \tag{B.51}$$

This value represents only the incremental drying cost. It does not include the upstream cost of producing wet hydrogen by electrolysis or the downstream cost of hydrogen distribution.

B.11. Sensitivity and Monte Carlo Uncertainty Analysis

The deterministic TEA represents one combination of technical and economic assumptions. Structural scenario checks and a combined technical–economic Monte Carlo analysis were therefore performed to test the robustness of the result.

B.11.1. Operator-Requirement and Integration Sensitivity

The preliminary automatic OpenPyTEA staffing method produced 13 operators for the stand-alone representation. Before the final integrated fixed-OPEX boundary was adopted, the effect of reducing the dedicated operator count was examined while retaining the other default overhead categories. The resulting LCOP values were approximately:

Table B.8: Diagnostic sensitivity of LCOP to dedicated operator count before integrated-overhead exclusions.

Dedicated operators	LCOP (EUR $\mathrm{kg}_{\mathrm{H_2}}^{-1}$)
13	4.349
8	3.142
5	2.418
3	1.936
1	1.453

This diagnostic showed that the automatic stand-alone staffing assumption was a major structural cost driver. The final base case therefore combined one allocated FTE with the integrated-boundary treatment of non-incremental fixed OPEX. With the same integrated fixed-OPEX treatment but a 30% OSBL factor, LCOP was approximately $1.235\ \mathrm{EUR\,kg^{-1}}$. Reducing OSBL to the final 20% integrated assumption gave the deterministic value of $1.179\ \mathrm{EUR\,kg^{-1}}$.

B.11.2. Installation-Factor Screening

The final deterministic base case retained 100% of the standard OpenPyTEA installation factors. A diagnostic screening calculation was also performed to show the effect of reducing the packaged installation factors. This sensitivity was not used to select the base case.

Table B.9: Screening sensitivity to the OpenPyTEA installation-factor basis.

Installation-factor basis	LCOP (EUR $\mathrm{kg}_{\mathrm{H_2}}^{-1}$)
100% of OpenPyTEA defaults	1.179195
75% of default auxiliary factors	1.046891
50% of default auxiliary factors	0.914588

The unmodified OpenPyTEA factors were retained in the reported base case to avoid tuning the cost model solely to obtain a lower LCOP.

B.11.3. Monte Carlo Uncertainty Framework

A combined Monte Carlo analysis was performed using

$$N_{\mathrm{MC}} = 10\,000$$

realisations and a random seed of 42. All uncertain variables were sampled from bounded truncated-normal distributions. For a generic uncertain variable X,

$$X \sim \mathcal{TN}(\mu, \sigma, X_{\min}, X_{\max}). \tag{B.52}$$

The selected ranges are screening-level uncertainty assumptions. They should not be interpreted as experimentally measured population standard deviations.

B.11.4. Economic Uncertainty Inputs

Table B.10: Economic uncertainty assumptions used in the final Monte Carlo analysis.

Parameter	Mean	Std. dev.	Minimum	Maximum
CAPEX multiplier	1.00	0.20	0.70	1.50
OSBL factor	0.20	0.05	0.10	0.30
Interest rate	0.09	0.02	0.05	0.13
Project lifetime [yr]	20	5	10	30
Electricity price [EUR kWh^{-1}]	0.246	0.04	0.15	0.35
Operator rate [EUR h^{-1}]	35.21	7.0	20.0	50.0

The CAPEX multiplier represents uncertainty in the screening-level equipment and installed-capital estimate. The OSBL factor independently represents uncertainty in the extent of shared off-site infrastructure. Interest rate, project lifetime, electricity price and operator rate represent economic scenario uncertainty.

B.11.5. Technical Uncertainty Inputs

Table B.11: Technical uncertainty assumptions used in the final Monte Carlo analysis.

Parameter	Mean	Std. dev.	Minimum	Maximum
Compressor electrical power [kW]	80.9	8.09	64.72	97.08
Regeneration energy [MJ cycle^{-1}]	47.13	7.07	32.99	61.27
TSA cycle time [s]	37,500	3,750	30,000	45,000
Dry-H_2 production rate [kg h^{-1}]	151.3	7.565	136.17	166.43

The compressor-power and cycle-time standard deviations correspond to approximately 10% of their base values, the regeneration-energy standard deviation to approximately 15%, and the dry-hydrogen production-rate standard deviation to approximately 5%.

For each realisation, compressor power changed annual compressor electricity, while sampled regeneration energy and cycle time changed heater electricity:

$$E_{\mathrm{comp,d}} = P_{\mathrm{comp}}(24), \tag{B.53}$$

$$E_{\mathrm{heater,d}} = \frac{Q_{\mathrm{regen,H_2}}}{\eta_{\mathrm{heater}}(3.6)} \left(\frac{86\,400}{t_{\mathrm{cycle}}} \right) N_{\mathrm{beds}}. \tag{B.54}$$

The sampled dry-hydrogen production rate changed the annual product quantity:

$$m_{\mathrm{H_2,annual}} = \dot{m}_{\mathrm{H_2}}(24)(365). \tag{B.55}$$

Each sampled project lifetime was evaluated over its corresponding discounted cash-flow horizon before the LCOP samples were recombined.

B.11.6. Final Monte Carlo Distribution

The final $10\,000$-realisation combined technical–economic Monte Carlo analysis produced the distribution summarised in Table B.12.

Table B.12: Detailed summary of the final Monte Carlo LCOP distribution.

Statistic	LCOP (EUR $\mathrm{kg}_{\mathrm{H_2}}^{-1}$)
Mean	1.232123
Standard deviation	0.225117
Median	1.210976
2.5th percentile	0.852060
5th percentile	0.900895
95th percentile	1.635754
97.5th percentile	1.722989

The central 95% uncertainty interval was therefore

$$\boxed{0.852 \leq LCOP \leq 1.723 \ \mathrm{EUR}\,\mathrm{kg}_{\mathrm{H_2}}^{-1}}. \tag{B.56}$$

The deterministic LCOP was $1.179195 \ \mathrm{EUR}\,\mathrm{kg}_{\mathrm{H_2}}^{-1}$, while the Monte Carlo median was $1.210976 \ \mathrm{EUR}\,\mathrm{kg}_{\mathrm{H_2}}^{-1}$. The slightly larger Monte Carlo mean and median reflect the nonlinear propagation of the uncertain economic and technical inputs through the discounted cost model.

B.11.7. Spearman Rank Sensitivity Analysis

The relative importance of the uncertain inputs was quantified using the Spearman rank correlation coefficient,

$$\rho_s = \mathrm{corr}[\mathrm{rank}(X), \mathrm{rank}(LCOP)]. \tag{B.57}$$

The final coefficients are listed in Table B.13.

Table B.13: Spearman rank correlation coefficients for the final combined technical–economic uncertainty analysis.

Parameter	ρ_s	Absolute ρ_s
CAPEX multiplier	0.692790	0.692790
Interest rate	0.478748	0.478748
Project lifetime	-0.339479	0.339479
Dry-H_2 production rate	-0.239729	0.239729
Operator hourly rate	0.104630	0.104630
OSBL factor	0.102938	0.102938
Electricity price	0.093539	0.093539
Compressor electrical power	0.048131	0.048131
Regeneration energy	0.015431	0.015431
TSA cycle time	0.006300	0.006300

The CAPEX multiplier showed the strongest positive relationship with LCOP, followed by the interest rate. Project lifetime and dry-hydrogen production rate showed negative correlations because a longer operating period and a higher production rate distribute the capital and operating costs over more product. Operator rate and OSBL had smaller but still visible effects. The technical electricity-related variables were comparatively weak within the selected uncertainty ranges, particularly regeneration energy and cycle time.

References

[1] Yorick Ligen, Heron Vrubel, and Hubert Girault. “Energy efficient hydrogen drying and purification for fuel cell vehicles”. In: *International Journal of Hydrogen Energy* 45.18 (2020), pp. 10639–10647. ISSN: 0360-3199. DOI: https://doi.org/10.1016/j.ijhydene.2020.02.035. URL: https://www.sciencedirect.com/science/article/pii/S0360319920305176.

[2] Young-Woo You et al. “H2 PSA purifier for CO removal from hydrogen mixtures”. In: *International Journal of Hydrogen Energy* 37 (Dec. 2012), pp. 18175–18186. DOI: 10.1016/j.ijhydene.2012.09.044.

[3] Ayub Golmakani, Shohreh Fatemi, and Javad Tamnanloo. “Investigating PSA, VSA, and TSA methods in SMR Unit of Refineries for Hydrogen Production with Fuel Cell Specification”. In: *Separation and Purification Technology* 176 (Nov. 2016). DOI: 10.1016/j.seppur.2016.11.030.

[4] International Organization for Standardization. *ISO 14687:2019 - Hydrogen fuel quality – Product specification*. Accessed July 1, 2025. 2019. URL: https://www.iso.org/standard/69909.html (visited on 07/01/2025).

[5] Heleen Meuzelaar et al. “Trace level analysis of reactive ISO 14687 impurities in hydrogen fuel using laser-based spectroscopic detection methods”. In: *International Journal of Hydrogen Energy* 45.58 (2020), pp. 34024–34036. ISSN: 0360-3199. DOI: https://doi.org/10.1016/j.ijhydene.2020.09.046. URL: https://www.sciencedirect.com/science/article/pii/S0360319920334637.

[6] Zhemin Du et al. “A Review of Hydrogen Purification Technologies for Fuel Cell Vehicles”. In: *Catalysts* 11.3 (2021). ISSN: 2073-4344. DOI: 10.3390/catal11030393. URL: https://www.mdpi.com/2073-4344/11/3/393.

[7] Mauro Luberti and Hyungwoong Ahn. “Review of Polybed pressure swing adsorption for hydrogen purification”. In: *International Journal of Hydrogen Energy* 47.20 (2022), pp. 10911–10933. ISSN: 0360-3199. DOI: https://doi.org/10.1016/j.ijhydene.2022.01.147. URL: https://www.sciencedirect.com/science/article/pii/S0360319922002877.

[8] Saima Parkar et al. “Intensification of Temperature Swing Adsorption”. In: *Journal of Sustainable Materials Processing and Management* 2 (Apr. 2022). DOI: 10.30880/jsmpm.2022.02.01.009.

[9] Stuart Chalk and Leah McEwen. “The IUPAC Gold Book”. In: *Chemistry International* 39 (Jan. 2017). DOI: 10.1515/ci-2017-0307.

[10] Moslem Ahmadian, Hossein Derakhshankhah, and Mehdi Jaymand. “Recent advances in adsorption of environmental pollutants using metal–organic frameworks-based hydrogels”. In: *International Journal of Biological Macromolecules* 231 (2023), p. 123333. ISSN: 0141-8130. DOI: https://doi.org/10.1016/j.ijbiomac.2023.123333. URL: https://www.sciencedirect.com/science/article/pii/S0141813023002192.

[11] Xue-Feng Yan et al. “An adsorption isotherm model for adsorption performance of silver-loaded activated carbon”. In: *Thermal Science* 21 (Jan. 2017), pp. 48–48. DOI: 10.2298/TSCI151202048Y.

[12] Saeid Azizian, Setareh Eris, and Lee D. Wilson. “Re-evaluation of the century-old Langmuir isotherm for modeling adsorption phenomena in solution”. In: *Chemical Physics* 513 (2018), pp. 99–104. ISSN: 0301-0104. DOI: https://doi.org/10.1016/j.chemphys.2018.06.022. URL: https://www.sciencedirect.com/science/article/pii/S0301010418305317.

[13] Lingli Kong and Hertanto Adidharma. “A generalized van der Waals model for light gas adsorption prediction in IRMOFs”. In: *Phys. Chem. Chem. Phys.* 21 (17 2019), pp. 8906–8914. DOI: 10.1039/C9CP00285E. URL: http://dx.doi.org/10.1039/C9CP00285E.

[14] Abdelhamid Metrane et al. “Water Vapor Adsorption by Porous Materials: From Chemistry to Practical Applications”. In: *Journal of Chemical & Engineering Data* 67.7 (2022), pp. 1617–1653. DOI: 10.1021/acs.jced.2c00145. eprint: https://doi.org/10.1021/acs.jced.2c00145. URL: https://doi.org/10.1021/acs.jced.2c00145.

[15] Abdelhamid Metrane et al. “Water Vapor Adsorption by Porous Materials: From Chemistry to Practical Applications”. In: *Journal of Chemical & Engineering Data* 67.7 (2022), pp. 1617–1653. DOI: 10.1021/acs.jced.2c00145. eprint: https://doi.org/10.1021/acs.jced.2c00145. URL: https://doi.org/10.1021/acs.jced.2c00145.

[16] Stefan Wuttke. “Introduction to Reticular Chemistry. Metal–Organic Frameworks and Covalent Organic Frameworks Von Omar M. Yaghi, Markus J. Kalmutzki und Christian S. Diercks.” In: *Angewandte Chemie* 131 (June 2019). DOI: 10.1002/ange.201906230.

[17] Eng-Poh Ng and Svetlana Mintova. “Nanoporous materials with enhanced hydrophilicity and high water sorption capacity”. In: *Microporous and Mesoporous Materials* 114 (Sept. 2008), pp. 1–26. DOI: 10.1016/j.micromeso.2007.12.022.

[18] Elshaday Mulu, Milton M. M’Arimi, and Rose C. Ramkat. “A review of recent developments in application of low cost natural materials in purification and upgrade of biogas”. In: *Renewable and Sustainable Energy Reviews* 145 (2021), p. 111081. ISSN: 1364-0321. DOI: https://doi.org/10.1016/j.rser.2021.111081. URL: https://www.sciencedirect.com/science/article/pii/S1364032121003695.

[19] Petros Gkotsis et al. “Biogas upgrading technologies – Recent advances in membrane-based processes”. In: *International Journal of Hydrogen Energy* 48.10 (2023), pp. 3965–3993. ISSN: 0360-3199. DOI: https://doi.org/10.1016/j.ijhydene.2022.10.228. URL: https://www.sciencedirect.com/science/article/pii/S0360319922050418.

[20] Rosaria Augelletti, Maria Conti, and Maria Annesini. “Pressure swing adsorption for biogas upgrading. A new process configuration for the separation of biomethane and carbon dioxide”. In: *Journal of Cleaner Production* 140 (Oct. 2016). DOI: 10.1016/j.jclepro.2016.10.013.

[21] Marwan Kheimi and Sultan K. Salamah. “Simulation of temperature swing adsorption process to purify hydrogen for fuel cell uses by SAPO34 as adsorbent”. In: *Chemosphere* 338 (2023), p. 139454. ISSN: 0045-6535. DOI: https://doi.org/10.1016/j.chemosphere.2023.139454. URL: https://www.sciencedirect.com/science/article/pii/S0045653523017216.

[22] Lanlan Zhang et al. “A multi-node thermodynamic model on temperature-vacuum swing adsorption (TVSA) for carbon capture: Process design and performance analysis”. In: *Energy* 309 (2024), p. 133181. ISSN: 0360-5442. DOI: https://doi.org/10.1016/j.energy.2024.133181. URL: https://www.sciencedirect.com/science/article/pii/S0360544224029566.

[23] Peter Klobes, Klaus Meyer, and Ronald G. Munro. *Porosity and Specific Surface Area Measurements for Solid Materials*. NIST Special Publication 960–17. Accessed June 28, 2025. Gaithersburg, MD: National Institute of Standards and Technology, Aug. 2006. URL: https://tsapps.nist.gov/publication/get_pdf.cfm?pub_id=854263 (visited on 06/28/2025).

[24] Wei Liu et al. “Effect of Pore Size Distribution and Amination on Adsorption Capacities of Polymeric Adsorbents”. In: *Molecules* 26 (Aug. 2021), p. 5267. DOI: 10.3390/molecules26175267.

[25] Lumeng Liu et al. “Water adsorption on carbon - A review”. In: *Advances in Colloid and Interface Science* 250 (Nov. 2017). DOI: 10.1016/j.cis.2017.10.002.

[26] Toshihide Horikawa et al. “Scanning curves of water adsorption on graphitized thermal carbon black and ordered mesoporous carbon”. In: *Carbon* 95 (Aug. 2015), pp. 137–143. DOI: 10.1016/j.carbon.2015.08.034.

[27] Eng-Poh Ng and Svetlana Mintova. “Nanoporous materials with enhanced hydrophilicity and high water sorption capacity”. In: *Microporous and Mesoporous Materials* 114 (Sept. 2008), pp. 1–26. DOI: 10.1016/j.micromeso.2007.12.022.

[28] Y. Tashiro et al. “Assessment of adsorption-desorption characteristics of adsorbents for adsorptive desiccant cooling system”. In: *Journal of Materials Science* 39 (Feb. 2004), pp. 1315–1319. DOI: 10.1023/B:JMSC.0000013937.11959.6a.

[29] Józef Nastaj and Tomasz Aleksandrzak. “Adsorption Isotherms of Water, Propan-2-ol, and Methylbenzene Vapors on Grade 03 Silica Gel, Sorbonorit 4 Activated Carbon, and HiSiv 3000 Zeolite”. In: *Journal of Chemical & Engineering Data* 58.9 (2013), pp. 2629–2641. DOI: 10.1021/je400517c. eprint: https://doi.org/10.1021/je400517c. URL: https://doi.org/10.1021/je400517c.

[30] Eduardo Pérez-Botella, Susana Valencia, and Fernando Rey. “Zeolites in Adsorption Processes: State of the Art and Future Prospects”. In: *Chemical Reviews* 122.24 (2022). PMID: 36260918, pp. 17647–17695. DOI: 10.1021/acs.chemrev.2c00140. eprint: https://doi.org/10.1021/acs.chemrev.2c0014. URL: https://doi.org/10.1021/acs.chemrev.2c00140.

[31] Yu Wang. “Measurements and Modeling of Water Adsorption Isotherms of Zeolite Linde-Type A Crystals”. In: *Industrial & Engineering Chemistry Research* 59.17 (2020), pp. 8304–8314. DOI: 10.1021/acs.iecr.9b06891. eprint: https://doi.org/10.1021/acs.iecr.9b06891. URL: https://doi.org/10.1021/acs.iecr.9b06891.

[32] Guang-Ping Hao et al. “Unusual ultra-hydrophilic, porous carbon cuboids for atmospheric-water capture”. In: *Angewandte Chemie International Edition* 54 (2015). DOI: 10.1002/anie.201409439.

[33] D. Olson, W. Haag, and William Borghard. “Use of water as a probe of zeolitic properties: Interaction of water with HZSM-5”. In: *Microporous and Mesoporous Materials - MICROPOROUS MESOPOROUS MAT* 35 (Apr. 2000), pp. 435–446. DOI: 10.1016/S1387-1811(99)00240-1.

[34] P.A.S. Moura et al. “Water adsorption and hydrothermal stability of CHA zeolites with different Si/Al ratios and compensating cations”. In: *Catalysis Today* 390-391 (2022). CIS-2021 Young Researchers, pp. 99–108. ISSN: 0920-5861. DOI: https://doi.org/10.1016/j.cattod.2021.11.042. URL: https://www.sciencedirect.com/science/article/pii/S0920586121005290.

[35] Abdelhamid Metrane et al. “Water Vapor Adsorption by Porous Materials: From Chemistry to Practical Applications”. In: *Journal of Chemical & Engineering Data* 67 (June 2022). DOI: 10.1021/acs.jced.2c00145.

[36] Jérôme Canivet et al. “Water adsorption in MOFs: Fundamentals and applications”. In: *Chemical Society reviews* 43 (May 2014). DOI: 10.1039/c4cs00078a.

[37] Rahul Banerjee et al. “Pore Surface Engineering in Porous, Chemically Stable Covalent Organic Frameworks for Water Adsorption”. In: *J. Mater. Chem. A* 3 (Nov. 2015). DOI: 10.1039/C5TA07998E.

[38] Suvendu Karak et al. “Constructing Ultraporous Covalent Organic Frameworks in Seconds via an Organic Terracotta Process”. In: *Journal of the American Chemical Society* 139 (Jan. 2017). DOI: 10.1021/jacs.6b08815.

[39] Qi Chen et al. “Mesoporous Conjugated Polycarbazole with High Porosity via Structure Tuning”. In: *Macromolecules* 47 (Sept. 2014), pp. 5926–5931. DOI: 10.1021/ma501330v.

[40] M. Rozwadowski et al. “Mechanism of Adsorption of Water, Benzene, and Nitrogen on Al-MCM-41 and Effect of Coking on the Adsorption”. In: *Langmuir* 17.7 (2001), pp. 2112–2119. DOI: 10.1021/la0006723. eprint: https://doi.org/10.1021/la0006723. URL: https://doi.org/10.1021/la0006723.

[41] Lingxin Chen et al. “Molecular imprinting: Perspectives and applications”. In: *Chemical Society Reviews* 2016 (Mar. 2016), pp. 2137–2211. DOI: 10.1039/C6CS00061D.

[42] Abdelhamid Metrane et al. “Water Vapor Adsorption by Porous Materials: From Chemistry to Practical Applications”. In: *Journal of Chemical & Engineering Data* 67.7 (2022), pp. 1617–1653. DOI: 10.1021/acs.jced.2c00145. URL: https://doi.org/10.1021/acs.jced.2c00145.

[43] K. Sing F. Rouquerol J. Rouquerol. *Adsorption by Powders and Porous Solids*. Acedemic Press, 1998.

[44] Darren Broom. “Characterizing adsorbents for gas separations”. In: *Chemical Engineering Progress* 114 (Mar. 2018), pp. 30–37.

[45] J.F. Nastaj, B. Ambrożek, and J. Rudnicka. “Simulation studies of a vacuum and temperature swing adsorption process for the removal of VOC from waste air streams”. In: *International Communications in Heat and Mass Transfer* 33.1 (2006), pp. 80–86. ISSN: 0735-1933. DOI: https://doi.org/10.1016/j.icheatmasstransfer.2005.08.005. URL: https://www.sciencedirect.com/science/article/pii/S073519330500148X.

[46] So-mang Kim and Grégoire Léonard. “Process modelling of Direct Air Capture (DAC) of CO2 using solid amine sorbents”. In: *32nd European Symposium on Computer Aided Process Engineering*. Ed. by Ludovic Montastruc and Stephane Negny. Vol. 51. Computer Aided Chemical Engineering. Elsevier, 2022, pp. 265–270. DOI: https://doi.org/10.1016/B978-0-323-95879-0.50045-X. URL: https://www.sciencedirect.com/science/article/pii/B978032395879050045X.

[47] Jan F. Wiegner et al. “Optimal Design and Operation of Solid Sorbent Direct Air Capture Processes at Varying Ambient Conditions”. In: *Industrial & Engineering Chemistry Research* 61.34 (2022), pp. 12649–12667. DOI: 10.1021/acs.iecr.2c00681. URL: https://doi.org/10.1021/acs.iecr.2c00681.

[48] Shing Bo Peh, Shamsuzzaman Farooq, and Dan Zhao. “Techno-economic analysis of MOF-based adsorption cycles for postcombustion CO2 capture from wet flue gas”. In: *Chemical Engineering Science* 268 (2023), p. 118390. ISSN: 0009-2509. DOI: https://doi.org/10.1016/j.ces.2022.118390. URL: https://www.sciencedirect.com/science/article/pii/S0009250922009757.

[49] Francesco Sabatino et al. “Evaluation of a Direct Air Capture Process Combining Wet Scrubbing and Bipolar Membrane Electrodialysis”. In: *Industrial & Engineering Chemistry Research* 59.15 (2020), pp. 7007–7020. DOI: 10.1021/acs.iecr.9b05641. URL: https://doi.org/10.1021/acs.iecr.9b05641.

[50] Anshuman Sinha et al. “Systems Design and Economic Analysis of Direct Air Capture of CO2 through Temperature Vacuum Swing Adsorption using MIL-101(Cr)-PEI-800 and mmen-Mg2(dobpdc) MOF Adsorbents”. In: *Industrial and Engineering Chemistry Research* 56 (Dec. 2016). DOI: 10.1021/acs.iecr.6b03887.

[51] Fidal Bashir et al. “Performance and Cost Analysis of Pressure Swing Adsorption for Recovery of H2, CO, and CO2 from Steelworks Off-Gases”. In: *Energies* 18 (May 2025), p. 2440. DOI: 10.3390/en18102440.

[52] David Danaci, Paul Webley, and Camille Petit. “Guidelines for Techno-Economic Analysis of Adsorption Processes”. In: *Frontiers in Chemical Engineering* 2 (Jan. 2021), p. 602430. DOI: 10.3389/fceng.2020.602430.

[53] Jiaji Su et al. “A statistical approach to estimating adsorption-isotherm parameters in gradient-elution preparative liquid chromatography”. In: *The Annals of Applied Statistics* 17.4 (2023), pp. 3476–3499. DOI: 10.1214/23-AOAS1772. URL: https://doi.org/10.1214/23-AOAS1772.

[54] Bahare Abdoos, Almerinda Di Benedetto, and Danilo Russo. “Integrated design, scale-up, and surrogate-based optimization of PSA systems for hydrogen purification from ammonia decomposition”. In: *Chemical Engineering Journal* 526 (2025), p. 170994. ISSN: 1385-8947. DOI: https://doi.org/10.1016/j.cej.2025.170994. URL: https://www.sciencedirect.com/science/article/pii/S1385894725118408.

[55] Zeinab Jabbari, Vinny Cris M, and A. M. “Simulation of multi-step pressure swing adsorption process for production of pure hydrogen with high recovery”. In: *Chemical Engineering Journal* (2011).

[56] A. Henrotin et al. “Modelling and optimization of vacuum pressure swing adsorption CO2 capture pilot using MIL-160(Al)”. In: *Chemical Engineering Research and Design* 226 (2026), pp. 14–30. ISSN: 0263-8762. DOI: https://doi.org/10.1016/j.cherd.2025.12.030. URL: https://www.sciencedirect.com/science/article/pii/S0263876225006896.

[57] Harish Khajuria. “Model-based Design, Operation and Control of Pressure Swing Adsorption Systems”. PhD thesis. Imperial College London, 2011.

[58] Aspen. *Introduction to Aspen Adsorption*. AspenTech, 2008.

[59] ASPEN TECH. *Title of the Webpage*. 2026. URL: https://www.aspentech.com/en/products/engineering/aspen-adsorption-and-aspen-chromatography (visited on 08/31/2026).

[60] National Renewable Energy Laboratory. *Measurement of Hydrogen Production Rate Based on Dew Point Temperatures*. Independent Review Report NREL/MP-150-42237. Golden, Colorado, USA: National Renewable Energy Laboratory, Nov. 2007.

[61] Kevin R. Wood, Y. A. Liu, and Yueying Yu. *Design, Simulation, and Optimization of Adsorptive and Chromatographic Separations: A Hands-On Approach*. 1st ed. Weinheim, Germany: Wiley-VCH Verlag GmbH & Co. KGaA, 2018.

[62] Zubair Riaz. "Modelling of Gas Separations Using Aspen Adsorption Software". Master's Thesis. Lappeenranta–Lahti University of Technology, 2021.

[63] Aspen Technology, Inc. *Aspen Adsorption Help*. Version 12. Software documentation. Aspen Technology, Inc. Bedford, Massachusetts, USA, 2019.

[64] Haripriya Naidu and Alexander P. Mathews. "Linear driving force analysis of adsorption dynamics in stratified fixed-bed adsorbers". In: *Separation and Purification Technology* 257 (2021), p. 117955. ISSN: 1383-5866. DOI: https://doi.org/10.1016/j.seppur.2020.117955. URL: https://www.sciencedirect.com/science/article/pii/S138358662032428X.

[65] Andreas Gorbach, M. Stegmaier, and Gerhart Eigenberger. "Measurement and Modeling of Water Vapor Adsorption on Zeolite 4A—Equilibria and Kinetics". In: *Adsorption* 10 (Jan. 2004), pp. 29–46. DOI: 10.1023/B:ADSO.0000024033.60103.ff.

[66] Yu Wang. "Measurements and Modeling of Water Adsorption Isotherms of Zeolite Linde-Type A Crystals". In: *Industrial Engineering Chemistry Research* 59.17 (Apr. 2020), pp. 8304–8314.

[67] Kevin Loughlin. "Water isotherm models for 4A (NaA) zeolite". In: *Adsorption* 15 (Aug. 2009), pp. 337–353. DOI: 10.1007/s10450-009-9189-2.

[68] Almas Mardanov. "Modelling and Sizing of Post-Processing Equipment for Wet Hydrogen from Alkaline Electrolysis". Faculty of Mechanical, Maritime and Materials Engineering. Graduation Project. Delft, The Netherlands: Delft University of Technology, 2023.

[69] Elliot Scuiller et al. "New Approach for Measuring the Specific Heat Capacity of Reactive Adsorbents Using Calorimetry". In: *Journal of Chemical Engineering Data* 68.8 (July 2023), pp. 1865–1871.

[70] N. Wakao, S. Kaguei, and T. Funazkri. "Effect of fluid dispersion coefficients on particle-to-fluid heat transfer coefficients in packed beds: Correlation of nusselt numbers". In: *Chemical Engineering Science* 34.3 (1979), pp. 325–336. ISSN: 0009-2509. DOI: https://doi.org/10.1016/0009-2509(79)85064-2. URL: https://www.sciencedirect.com/science/article/pii/0009250979850642.

[71] M. J. Assael et al. "Correlation of the Thermal Conductivity of Normal and Parahydrogen from the Triple Point to 1000 K and up to 100 MPa". In: *Journal of Physical and Chemical Reference Data* 40.3 (2011), p. 033101. DOI: 10.1063/1.3606499.

[72] Simscale. *Title of the Webpage*. 2026. URL: https://www.simscale.com/docs/simwiki/numerics-background/what-is-nusselt-number/ (visited on 08/31/2026).

[73] Dassault Systems. *Welcome to the SOLIDWORKS Web Help*. 2026. URL: https://help.solidworks.com/2021/english/SolidWorks/cworks/c_Convection.htm#jmd1450460168782 (visited on 08/31/2026).

[74] The Engineering ToolBox. *Stainless Steel: Specific Heat and Thermal Conductivities versus Temperatures*. https://www.engineeringtoolbox.com/stainless-steel-specific-heat-thermal-conductivity-vs-temperature-d_2225.html. Accessed: 2 August 2026. 2023.

[75] Warren L. McCabe, Julian C. Smith, and Peter Harriott. *Unit Operations of Chemical Engineering*. 5th ed. New York: McGraw-Hill, 1993. ISBN: 0-07-044844-2.

[76] P.B. Tamarona, T.J.H. Vlugt, and M. Ramdin. "OpenPyTEA: An open-source python toolkit for techno-economic assessment of chemical process plants and energy systems with economic sensitivity and uncertainty evaluation". In: *SoftwareX* 35 (2026), p. 102816. ISSN: 2352-7110. DOI: https://doi.org/10.1016/j.softx.2026.102816. URL: https://www.sciencedirect.com/science/article/pii/S2352711026003080.

[77] National Institute of Standards and Technology. *Hydrogen*. NIST Chemistry WebBook, NIST Standard Reference Database Number 69. CAS Registry Number 1333-74-0; accessed 2 August 2026. 2025. DOI: 10.18434/T4D303. URL: https://webbook.nist.gov/cgi/cbook.cgi?ID=C1333740&Mask=187&Units=SI.